Cape Peninsula
University of Technology

ESTIMATION OF THE DIRECTION OF ARRIVAL OF SIGNALS FROM NANO-SATELLITES USING ANTENNA INTERFEROMETRY

by

FENNI MAGANO TWEETHENI SHIDHIKA

Thesis submitted in fulfilment of the requirements for the degree

Master of Technology: ELECTRICAL ENGINEERING

in the Faculty of Engineering

at the Cape Peninsula University of Technology

Supervisor: Dr. K. Govender
Co-supervisor: Prof. P. J. Cilliers

Bellville

November 2014

CPUT copyright information

The thesis may not be published either in part (in scholarly, scientific or technical journals), or as a whole (as a monograph), unless permission has been obtained from the University.

DECLARATION

I, Fenni Magano Tweetheni Shidhika, declare that the content of this thesis represents my own unaided work, and that the thesis has not previously been submitted for academic examination towards any qualification. Furthermore, it represents my own opinions and not necessarily those of the Cape Peninsula University of Technology.

Signed **Date**

ABSTRACT

The thesis reports on the evaluation and comparison of various signal processing algorithms for estimating the direction of arrival (DOA) of a high frequency (HF) beacon signal from a CubeSat in Low Earth Orbit (LEO). The DOA of the HF beacon signal is expressed in terms of the two angles, azimuth (α) and elevation (ε). The azimuth and elevation angles of the received HF signal are calculated from the phase differences between signals observed at three elements of an L-shaped crossed-loop antenna array. The algorithms which were evaluated are the Zero Crossing (ZC), Cross Correlation (CC), Fast Fourier Transform (FFT) and Cross Power Spectral Density (CPSD) algorithms. A theoretical analysis was done to demonstrate that the phase differences at the radio frequency (RF) of the beacon are propagated to the baseband signals. The algorithms were thus tested using simulated baseband signals as would be derived from the RF signals intercepted by the three elements of an L-shaped crossed-loop antenna array. Gaussian noise with a given signal-to-noise ratio (SNR) was added to the simulated baseband signals. The algorithms were implemented in MATLAB. The criteria for the selection of the best algorithm were accuracy and speed. The standard deviation (SD) of the azimuth and elevation errors was used to measure the performance accuracy of each algorithm, while the computational time for a given number of samples and runs was used to express the speed of each algorithm.

First the ZC, CC, FFT and CPSD algorithms were evaluated for various SNR values, and compared with respect to SD of the azimuth and elevation errors. The analysis of the simulations demonstrate that the FFT and CPSD algorithms outperform the ZC and CC algorithms by estimating the DOA with a small SD of errors even at the low SNR of 0 dB, where the noise amplitude is the same as the signal amplitude. The ZC algorithm estimates the DOA with a large SD of error at low SNR due to multiple ZC points occurring during the same cycle. The ZC algorithm breaks down when the SNR decreases below 35 dB. The accuracy of the ZC algorithm depends on the method by which the ZC points are detected. The CC algorithm breaks down when the SNR decreases below 10 dB. The CPSD and FFT algorithms break down when the SNR decreases below – 20 dB. However, at a high SNR of 40 dB and above, all the algorithms estimate the DOA with a SD of error smaller than 1˚ for the azimuth and elevation. Next, the ZC, CC, FFT and CPSD algorithms were compared with respect to computation time. The FFT was found to be the fastest algorithm. Although the CPSD and the FFT algorithms reach the same accuracy in the estimation of the DOA, the FFT was selected as the optimum algorithm due to its better computation time. Recommendations are made regarding the implementation of the proposed algorithms for real signals from the HF direction finding (DF) array. At the time of submission of this thesis, such signals were not yet available.

ACKNOWLEDGEMENTS

I wish to thank:

- The Almighty God, for giving me strength and courage through his grace, to complete my thesis.
- My two supervisors, Prof. Pierre Cilliers and Dr. Kessie Govender, for their excellent guidance, support and encouragement. I was greatly motivated and inspired by their knowledge and expertise. This thesis would not have been possible without their input. It was not easy, but with their constant support and help, I manage to complete my thesis.
- The French South African Institute of Technology (F'SATI) for the scholarship.
- SANSA: Space Science Directorate, for providing accommodation, while I was based at SANSA Space Science in Hermanus, and for allowing me to use their facilities for my project.
- My family for the moral support and encouragement during my studies.
- Electdom Matandirotya and David Perez for all their assistance and ideas.
- Jeanne Cilliers for proofreading my thesis.
- All my classmates for academic support, guidance and encouragement.
- My friends for moral support and motivation.

The financial assistance of the National Research Foundation towards this research is acknowledged. Opinions expressed in this thesis and the conclusions arrived at, are those of the author, and are not necessarily to be attributed to the National Research Foundation.

DEDICATION

I dedicate this thesis to my parents (Aron Shidhika and Johanna Shidhika) as a token of gratitude for their continuous support, love, encouragement and patience. Dad and Mom, thank you for inspiring the importance of hard work and higher education, and allowing me to go this far with my studies.

I further dedicate this thesis to my siblings (late Jesaya Nanzimbogo, Alisa Kakwambi, Alisa Shidhika, Erastus Shidhika, Lucky Shidhika, Tangi Martin Nanzimbogo and Rosemary Hapulile) - you all contributed to this work. May you also be motivated, encouraged and inspired to reach your dreams. Ultimately, I dedicate this work to the Almighty God.

RESEARCH OUTPUTS

1. Shidhika F.M.T, Govender K, Cilliers P.J, A high frequency direction of arrival interferometer for the ZACUBE-1 mission, Abstract presented at CPUT Postgraduate Conference 2013, Bellville, South Africa, 5 November 2013.

2. Cilliers P.J, Opperman B.D.L, Van Zyl R.R, Visser D.F, Shidhika F, Agaba D, Inggs M, HF Beacon on South African CubeSat for characterization of SuperDARN radar antennas and interferometers, Poster presented at SCAR Open Science Conference 2014, Auckland, New Zealand, 25-28 August 2014

3. P.J. Cilliers, F. Shidhika, S. Cupido, K. Govender, R.R. Van Zyl, HF DF Array and DOA estimation algorithms for the ZACUBE-1 HF Beacon, Abstract presented at the 2nd International African CubeSat Workshop 2014, CPUT, Bellville, 4 November 2014

4. Shidhika F.M.T, Govender K, Cilliers P.J, A comparison of various signal processing algorithms for estimating direction of arrival (DOA) for the high frequency (HF) radio beacon signal operating at 14.099 MHz on a CubeSat, to be submitted to the International Journal of Satellite Communications and Networking

TABLE OF CONTENTS

LIST OF FIGURES

LIST OF TABLES

GLOSSARY

Terms/Acronyms/Abbreviations/Symbols

AOA	Angle of Arrival
CC	Cross Correlation
CPSD	Cross Power Spectral Density
CPSP	Cross Power-Spectrum Phase
CPUT	Cape Peninsula University of Technology
CubeSat	Cube Satellite
DF	Direction Finding or Direction Finder
DOA	Direction of Arrival
DST	Department of Science and Technology
ESPRIT	Estimation of Signal Parameters via Rotational Invariance Techniques
EUV	Extreme Ultra-violet
EVD	Eigenvalue Decomposition
FFT	Fast Fourier Transform
F'SATI	French South African Institute of Technology
GCC	Generalised Cross Correlation
HF	High Frequency (3 – 30 MHz)
IF	Intermediate Frequency
IRI	International Reference Ionosphere
LEO	Low Earth Orbit
LNA	Low Noise Amplifier
LMS	Least Mean Square
LO	Local Oscillator
LUF	Lowest Usable Frequency
MHz	Megahertz
MUSIC	Multiple Signal Classification
n.d.	No date of publication

NRF	National Research Foundation
PDF	Probability Distribution Function
RF	Radio Frequency
RMSE	Root Mean Square Error
RX	Receiver
SANAE	South African National Antarctic Expedition
SANSA	South African National Space Agency
SD	Standard Deviation
SNR	Signal-to-noise ratio
SUN	Stellenbosch University
SuperDARN	Super Dual Auroral Radar Network
TDOA	Time Difference of Arrival
TOA	Time of Arrival
TX	Transmitter
TTFD	Twin Terminated Folded Dipole
TshepisoSAT	Tshepiso Satellite also known as ZACUBE-1
UCA	Uniform Circular Array
ZC	Zero Crossing

CHAPTER ONE: INTRODUCTION

1.1 Introduction

The aim of the thesis is to select the optimum algorithm for the determination of the direction of arrival (DOA) of signals from a high frequency (HF) beacon transmitter onboard the ZACUBE-1 nano-satellite, also known as TshepisoSAT. The selection of the optimum algorithm was based on two figures of merit, namely accuracy and speed, using simulated baseband signals

ZACUBE-1 (TshepisoSAT) is a space weather CubeSat mission developed by students at Cape Peninsula University of Technology (CPUT), incorporating the French South African Institute of Technology (F'SATI), the South African National Space Agency (SANSA) and Stellenbosch University (SUN), with funding from the South African Department of Science and Technology (DST) and National Research Foundation (NRF). The CubeSat was launched on the 21 November 2013 by a Russian Dnepr launch vehicle at a nominal height of 600 km and at an inclination angle of 98˚ (Van Zyl *et al*., 2013:52). The main payload on the CubeSat is a HF beacon transmitter operating at 14.099 MHz. The mission has the following objectives:

- To study ionospheric propagation of HF (3 – 30 MHz) radio waves.
- To use the HF beacon signal to calibrate the interferometer of the Super Dual Auroral Radar Network (SuperDARN) at the SANAE (South Africa National Antarctica Expedition) base in Antarctica (2.84˚W, 71.67˚S) (Van Zyl *et al*., 2013:52).

The HF signal is transmitted by means of a 10 m long wire antenna. The CubeSat has to spin at a given rate of 2˚ per second, for the wire antenna to remain straight while being deployed (Van Zyl *et al*., 2013:52). Figure 1-1 shows ZACUBE-1 (TshepisoSAT) with the mechanism that was designed and implemented to deploy the antenna.

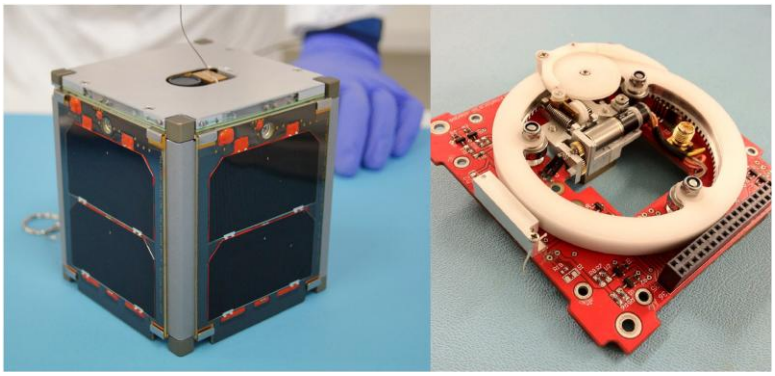

Figure 1-1: The 1.2 kg ZACUBE-1 (TshepisoSAT) measuring 10 cm x 10 cm x 10 cm, with the visible section of the 10 m wire antenna for the HF beacon (left) and the deployment mechanism for the antenna (right) (From Van Zyl *et al*., 2013:53)

1.2 Background to the ZACUBE-1 (TshepisoSAT) mission

In 2007, a space industry capacity survey was conducted by the DST. The results revealed that South Africa has a space heritage dating back to the 1950s. In addition, the study revealed that paucity in the space industry was mainly due to a shortage of engineers and professionals. DST concluded that South Africa's space heritage and skills would become invisible if not exploited within the next 5 to 10 years.[1]

Thus DST and NRF determined to implement a massive human capital development drive to develop specialists in this field. CPUT in conjunction with F'SATI introduced a Master's degree in Satellite Systems Engineering, which is funded by DST and NRF.

F'SATI uses CubeSats as an educational tool to provide students with hands-on experience in space technology. Over time it has developed into a standard that facilitates inexpensive space missions and is useful for technology demonstrations. The standard dimensions are 10 cm x 10 cm x 10 cm, with a mass of not more than 1.33 kg (Woeller *et al*., 2011).

With the inauguration of the Satellite Systems Engineering Programme at F'SATI, the 3U CubeSat mission (ZACUBE-2) was defined as a long-term project with a prototype planned for October 2011. However, an opportunity was recognised whereby a simple, small low-cost space weather mission could be developed and launched within the same timeline as the 3U CubeSat prototype. This whole concept would give students hands-on experience in a complete mission, from concept to launch and operations. This mission was named as ZACUBE-1 and is now known as TshepisoSAT.[2] The main payload on board the CubeSat was proposed by the Space Science Directorate of SANSA.

The Space Science Directorate of SANSA operates the South African Super Dual Auroral Radar Network (SuperDARN) at the South African National Antarctic Expedition (SANAE) base in Antarctica. The radar comprises a 16-element Twin Terminated Folded Dipole (TTFD) antenna array (main array) and a secondary four-element array 100 m north of the main array (Greenwald *et al*., 1995:761). This set of antennas is one of the stations of the SuperDARN. The objective of the SuperDARN is to transmit HF signals into the ionosphere, and to capture the reflected signals. The data captured by the radar is used to analyse the dynamic and spatial behaviour of ionospheric density and to predict the HF radio propagation conditions (Visser, 2009:13).

[1] www.cput.ac.za/blog/fsati/cubesat

[2] http://active.cput.ac.za/fsati

SuperDARN is an international network of 33 radar networks which monitors the ionospheric electron density in the northern and southern polar regions. The SuperDARN radars operate in the frequency range 8 – 20 MHz (Agaba, 2012:5). The placement of an HF beacon transmitter on a CubeSat was proposed after several unsuccessful attempts to calibrate the interferometer of the SuperDARN antenna array at the SANAE base. Previous attempts included the transmission of HF signals via a helicopter. The latter experiment failed due to the intermittent nature of transmission and due to errors in logging the position of the helicopter at the time of transmission (Cilliers *et al*., 2013:1290). Figure 1-2 shows the main antenna array of the current SuperDARN at SANAE.

Figure 1-2: The 16-element Twin Terminated Folded Dipole (TTFD) antenna array of the SuperDARN radar in Antarctica (Adapted from Cilliers *et al*., 2013:1290)

1.3 Background to the research problem

The HF beacon signal that is transmitted from the CubeSat will be received by the ground stations at SANSA Space Science in Hermanus (19.24°E, 34.42°S), at SANAE in Antarctica (2.84˚W, 71.67˚S) and at any other receiver tuned to the beacon frequency.[3] The purpose of these ground stations is to measure the incoming azimuth and elevation angles of a 14.099 MHz beacon signal transmitted from the CubeSat, using the phase difference between the signals received at the different elements of the interferometer arrays. The measured data will be used to contribute to the knowledge of the Earth's ionosphere and assist scientists in modeling the ionosphere. Scientists use ionospheric models to determine the ionospheric electron density (Visser, 2009:13). Ionospheric models are crucial in gaining an understanding of space weather and its impact on communication technologies.

There are currently two interferometer antenna arrays for receiving the HF beacon signal namely, the South African SuperDARN at SANAE with a 16-element Twin Terminated

[3] http://www.sansa.org.za/spacescience/resource-centre/news/529-understanding-space-plasma

Folded Dipole antenna array, plus a four-element array of the same design, and a seven-element HF DF interferometer array in Hermanus, South Africa, of which the first three elements were being constructed at the time of submission of this thesis (see Figure 1-4).

F'SATI, in collaboration with SANSA Space Science, designed the HF DF interferometer array. The purpose of this array is the estimation of the DOA of a 14.099 MHz signal transmitted from the CubeSat in Low Earth Orbit (LEO). The HF DF interferometer will comprise seven elements, each made of two orthogonal crossed loop dipole antennas. The seven elements are arranged in an L-shape with one leg of the L approximately east-west and the other approximately north-south with a 90° angle between the two legs. The measurements of the phase difference of the trans-ionospheric HF signals received at the crossed loop antennas will be used to determine the DOA. The DOA is expressed in terms of two angles, the azimuth (α) and elevation (ε). Figure 1-3 shows the proposed layout for the HF DF interferometer array at SANSA Space Science in Hermanus.

The spacing between the elements was designed such, that the distance between the reference antenna and the first two orthogonal crossed loop dipole antennas is less than a wavelength of the HF beacon signal. The distance between the reference antenna and the second two orthogonal crossed loop antennas is slightly more than a half a wavelength. The distance between the reference and the third two orthogonal crossed loop antennas is more than the distance between the reference and the second two orthogonal antennas. The calculation of the optimum spacing between the elements is beyond the scope of the thesis; however, the layout of the receiver array and the values provided in Figure 1-3 were suggested by other group members. The other group members were also responsible for the design and installation of the HF DF interferometer array.

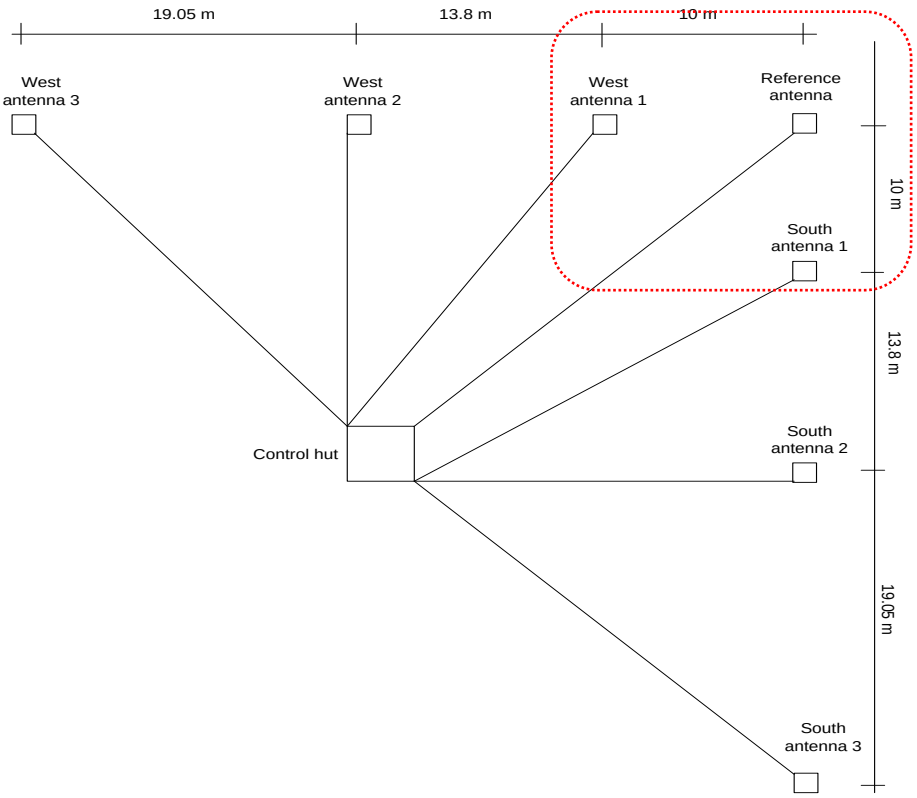

Figure 1-3: The orientation and spacing of the seven elements of the HF DF interferometer array designed for estimating the DOA of the HF beacon signal from the ZACUBE-1 satellite. Only the three antennas surrounded by the dotted lines have been implemented so far. The algorithms described in this thesis are based on simulations of the signals received at the Reference antenna, West antenna 1 (W1) and South antenna 1 (S1)

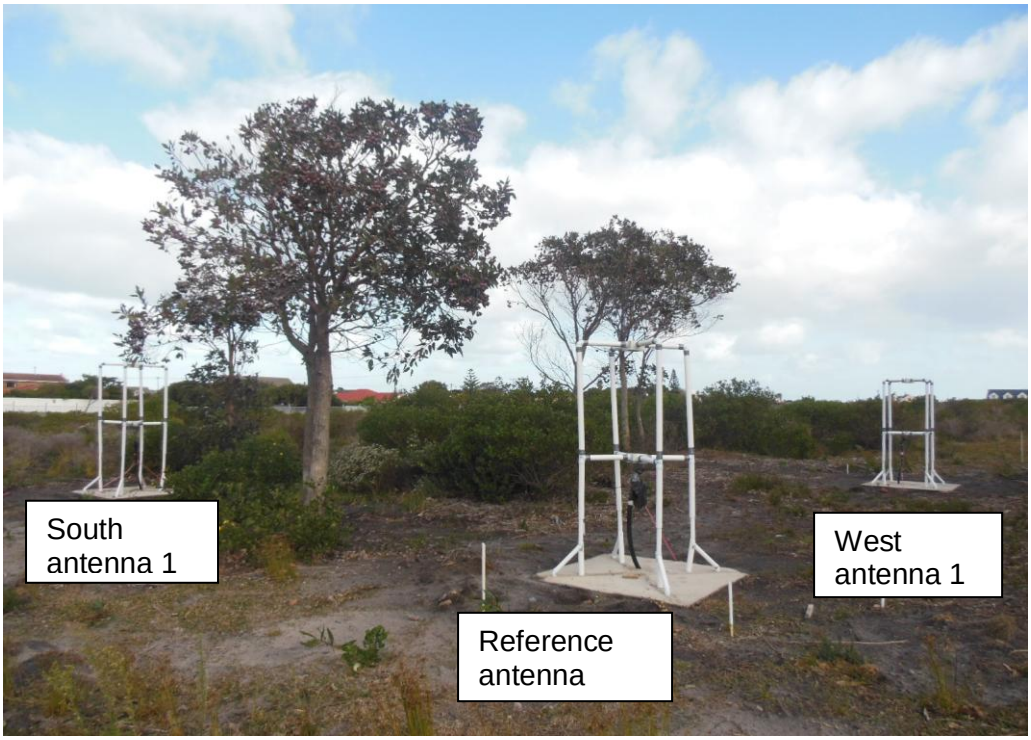

Figure 1-4: The first three elements (circled with a dotted red line in Figure 1-3) of the HF DF array at SANSA Space Science in Hermanus

The HF DF interferometer at SANSA Space Science will be used to make an independent measurement of the satellite's position during overpass and to develop the algorithms. A similar antenna array will be constructed at SANAE as an independent tool to calibrate the beam pattern of the SuperDARN in Antarctica in future.

The HF DF array was designed as a project for a group. The hardware component, developed by group members at F'SATI, captures the RF signal and converts it to baseband. The software component stores and analyses the sampled baseband signals from the HF receiving system. The stored data contains the time and location of reception of the signal from ZACUBE-1 (TshepisoSAT). Additionally, the software has to extract the stored raw data to provide an estimate DOA of the 14.099 MHz beacon signal. The author's contribution was to research the appropriate signal processing algorithm for the DF processor. The objective was to evaluate and compare the performance of algorithms that estimate the DOA from the phase differences by means of simulations. The criteria for the selection of the optimum algorithm were accuracy and speed. Figure 1-5 depicts the block diagram of the whole project.

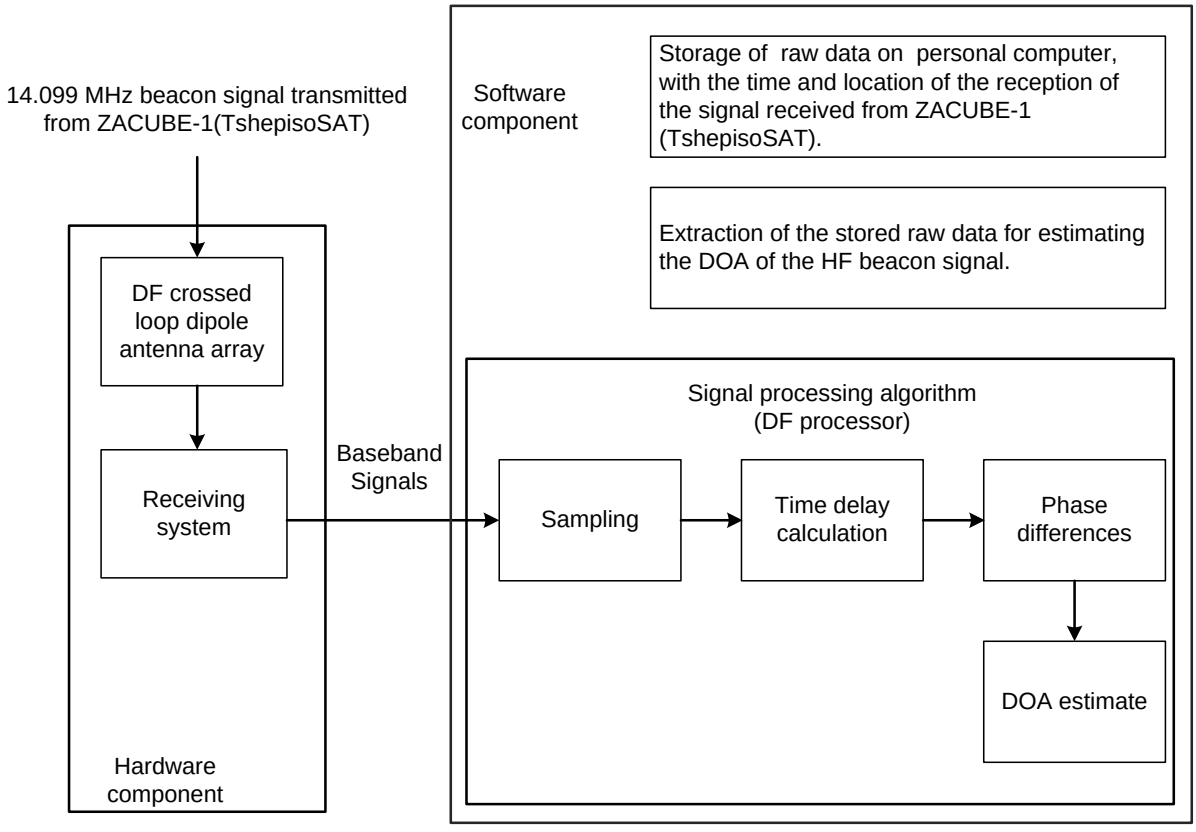

Figure 1-5: The HF DF ground station. The signals from the receiver are baseband signals that have to be sampled and processed. The signal processing algorithms process the simulated baseband signals to estimate the DOA from the time delays and phase differences

1.3.1 DF system overview

Direction finding (DF) refers to systems that determine the DOA of the incoming radio frequency (RF) signal (Herndon, 1991:1). The main purpose of DF systems is to measure the DOA of the incoming signal relative to a known reference which can be geographic north, magnetic north or grid north. DF systems receive radio waves from a source that is assumed to be very far; it processes the received signals and locates the direction of the incoming signal (Gething, 1991:7).

Figure 1-6 depicts the major components of DF systems which include:

- **A DF antenna array** with directional property, which is responsible for receiving electromagnetic energy and translating the energy into an electrical signal that contains the DOA information (Tsai, 2008:4). The antenna array has a directional property due to the phase delay between the signals received by the elements of the array.
- **A receiving system**, which comprises one receiver channel per antenna that is responsible for measuring the response of the antenna array. The receiving system plays a major role in down-converting the signal to intermediate frequency (IF) or baseband (Herndon, 1991:1).
- **A DF processor**, which further processes the signal received to obtain the DOA information (Silva *et al*., 2011).
- **An Output device** is responsible for displaying the DOA information and preparing the transmission of the DOA information to the recipients of the DF data (Herndon, 1991:1).

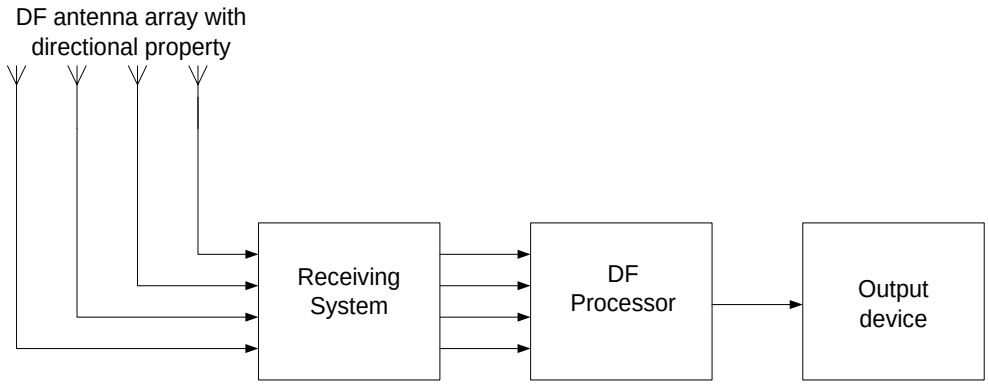

Figure 1-6: Block diagram of the general DF system (Adapted from Papandreou, 1997)

There are several factors that should be taken into consideration when designing a DF system. The selection of the array geometry and antennas, the structure of the receiver, and

the signal processing algorithm for DOA estimates appear to be the main factors. This thesis is primarily concerned with the selection of the signal processing algorithm.

However, the antenna array is considered to be the crucial element that affects the accuracy of the performance of the DF system, therefore the design of the antenna array has to be critically reviewed. The geometry of the array influences aspects of the DF system, such as resolution, sensitivity due to systematic errors and the processing algorithm that estimates the DOA (Abdullah, 2006:2). Yet, in most cases the antennas in the array are assumed to be identical, for purposes of simplifying the practical installation of the array and the analysis of the data.

DF systems are categorised. In some systems, only the horizontal angle known as azimuth angle (α) can be determined. Azimuth angle is measured clockwise from the y-axis. However, some systems can determined both the horizontal and vertical angle known as the elevation angle (ε), measured from the z-axis. The z-axis is in the direction of zenith, while the y-axis is the reference direction for the azimuth measurement, as illustrated in Figure 1-7. This is referred to as a radial coordinate system (Herndon, 1991:9). In a radial coordinate system, the azimuth and elevation angles represent the complete measurement of the DOA of the incoming signal (Gething, 1991:1). For this thesis both azimuth and elevation angles are resolved, to locate the source where the signal is being transmitted from. The optimal DF should work over a wide angular range, with azimuth angle up to 360˚ and elevation angle up to 90˚.

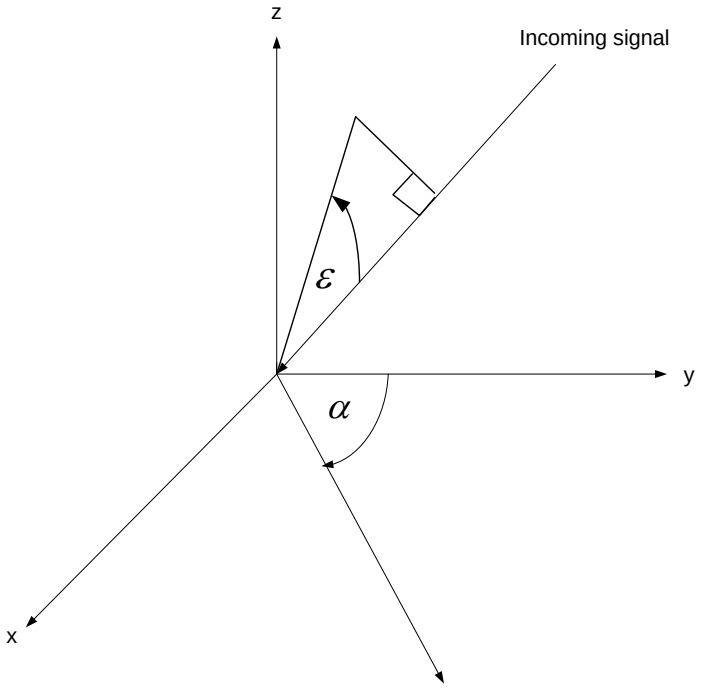

Figure 1-7: The radial coordinate system of a DF that resolves both the azimuth and elevation angles characterising the DOA

1.3.2 Phase comparison or interferometer methods

The phase comparison of the interferometer DF system is considered one of the important techniques for determining the DOA, when great accuracy is important (Jianhua *et al*., 2000). The interferometer uses time delay to estimate the phase difference between signals received at the antenna elements. These phase differences are then translated into DOA information (Paulose *et al*., 2013:935).

At least two antennas are required for the interferometer technique and the antennas need to be spaced at less than a half a wavelength to resolve the DOA without ambiguity. Furthermore, the detection of the azimuth and elevation is done through various algorithms that use the measured phase differences as inputs. However, the easiest case of detecting the elevation is to analyse an incoming signal received on the array from an azimuthal direction along the line between the antennas.

Figure 1-8 depicts the basic geometry of the basic interferometer principle. The geometry consists of two identical antennas separated by distance d. A plane wave along a ray path in the vertical plane, which cuts through both antennas and the transmitter, arriving at an elevation angle ε above the horizon, is received by antenna 1 earlier than antenna 2 due to the time delay. The time delay is proportional to the distance from the wave front to antenna 2 at the moment it reaches antenna 1.

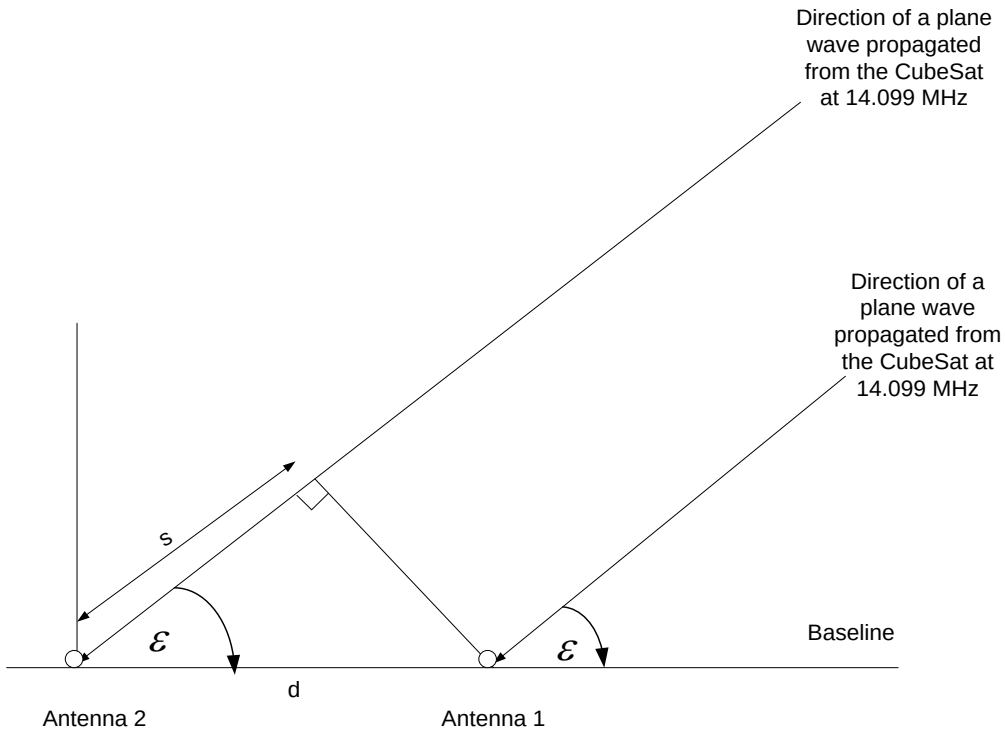

Figure 1-8: Basic geometry to illustrate the interferometric principle for estimating the elevation angle of a ray in the plane of two antennas. The geometry shown is what is applied in the analysis (i.e. that the elevation or azimuth angles at the two antennas are the same) since the

distance between the antennas is so small compared to the distance from the receiver antenna to the satellite, this approximation is justified as demonstrated in the text related to Figure 4-13 (Adapted from Corbin, 2011:11)

In an interferometer, the wave front is assumed to be coming from the source that is far enough that the wave front is planar and the wave arriving at the antennas is a plane wave, travelling at the speed of light. The angle ε can be either the elevation or azimuth, depending on whether we are analysing the situation in the vertical or horizontal plane.

Suppose the source transmits a signal in the plane of the two antennas, at an elevation angle ε whereby two antennas in an array receive the signal $x_1(t)$ and $x_2(t)$, as illustrated by Equation 1.1

$$\begin{aligned} x_1(t) &= A_1 \cos(2\pi f_c t) + n_1(t), \\ x_2(t) &= A_2 \cos\left[2\pi f_c (t - \Delta t)\right] + n_2(t). \end{aligned} \qquad 1.1$$

Here $x_1(t)$ and $x_2(t)$ are the signals received by antenna 1 and antenna 2 respectively, with amplitudes A_1 and A_2, and random additive noise $n_1(t)$ and $n_2(t)$ respectively. f_c is the carrier frequency at 14.099 MHz, and s is the distance from the wave front to antenna 2 at the moment it reaches antenna 1, which is illustrated by Equation 1.2. The distance s is related to the time delay, using Equation 1.3

$$s = d \cos \varepsilon, \qquad 1.2$$

$$\Delta t = \frac{d \cos \varepsilon}{c}. \qquad 1.3$$

Here d is the distance between the antennas in metres, ε is the elevation angle and c is the speed of light (3×10^8 m/s). The phase difference is computed from the time delay and the elevation angle, using Equation 1.4

$$\Delta\psi = \omega \Delta t = 2\pi f_c \frac{d \cos \varepsilon}{c} = \frac{2\pi}{\lambda_c} d \cos \varepsilon. \qquad 1.4$$

Here $\Delta\psi$ is the phase difference between the received signals by the two antennas and λ_c is the wavelength of the incoming signal in metres. The elevation angle is calculated by using Equation 1.5

$$\Delta\psi = \frac{2\pi}{\lambda_c} d \cos \varepsilon$$

$$\lambda_c \Delta\psi = 2\pi \times d \cos \varepsilon$$

$$d \cos \varepsilon = \frac{\lambda_c \Delta\psi}{2\pi} \qquad 1.5$$

$$\cos \varepsilon = \frac{\lambda_c \Delta\psi}{2\pi d}$$

$$\varepsilon = \cos^{-1}\left[\frac{\lambda_c \Delta\psi}{2\pi d}\right].$$

A similar approach is used to resolve ε as the azimuth angle, when the ray path is in the ground plane and the elevation angle is equal to 0˚. In order to resolve the azimuth and elevation angles, the two simple approaches have to be combined. Here at least three antennas are required. The extensions of the above approach to resolve both azimuth and elevation of the incoming signal will be explained in more detail in chapter four.

Several studies have been conducted on algorithms for the estimation of time delays from which the phase difference can be calculated, e.g. Generalised Cross Correlation (GCC), the adaptive Eigenvalue Decomposition (EVD) (Benesty, 2000), the Least Mean Square (LMS) Adaptive Filter (Lin & Chern, 1998) and the CrossPower-Spectrum Phase (CPSP) (Omologo & Svaizer, 1994). Super resolution algorithms have been widely used in various fields such as radar, sonar, radio astronomy and radio direction finding. The multiple signal characteristics (MUSIC) algorithm proposed by Schmidt (1979) is one of the best known super resolution algorithms (Gething, 1991:207). However, estimation of signal parameters via rotational invariance techniques (ESPRIT) improved the performance of the MUSIC algorithm. Although super resolution algorithms give superior results, they fall beyond the scope of this project. The super resolution algorithms are designed to differentiate between sources that are in close proximity.

In this thesis four algorithms that detect the phase difference between signals were investigated, evaluated and compared by means of simulations. The algorithms are based on a single frequency. These algorithms are Zero Crossing (ZC), Fast Fourier Transform (FFT), Cross Correlation (CC) and Cross Power Spectral Density (CPSD).

1.4 Problem statement

The research focuses on the investigation, evaluation and comparison of various signal processing algorithms for estimating the DOA of the HF beacon signal. The HF beacon signal will be received at the crossed loop dipole antennas of the HF DF interferometer array at SANSA Space Science in Hermanus. Algorithms were analysed both analytically and by

means of computer simulation. The algorithm which is least sensitive to noise and simple, and also provides an accurate estimate of the DOA is the best algorithm.

1.5 Objectives of the research

The main objective of the research is to select the best algorithm for estimating the DOA from the phase difference of the HF beacon signal transmitted from ZACUBE-1 (TshepisoSAT). The process was as follows:

- Evaluate the performance of all the algorithms against variables such as noise, accuracy and speed.
- Select the algorithm which provides an accurate estimate of the DOA, taking into account the variables.
- Demonstrate the performance of the algorithms using simulated baseband signals.

1.6 Questions for investigation

The research addresses the baseband signals from the receiver. The following questions guided this research:

The primary research question is: How should the baseband signals, captured by the receiver, be processed in order to obtain the best estimate of the DOA?
Questions which follow on this one are:

- Which parameters affect the performance of each algorithm in the estimation of the DOA?
- Which limiting factors should be taken into consideration when selecting the optimum algorithm?
- How will the space missions benefit from the DOA of the HF beacon signal?

1.7 Research methodology

The following process was followed in order to achieve the research objectives.

Literature review:

- A survey of the literature on various signal processing algorithms that determine the phase difference between HF DF signals was done. The literature included books, journal, articles and white papers.

Development:

- The development of each algorithm was based on the simulated baseband signals from the receiving system.

Implementation and simulations:

- The algorithms were implemented by means of MATLAB. MATLAB is convenient and efficient for code development. It is certainly not the fastest way to run an algorithm. However, MATLAB is flexible and easy to modify.

- The performance of the each algorithm was measured, taking into account the standard deviation (SD) of the azimuth and elevation errors, by varying the input parameters, namely noise, sampling rate and the duration of the signal. The results were measured against the criteria of accuracy and speed.

Selection:

- The algorithm which provided the most accurate estimation within the shortest time was selected.

1.8 Research significance

The HF DF interferometer array at SANSA Space Science in Hermanus will receive HF signals from ZACUBE-1 (TshepisoSAT). The results to be obtained from the HF DF array will be used in the following applications:

- To improve the model of the polar ionosphere which is not fully characterised due to the lack of data.
- The characterisation of the Earth's ionosphere and of space weather radar antennas.
- To assess the feasibility of using a similar design in Antarctica for the calibration of the SuperDARN and to characterise the SuperDARN interferometer in Antarctica (Van Zyl *et al*., 2013:1).
- To help scientists to understand the effects of space weather on HF radio wave propagation.

1.9 Project delineation

This is a project that involves a number of people. The author's contribution was primarily responsible for the selection of the optimal algorithm to determine the phase difference between the signals.

At the time the thesis was submitted, the other group members were still busy with the hardware design of the HF DF array. In addition, the F'SATI ground station operator was still busy with the deployment of the HF antenna that has to transmit the 14.099 MHz. The thesis does not include the simulation of the hardware system of the HF DF. The performance of the algorithms discussed in this thesis is not based on the processing of the real data, but on the simulated baseband signals. The polarisation of the antennas is not taken into consideration; it is beyond the scope of this research.

1.10 Thesis outline

Chapter 1: Introduces the aim of the research, some background information and the thesis outline.

Chapter 2: Presents an overview of the ionosphere and ionospheric effects on the propagation of HF radio waves. The effects of space weather on the propagation of HF radio waves are briefly discussed.

Chapter 3: Reviews algorithms that are used to estimate the DOA of the incoming signals.

Chapter 4: Presents the method that was followed to estimate the DOA of the HF signals from the phase difference between signals and parameters that affect the accuracy in the DOA estimation.

Chapter 5: Describes the implementation of signal processing algorithms for estimation of DOA and the performance of each algorithm as a function of signal-to-noise ratio (SNR). The results obtained from each algorithm are presented.

Chapter 6: Evaluates and discusses the results obtained from the algorithms.

Finally, *chapter 7* offers conclusions and some recommendations for future work in this research field.

CHAPTER TWO: BACKGROUND ON HF RADIO WAVE PROPAGATION

2.1 Introduction

Scientists and spacecraft operators are eager to improve their knowledge of the ionosphere for communication purposes. The data from the HF DF interferometer array at SANSA Space Science in Hermanus will be used to gain a better understanding of radio wave propagation through the ionosphere. The influence of space weather on the ionosphere affects the propagation of HF (3 – 30 MHz) radio waves, thus impacting communication. This chapter gives a brief overview of the ionosphere and its effects on HF radio wave propagation. The propagation of HF radio waves and the effects of space weather on technological systems associated with radio communication, are discussed.

2.2 Overview of the ionosphere

The ionosphere is the ionised region in the upper atmosphere (altitude 50 km to 1500 km) that causes radio waves to be refracted and reflected (McNamara, 1991:17). Due to the reflection of radio waves, the ionosphere plays a crucial role when it comes to HF radio wave propagation via reflection by the ionosphere. Figure 2-1 illustrates the concept of reflection of radio waves by the ionosphere.

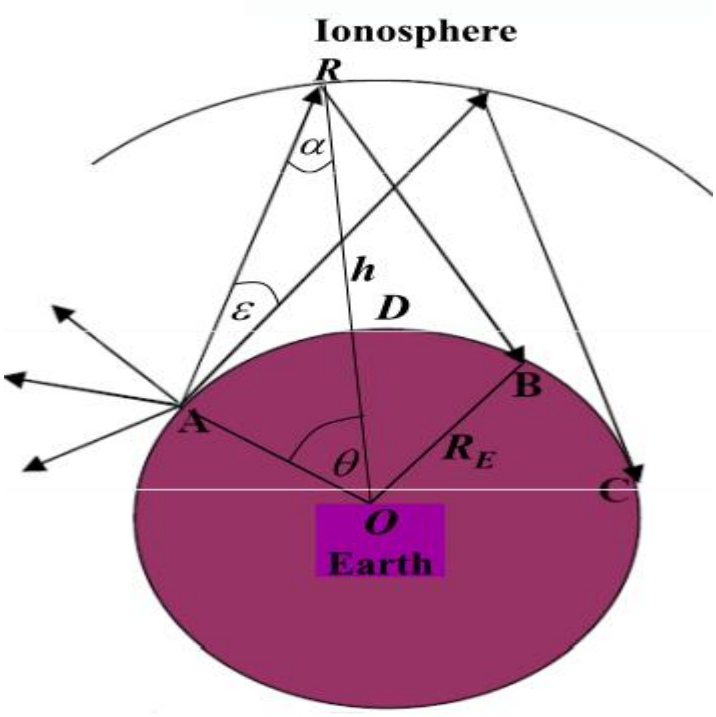

Figure 2-1: The reflection of the HF radio signals by the ionosphere, which allows communication between the transmitting station at A and receiving stations B or C. The height of the ionosphere and the elevation and azimuth angles of transmission resolve whether receiver B or C receives the signal (From Cilliers, 2012:18)

In the context of the HF beacon signal, the transmitting station at A is identified as ZACUBE-1 (TshepisoSAT), transmitting a 14.099 MHz signal to ground. The receiving station B or C refers to either the HF DF interferometer array at SANSA Space Science or the interferometer array at SANAE in Antarctica. The height of the ionosphere and the DOA of the transmission determines which receiver (B or C) receives the signal (Cilliers, 2012:18).

The ionosphere is formed when extreme ultraviolet (EUV) radiation ionises neutral atoms of the Earth's atmosphere (McNamara, 1991:17). The ionosphere acts as conductive layer covering the Earth and acts as a reflector of radio frequencies below 30 MHz.

The ions in and electron density of the ionosphere depend on the altitude. Furthermore, there is a relationship between the electron density and the frequency of reflection of vertically incident waves, referred to as the plasma frequency. The electron density in the ionosphere and the angular frequency of plasma frequency are related by Equation 2.1 (McNamara, 1991:19). The critical frequency is a crucial parameter in HF radio propagation through the ionosphere. For an HF signal to propagate from satellite to ground through the ionosphere, the critical frequency at the given incidence angle must be below the HF beacon frequency. The critical frequency is only the same as the plasma frequency for vertically incident waves. For HF waves at a slant angle, the critical frequency is higher than the plasma frequency.

In HF radio wave propagation, the critical frequency is defined as the maximum frequency by which a radio signal is reflected by the ionosphere. The wave only penetrates the ionosphere when the carrier frequency (f_c=14.099 MHz) is greater than the critical frequency (Rishbeth & Mendilo, 2001:1662). The critical frequency varies with the electron density and the incident angle of the wave. The ionisation density varies with seasons, the time of the day, and solar activity.

$$\omega_p{}^2 = 2\pi f_p{}^2 = \frac{n_e e^2}{\varepsilon_0 m}. \qquad 2.1$$

Here ω_p denotes the plasma resonance frequency in rad/s, n_e represents the electron density in electrons/m^3, e is the electrical charge of an electron (1.6 x 10^{-9} C), m denotes the mass of an electron (9.11 x 10^{-31} kg) , and ε_0 represents the permittivity of free space (8.85 x 10^{-12} Fm^{-1}) (McNamara, 1991:20). The plasma frequency expressed in Hz is defined by Equation 2.2,

$$f_p = 9\sqrt{n_e[m^{-3}]}, \qquad 2.2$$

where f_p denotes the plasma frequency in Hz and n_e represents the electron density in electrons/m^3. For each layer in the ionosphere there is a critical frequency. The critical frequency is defined as the highest frequency that will be reflected by any given layer for a vertically incident wave. The critical frequency for the E , F1 and F2 layers are denoted by f_oE, f_oF1 and f_oF2 respectively.

2.3 Structure of the ionosphere

The ionosphere is made up of four different layers namely D, E, F1 and F2. The structure of the ionosphere is determined by seasonal variations, diurnal variations and sunspot number variations (McNamara, 1991:22). Figure 2-2 illustrates the different layers in the ionosphere at certain altitudes. During the day, all four layers are present as shown in Figure 2-2, however, at night time the D, E and F1 layers disappear, leaving only the F2 layer, available for communication. At night this is known as the F region, as illustrated in Figure 2-2.

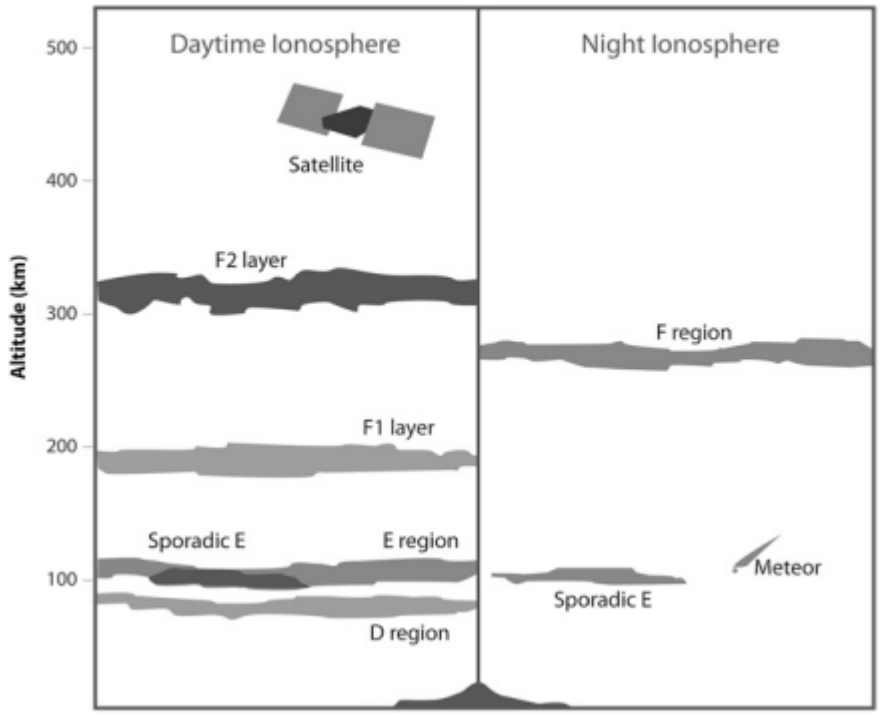

Figure 2-2: The structure of the ionospheric layers during the day and at night (From Zolesi & Cander, 2013:40)

The ionospheric layers are explained in greater detail in the next section.

D-Layer: The D layer is the lowest region of the ionosphere, and is associated with the altitude range of 50 – 90 km. This layer plays a role of an attenuator, at low frequencies. The level of ionisation is low since the nearer the Earth, the more dense the neutral atoms in the

D-layer. The X-rays which are the primary cause of the ionisation of the D-layer, are absorbed in the higher layers, and only a small percentage penetrates to the D-layer to cause ionisation. Signals at higher frequencies go through the ionosphere and are less attenuated. When the sun sets, the D-layer disappears because of the fast process of recombination of ions (Poole, 1999).

E-layer: The E layer exists at heights of about 90 – 110 km. Another name for the E layer is Kennelly-Heaviside layer, since this layer was named after the two men who first came up with the proposal of its existence. The recombination of ions in the E layer occurs at a faster rate than the recombination in the F-layer after sunset and the layer will almost disappear by midnight.

F1-layer: The F1 layer exists at altitudes in the range of 175 – 200 km and it is only formed during the day. The waves that penetrate the E layer (3 – 30 MHz) are able to penetrate this layer (Barringer & Springer, 2008).

F2-layer: The F2 layer is located at an altitude between 250 – 400 km .The rate of ionisation is higher than in the other layers and changes during the day. The F2 layer plays a major role in HF radio propagation, because it is available 24 hours of the day and its altitude is higher compared to the other layers. Since it reflects the frequencies that are in the HF range, it can be used for long-distance ground-to-ground communication (Zolesi & Cander, 2013:43).The transmission frequency from ZACUBE-1 (TshepisoSAT) should be greater than the critical frequency (f_oF2) of the ionosphere for at least some incident angles, for the signal to penetrate the ionosphere (Minko, 2013:28).

2.4 Observing the ionosphere

Several methods have been used to explore the ionosphere. The ionosonde is one of these. The ionosonde measures the electron density of the bottom side of the ionosphere. Figure 2-3 illustrates the ionosonde at SANSA Space Science in Hermanus, South Africa. The significance of having the ionosonde co-located with the HF DF array at SANSA Space Science in Hermanus, is that the measurements by the HF DF array incoming can be compared with those of the ionosonde and dual frequency global positioning system (GPS) receivers near Hermanus. The ionosonde data and dual-frequency GPS receiver's data will be used to improve the accuracy of the international reference ionosphere (IRI) model. The IRI model is used for ray tracing from satellite to receiver. Ionospheric models based on local ionospheric measurements by means of the ionosonde, can be tested by observation of refracted of radio waves from the HF beacon. (Agaba, 2012).

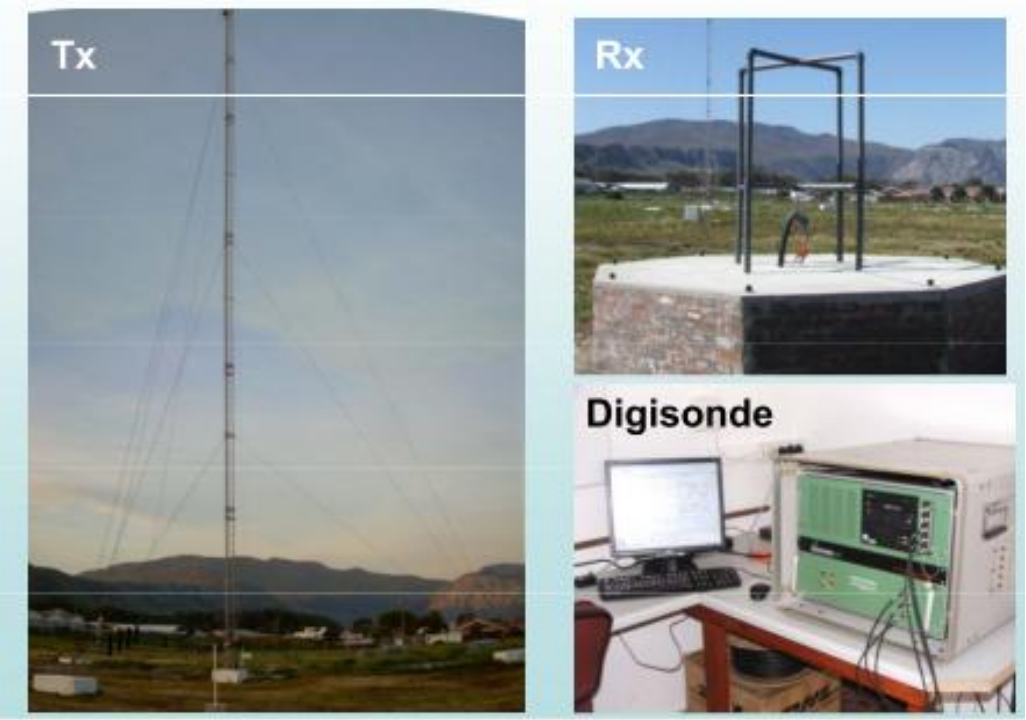

Figure 2-3: The ionosonde at SANSA Space Science in Hermanus consists of a transmitter with a vertical transmitting antenna of 30 m and a receiver array made up of four crossed loop dipole antennas and a digisonde located inside a nearby building (From McKinnell, 2008)

However, the ionosonde investigates the ionosphere from the bottom side only, since it relies on reflections from the ionosphere for its operation. Satellites can be used to investigate the ionosphere from the top side. The data to be acquired by the HF DF interferometer array at SANSA Space Science will allow scientists to test and improve models of the electron density in both the top side and bottom side of the ionosphere.

Ionospheric models are used to forecast the behaviour of the ionosphere and to predict the propagation of HF radio waves in the ionosphere. Ray tracing techniques are being used to model the propagation of radio waves through the ionosphere. Ray tracing determines whether a certain frequency at a specific time and date will penetrate the ionosphere. Agaba, (2012) modelled a ray path of an HF radio beacon signal from a Low Earth Orbit (LEO) CubeSat, using a spherical Earth multilayer model for the ionosphere. The ray path was traced from the CubeSat to ground. Figure 2-4 shows that all the indicated ray paths from the CubeSat reach the ground (Agaba, 2012).

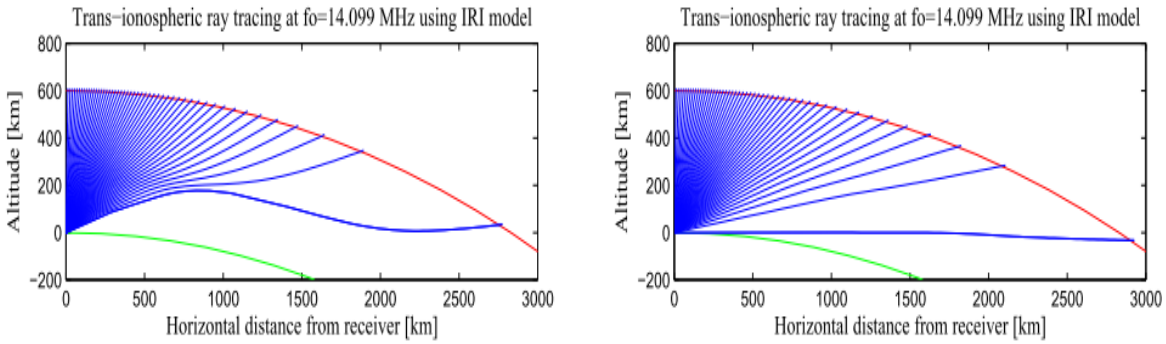

Figure 2-4: Simulated ray paths for the spherical Earth multilayer top-to-bottom model of a trans-ionospheric HF signal from the beacon on the CubeSat, transmitting at 14.099 MHz to the receiver, for midsummer (left) and midwinter (right) at an altitude of 600 km. This model is based on the IRI. The ray paths are dependent on the electron density of the ionosphere (From Agaba, 2012:60)

2.5 HF Radio Propagation

In this thesis the propagation of the beacon signal from the CubeSat is based on the trans-ionospheric propagation of HF radio signals. Trans-ionospheric radio signals take place when the radio signal propagates from the surface of the Earth (ground-based station) to moving satellites in space and vice versa through the ionosphere (Danilkin, 1997:31). The HF transmitter on board the satellite transmits an HF signal. The signal will be received by the HF DF array in Hermanus and at SANAE Antarctica.

Propagation of radio waves in the context of the HF beacon is the advance of the wave front of the radio wave from the transmitter on board the satellite to receivers on the surface of the Earth through different parts of the atmosphere. The radio wave is launched into space by means of a transmitting antenna comprising a 10 m length of wire.

2.5.1 Doppler shift

The HF beacon signal received at the receivers is different from the HF beacon signal transmitted, due to the Doppler shift. The Doppler shift is defined by Equation 4.6. The maximum Doppler shift frequency of the 14.099 MHz was calculated as ±316.47 Hz for a special case and ±354.1 Hz for the general case, when the satellite is on the horizon. The Doppler shift is passed to the baseband frequency through the process of multiplication by a local oscillator signal at a nominal offset of 1 kHz from the carrier frequency. Doppler shift frequency has to be taken into account for the HF beacon signal transmitted from ZACUBE-1

(TshepisoSAT). Details of the Doppler shift calculation and its effect on the DOA estimation are given in chapter four.

2.5.2 Noise

The noise that was added to the baseband signal represents various sources of noise, including additive noise along the propagation path, ionospheric scintillation, phase jitter in the receiver's ADC clock, finite word length in the ADC, and other unknown causes. The noise degrades the true estimated DOA of the incoming signal.

Ionospheric scintillation which is one of the sources of the noise is a variation in the signal strength of a trans-ionospheric signal, for example from satellite to ground station. Scintillation is caused by small variations of the ionosphere. The variations in phase, amplitude and polarisation angle of radio signals are called scintillations (Allnutt, 1989:72). In addition, the variations in phase, amplitude and polarisation angle can change the DOA of radio signals. These variations occur at a fast rate. The level of scintillation depends on factors such as location of the earth station, the state of the ionosphere and the latitude (Kintner *et al*., 2007:1).

In simulation of the algorithms, scintillation is represented by the Gaussian noise added to the simulated baseband signals. Central Limit Theorem is the main reason why noise is assumed to be Gaussian noise. This is because, in simulations random variables were used to represent the noise added to the baseband signals. Random variables are sampled from different distribution and if the random variables carry various sources of noise on top of the baseband signals, then when the number of run increases, the error distribution start to look Gaussian. From the central limit theorem, it is known that in point-to-point radio communication systems, the composite effect of many (almost) independent noise sources (e.g. thermal noise, shot noise, flicker noise, etc.) should approach a Gaussian distribution (Shomorony & Avestimehr, 2013). On the basis of the central limit theorem, Gaussian noise was assumed to be representative of the combined effect of all the noise sources that contribute to the noise on the baseband signals.

2.5.3 Refraction of radio waves

Refraction is defined as the bending of radio waves when they enter a new medium, where the speed of propagation changes. The bending of the waves is always toward the normal in the medium with a lower speed of propagation (Snell's law). Snell's law is given in Equation 2.3, while the refractive index in the ionosphere is given by Equation 2.4. Figure 2-5 illustrates the refraction of a radio wave.

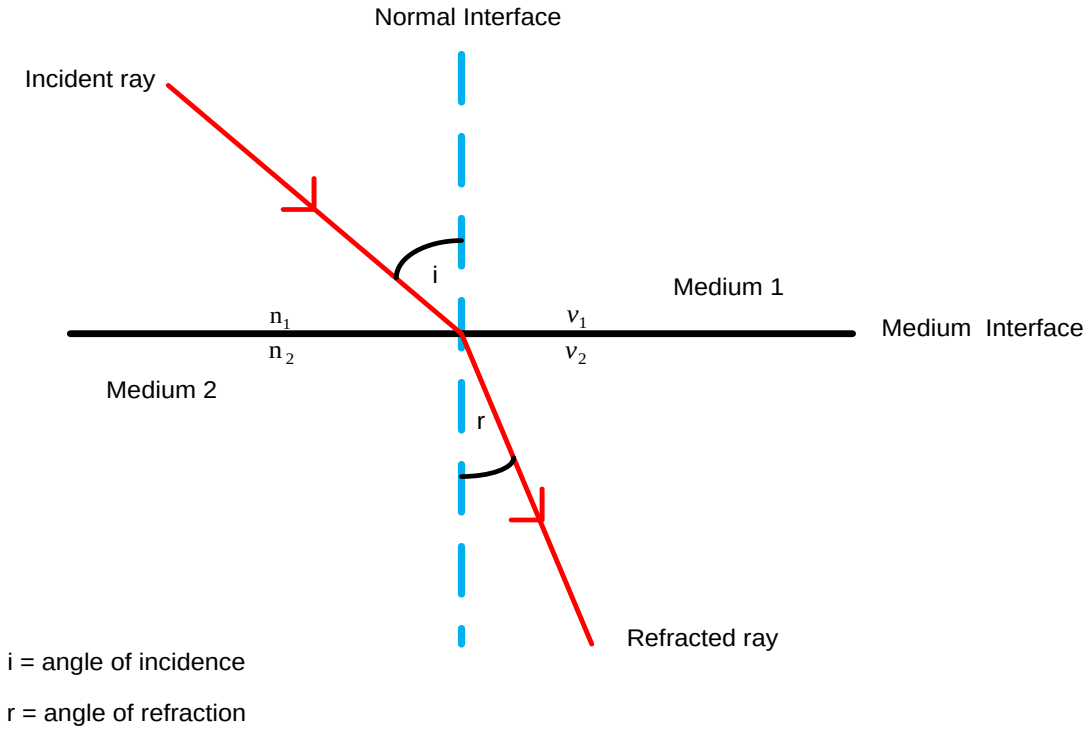

Figure 2-5: Illustration of the refraction of a radio signal. The propagation angle changes when the wave enters different media (Adapted from Agaba, 2012:18)

$$\frac{\sin\ i}{\sin\ r} = \frac{v_1}{v_2} = \frac{n_1}{n_2}, \qquad 2.3$$

where i represents the angle of incidence, r is the angle of refraction, n is the refractive index and v is the phase velocity of the signal.

$$n = \sqrt{1 - \frac{(f_p)^2}{(f_c)^2}}, \qquad 2.4$$

where:

f_p = electron density plasma frequency in MHz

f_c = frequency of the incident ray (14.099 MHz)

The density of the ionisation of the layer, the frequency of the radio wave and the angle at which the wave enters the layers, are the three main factors that affects refraction in the ionosphere. The frequency of the radio waves is the most critical for this research. Reflection occurs only if the frequency of the wave is below the critical frequency for the particular angle of incidence. For low angles of incidence, reflection can occur even if the frequency is much higher than the plasma frequency (Allnutt, 1989:64).

In the next section, certain parameters that determine whether the radio wave will or not propagate along a given path are discussed.

2.5.4 Maximum Usable Frequency (MUF) and Lowest Usable Frequency (LUF)

The MUF is defined as the maximum frequency that allows a radio wave to arrive at a particular destination for a given path. The MUF for a certain path varies throughout the day, with seasons and with solar cycle (McNamara, 1991:42). The MUF depends on the angle of incidence and the critical frequency of the ionosphere for a given layer. The critical frequency is a figure of merit that indicates the state of the ionosphere. When the wave enters the ionosphere in a vertical direction the critical frequency is equal to f_oF2. For the $\varphi > 0$, the MUF of a certain path for point-to-point communication between a terrestrial transmitter and a terrestrial receiver is given by Equation 2.5

$$\text{MUF} = f_{\text{cr}} / \cos\varphi . \qquad 2.5$$

Here f_{cr} is the critical frequency for the F2 layer, and φ is the angle of incidence which is related to the elevation angle by $\varphi = 90^{\circ} - \varepsilon$ (Kraus & Fleisch, 1984). The lowest usable frequency (LUF) is the frequency where the signals drop below a certain minimum strength over a certain ground-to-ground path for reception. The signal from a terrestrial transmitter will penetrate the ionosphere, if the frequency of transmission is higher than the MUF for ground-to-ground HF communication. However, if the frequency is lower than the LUF for ground-to-ground HF communication, the signal is absorbed in the D layer (Tshisaphungo, 2009: 13). Figure 2-6, illustrates the refraction and reflection of radio waves at different frequencies.

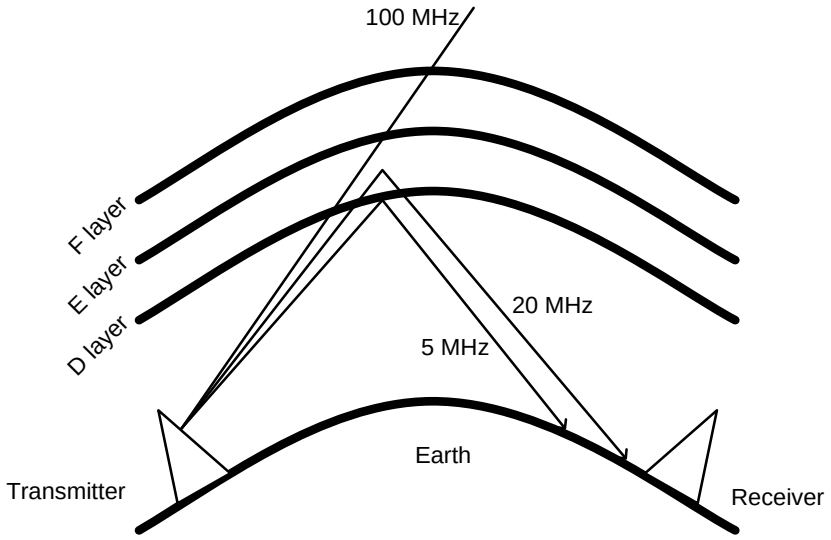

Figure 2-6: The refraction and reflection of radio waves at different frequencies. The highest frequencies penetrate the ionosphere, while the lowest frequencies are absorbed by the D layer (Adapted from Introduction to HF Radio, 2012)

For the trans-ionospheric HF radio communication from a satellite in the LEO, the LUF is defined as the lowest frequency that will pass through the ionosphere at a given incident angle. For satellite-to-ground communication the LUF is the same as the MUF for ground-to-ground communication. Signals transmitted through the ionosphere from the ground are refracted to the Earth if the transmission frequency is below the MUF for ground-to-ground communication. Likewise the signals transmitted from the satellite to the Earth are refracted to space if the transmission frequency is lower than the LUF for satellite-to-ground communication, and they are not able to reach to the ground (Minko, 2013:26).

The peak electron density of the ionosphere and the incident angle of the ray path penetrating the ionosphere are the two factors that relate the LUF (satellite-to-ground) and MUF (ground-to-ground). The critical frequency of the F-layer, which is known as f_oF2, is the MUF of the vertical incident signal. The f_oF2 is related to the maximum electron density in the ionosphere, $NmF2$ by Equation 2.6

$$f_oF2 = \sqrt{80.6\ (NmF2)}\ . \qquad 2.6$$

Here f_oF2 is the critical frequency of the F-layer in Hz and $NmF2$ is the maximum electron density in the ionosphere expressed in electrons/m^3 (Minko, 2013: 28).

Figure 2-7 demonstrates satellite-to-ground communication, which involves four steps as depicted in Figure 2-7. The frequency of transmission, path length between the transmitter

and receiver and the antenna elevation angle are dependent upon each other in HF propagation.

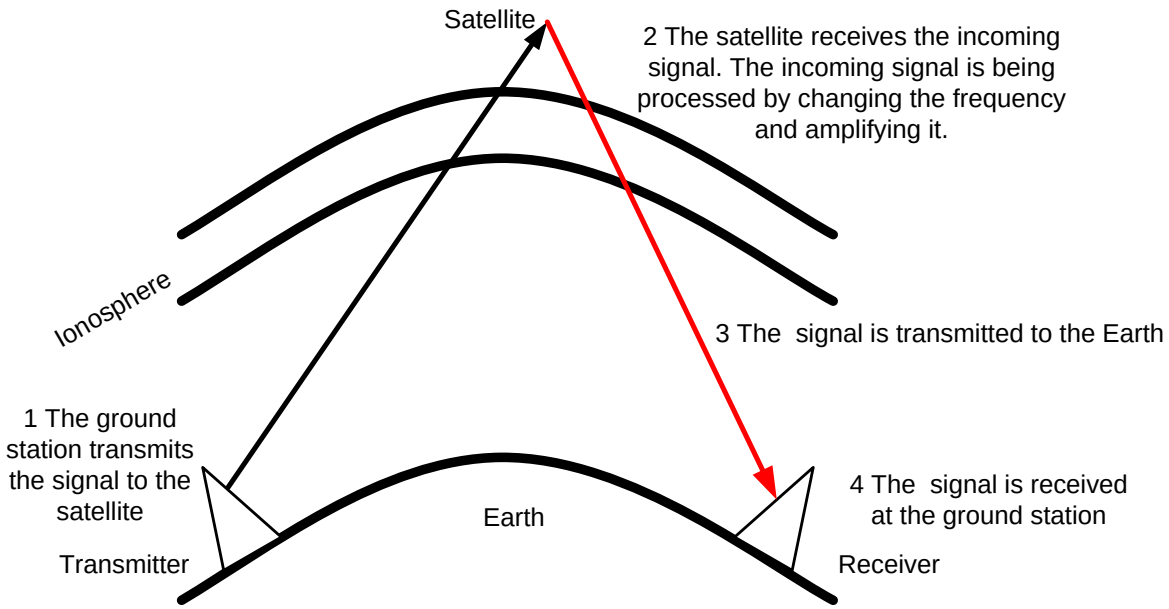

Figure 2-7: A typical communication systems used for ground-to-ground communication via satellite. In the case of the CubeSat beacon, the only relevant signal path is from satellite to ground since the signal originates from the satellite (Adapted from Intelsat, 2013)

2.6 Space weather

Space weather describes the conditions on the sun and in space that affects technological systems in Space and on the Earth (Goodman, 2005:2). Space weather influences space-borne and ground-based technological systems; furthermore, it can be dangerous to human health (Koons *et al*., 1999). Figure 2-8 depicts some of the technological systems that can be affected by space weather.

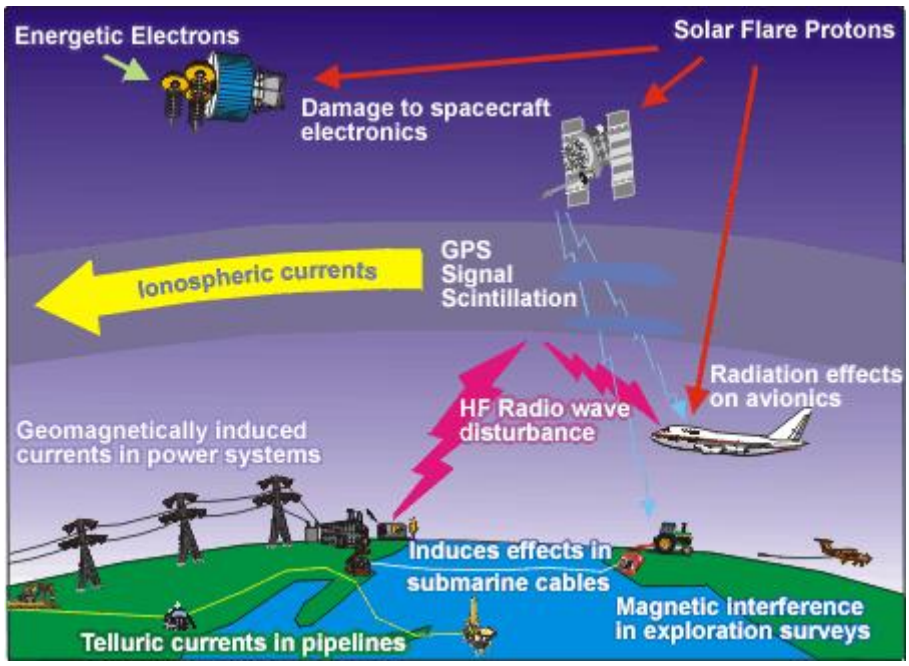

Figure: 2-8: Effects of Space weather on technological systems[4]

2.7 Summary

Although the ionosphere is considered the main resource for long-distance communication by means of HF radio, its influence on HF radio wave propagation from satellite-to-ground is crucial in the context of mission success of the proposed CubeSat-borne HF beacon. However, the variability in the ionosphere affects HF communication systems that depend on ionospheric reflection and refraction. The variability of the ionosphere affects how it attenuates, absorbs, reflects, and refracts radio waves. Short-term fluctuations of the electron density in parts of the ionosphere can lead to phase and amplitude scintillation on trans-ionospheric radio waves. The background material on the ionosphere presented here and the effects of the ionosphere on HF propagation, help to determine criteria for the selection of the best algorithm for retrieving possible estimates of the DOA from the HF beacon signal. The next chapter reviews existing techniques and algorithms for DOA estimation.

[4] http://www.spaceweather.gc.ca/tech/se-eng.php

CHAPTER THREE: ALGORITHMS FOR THE ESTIMATION OF DIRECTION OF ARRIVAL

3.1 Introduction

This chapter contains a review of the literature on techniques for direction finding systems, such as amplitude comparison and phase comparison. In the current context, the estimation of the direction of arrival is based on resolving the phase difference between signals observed by means of an array of crossed loop antennas arranged in an L-shaped configuration. This chapter reviews several signal processing algorithms that estimate the phase difference between two signals, using the time and frequency domains.

3.2 DOA techniques

Two techniques that are commonly used for DOA estimation are amplitude comparison, such as in radar monopulse systems, and phase comparison, such as in interferometers. The phase comparison technique offers the advantage of greater accuracy; however, amplitude comparison is more often used due to the lower cost and because it is less complex. Both techniques require a minimum of three antennas to estimate both the azimuth and elevation of the DOA. More accurate results can be obtained by increasing the number of antennas in the array (Neri, 2006:325).

Amplitude comparison algorithms for DF are mostly easy to design, however they do not perform very well due to amplitude measurement errors. Phase comparison performs very well and presents accurate results, however, antenna calibrations are required to minimise phase measurement error (Kawase, 2007:443). According to Silva *et al*., (2011), the phase comparison technique gives more accurate results than amplitude comparison, although its design is more challenging than for amplitude comparison.

3.2.1 Amplitude comparison techniques

The amplitude comparison technique uses more than two directional antennas to determine the DOA. The DOA can be computed by analysing the relative amplitudes of the signals received by different antennas (Erad *et al*., 2013). The incoming signal is received individually by the antenna elements, with overlapping beams. It is often required that the antennas used for amplitude comparison are able to produce identical beam patterns. According to Gething (1991), the antennas that are used in amplitude comparison have correspondent phase centres and identical radiation beam patterns. Figure 3-1 illustrates the squinted beam pattern of the antenna used for amplitude comparison. In most cases, the

distance between the antenna elements is equal to the bore sight axis at angles $+\theta$ (+ 45˚) and $-\theta$ (– 45˚), respectively, in order to provide a full coverage of 360˚.

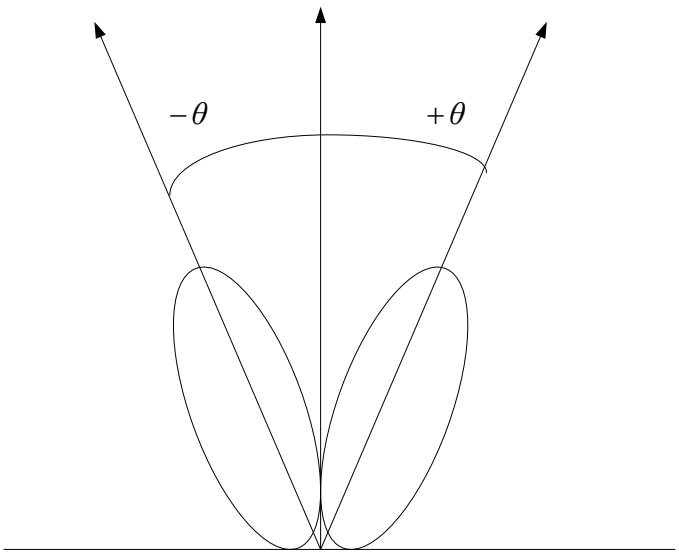

Figure 3-1: The squinted beam pattern of the antenna elements used for amplitude comparison. The antenna elements are equally spaced to provide a full coverage of 360˚ (Adapted from Corbin, 2011)

Amplitude comparison techniques are very cheap to implement, however, their degree of accuracy in DOA estimation is very low, because they depend on the strength of the signal (Shi & Zhang, 2010). The accuracy of amplitude comparison techniques is in the range of 3˚ to 10˚ root mean square (rms) (Neri, 2006:326). The accuracy becomes progressively worse at lower frequencies, because practical implementation does not accommodate large antennas. The accuracy is compromised, because of the inability to measure small differences in amplitude between the signals received at each antenna element. However, both poor accuracy and sensitivity can be improved by increasing the number of antennas in an array (Neri, 2006:327).

3.2.2 Phase comparison techniques

Phase comparison techniques, also known as interferometer techniques, are used when more accurate estimates of the DOA is needed, compared to that which is achievable with amplitude comparison methods. Interferometry has been widely used for DOA estimation, because it offers advantages such as high DF precision, high speed, and a simple algorithm (Cheng *et al*., 2013:1). The interferometer uses time delay to estimate the phase difference between signals received at the antenna elements. For phase comparison the antennas use parallel beams and distinct phase centres (Gething, 1991:123).

The distance between the antennas elements of an interferometer array needs to be calculated very carefully. When the distance is larger than half the wavelength of the

incoming signal, the phase difference will also be sufficiently large in order to allow phase difference resolution, however, there will be phase difference ambiguity. Ambiguities, which are called grating lobes, usually occur when the distance is larger than half a wavelength of the incoming signal. In such a case, multiple values of DOA will produce the same phase difference in multiples of 2π (Kawase, 2007:443). However, placement of more antennas within an array may be used to resolve the ambiguities (Akers, 2000). It can be seen that the phase difference, $\Delta\psi = \omega\Delta t = 2\pi f_c \frac{d\cos\varepsilon}{c} = \frac{2\pi}{\lambda_c} d\cos\varepsilon$, is clearly a function of the elevation angle (ε), frequency and the distance between the antenna elements. Figures 3-2 and 3-3 illustrate how the phase difference between array elements change, when the distance is half a wavelength $\frac{\lambda_c}{2}$ and λ_c respectively.

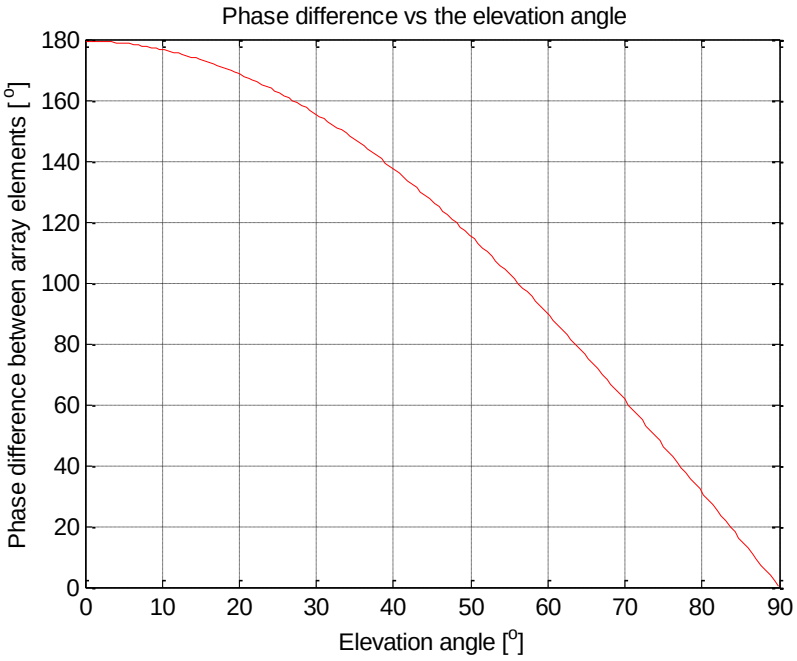

Figure 3-2: Phase difference between array elements received by the two antennas in Figure 1-8 versus elevation angle for the case where the distance is exactly half a wavelength at the carrier frequency

In Figure 3-2, it can be clearly seen that at the elevation angle of 90˚ the phase difference goes to 0˚. At the elevation angle of 90˚, the signal arrives almost at the same time at both antennas. Hence, there is no time delay between the signals, resulting in no phase difference being estimated.

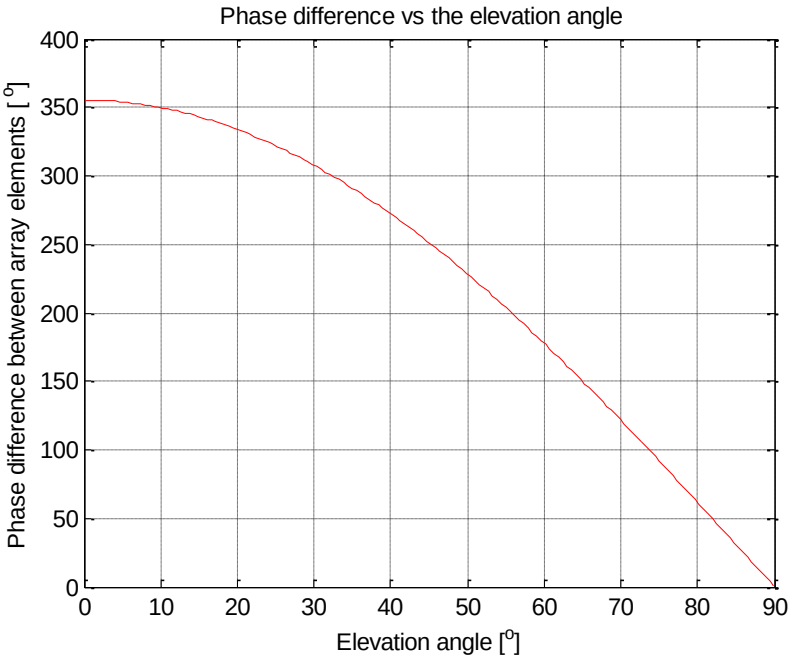

Figure 3-3: Phase difference between array elements received by the two antennas in Figure 1-8 versus elevation angle for the case where the distance is equal to a wavelength

Figure 3-3 shows the phase difference versus elevation angle for the special case where the spacing between the two antennas is equal to λ_c. The phase difference jumps from 180˚ to 360˚ when the distance increases to a wavelength. When the distance is equal to a wavelength, the same phase difference will be estimated, but in multiples of 360˚.

The interferometer method for DOA estimation achieves accuracy in the range of 0.1˚ to 1˚. Interferometry is resistant to multi-path effects, but it has some drawbacks (Neri, 2006:327). The radio frequency (RF) cables that join the receiving antenna to the unit that measure phase, may cause some phase errors due to changes in temperature of the cable, which will degrade the accuracy of the DOA information (Kawase, 2007:443). The two DOA measurement techniques are compared in Table 3-1.

Table 3-1: DOA measurement techniques

	Amplitude comparison	Phase comparison
Antenna configuration	4 to 6 equally-spaced antenna elements for 360˚ coverage	At least 2 or more antenna elements
Typical DF accuracy	3˚ to 10˚ root mean square (rms)	0.1˚ to 3˚ root mean square (rms)
To improve DF accuracy	Decrease the bandwidth of the antenna and increase the squint angle	Increase the distance between the outer antennas in the array
Sensitivity to multipath/reflections	Highly sensitive, causes large errors in DOA estimation	Low sensitivity, interferometry can accommodate large errors

After comparison of the two DOA estimation techniques, the phase comparison technique was selected for DOA estimation of the HF beacon signal.

3.3 Signal processing algorithms on the phase difference estimation

The DOA is computed from the phase difference between the signals received at several antennas, which is derived from the time delays. There are some simple time domain methods and frequency domain methods that can be used to find the phase difference between two signals. However time domain and frequency domain methods resolve the phase difference in different ways. Several methods that use time domain and frequency domain to estimate the phase difference were investigated. Time domain uses time delay estimation that will be related to phase difference, while the frequency domain methods estimate the phase difference from the frequency spectrum (Changlin, 2006:394). Changlin (2006:396) observed that both frequency domain and time domain can be used to estimate the phase difference between the signals, however the frequency domain gives more accurate results.

Time delay estimation:

Time delay estimation is an area of research that has been investigated since the development of radar during the 1930s (Chen *et al*., 2003:207). Time delay is widely used in radar communication, acoustics, sonar, locating radiation sources and geo-physics (Chen *et al*., 2003:207). Khaddour (2011:31) distinguishes between three kinds of time delay estimation:

- Time difference of arrival (TDOA), where the systems uses the time difference of arrival between the signals to locate the source.
- DOA, which uses the phase difference between the signals to locate the source.
- Energy based, which uses the sound energy at various sensor to locate the source. “The energy of the sound wave decreases, when the sound wave propagates in the air”.

Time delay is the time that the wave needs to reach a further point from the source. The relationship between the time delay and the phase difference is defined by Equation 3.1. Figure 3-4 is a geometrical representation of two wave fronts. The length of the arrows represents distance.

$$\Delta\psi = 2\pi f \times \Delta t \,. \qquad 3.1$$

Here $\Delta\psi$ represent the phase difference and Δt denotes the time delay.

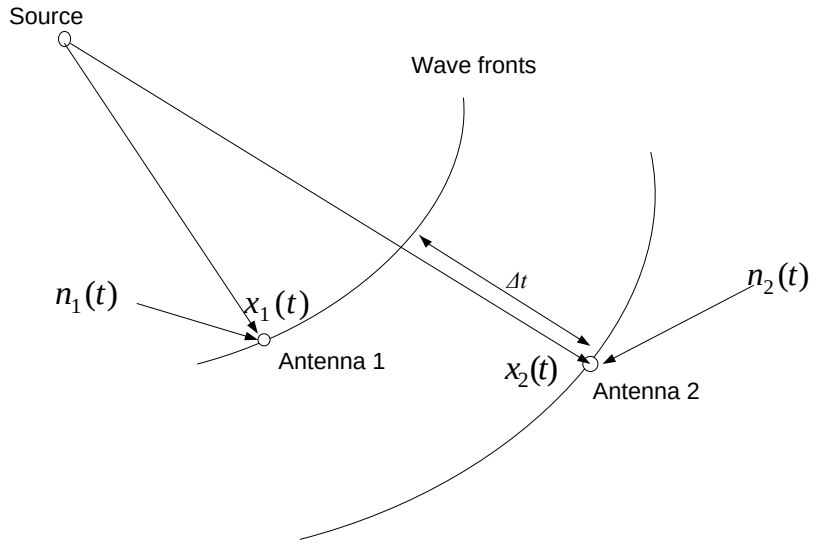

Figure 3-4: Geometrical drawing of two wave fronts with the lengths of the arrows representing distance (Adapted from Zhang *et al*., 2005:3)

Suppose the source transmits a signal $s_1(t)$, where antenna 1 and antenna 2 in an array receive the signals $x_1(t)$ and $x_2(t)$ respectively, as in Equations 3.2

$$\begin{aligned} x_1(t) &= s_1(t) + n_1(t), \\ x_2(t) &= s_1(t - \Delta t) + n_2(t). \end{aligned} \qquad 3.2$$

Here $n_1(t)$, and $n_2(t)$ are the noise signals that are added to the transmitted signals. The time delay is represented by Δt. The time delay is then be transformed to phase difference and DOA.

3.3.1 Cross correlation

Cross correlation is a signal processing algorithms that is commonly used for estimating the time delay between two received signals, and hence also applies to the estimation of time delays for finding DOA. Cross correlation is a technique that measures the degree to which the signals are correlated. Cross correlation between two signals is the correlation of one signal with the time delayed-version of another signal. The time delay is obtained, from the time lag that maximise the cross correlation function (Paulose *et al*., 2013:934).

Figure 3-5 depicts a block diagram of a cross correlation processor, which finds the largest peak in the output of the cross correlation between $x_1(t)$ and $x_2(t)$, by adjusting the value of τ to the value that maximises the cross correlation between $x_1(t)$ and $x_2(t)$.

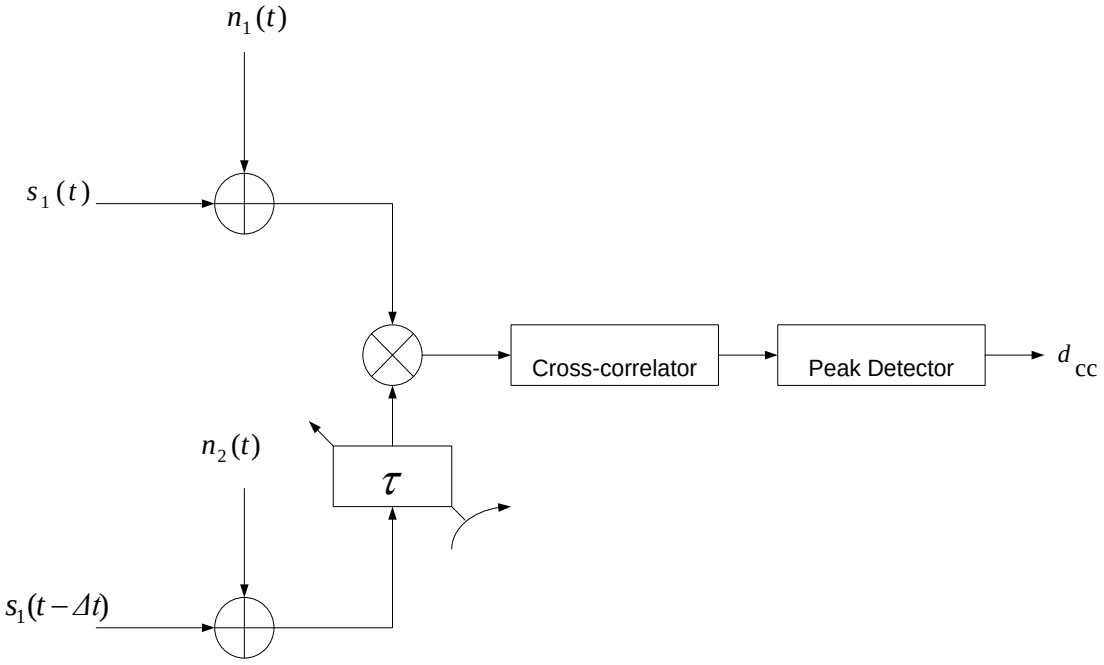

Figure 3-5: A block diagram of a cross correlation processor. τ is adjusted to maximize the cross correlation between $x_1(t)$ and $x_2(t)$ (Adapted from Zhang *et al*., 2005:6)

The cross correlation between $x_1(t)$ and $x_2(t)$ is defined by Equation 3.2, and the time delay is expressed by Equation 3.3.

$$R_{x1x2}(\tau) = E\left[x_1(t)\, x_2(t-\tau)\right], \qquad 3.2$$

$$d_{cc} = \arg \max \left[R_{x1x2}(\tau)\right]. \qquad 3.3$$

Here E denotes the expected value. The value of the argument τ, which maximises Equation 3.3, provides the estimate of the time delay, which can be related to phase difference to compute the DOA (Knapp & Carter, 1976).

Cheng *et al*., (2013), proposed a two-dimensional correlation interferometer algorithm that is based on dimension separation. In wideband DF systems, the range of incoming frequencies becomes much wider, so in order to capture all the incoming signals, DF systems based on multi-channels are used. The incoming signal appears in each channel, thus the DF is performed on each channel. However, the complexity of the DF grows as the channel number increases. The algorithm proposed by Cheng *et al*., (2013) addresses the problem of

reducing the complexity of correlation in the two-dimensional DF system where both azimuth and elevation angles are estimated.

The study by Cheng *et al*., (2013:7) was based on the M-element uniformly spaced circular array (UCA), as shown in Figure 3-6, where R is the radius of the array.

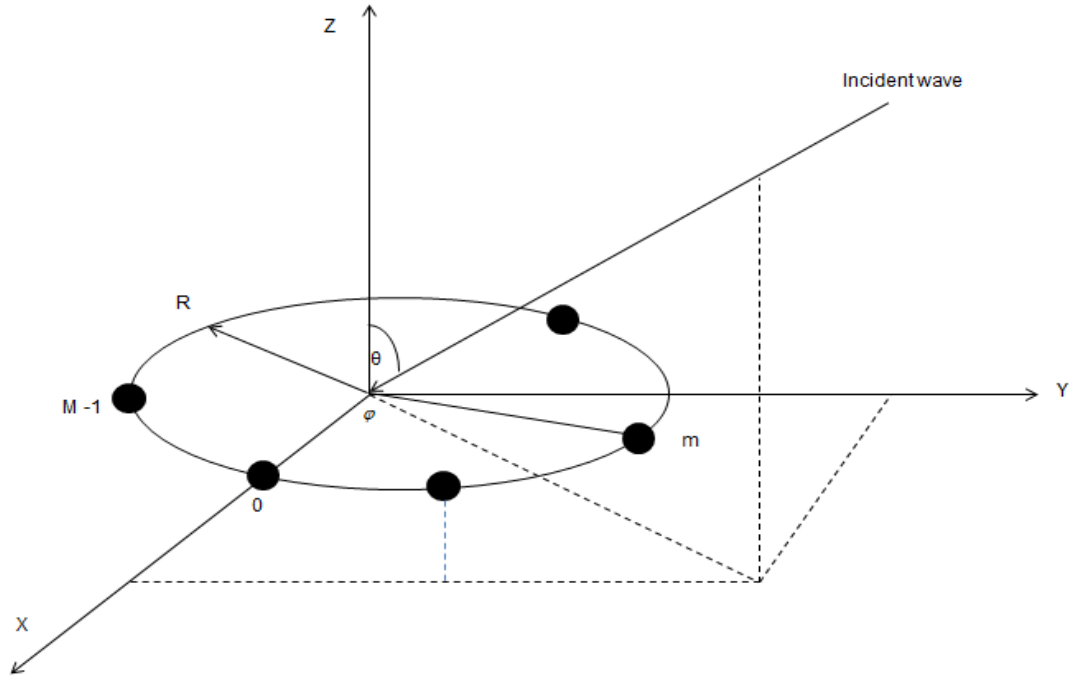

Figure 3-6: The layout of the uniformly spaced circular array of M elements with radius R. One of the elements lies on the x-axis (Adapted from Cheng *et al*., 2013:2)

The incoming signal received by the array in the direction of (φ, θ) is the incident wave, the azimuth angle is denoted by φ and the angle between the zenith and the ray path is denoted by θ. The centre of the array is denoted as the reference point. The received signal of the element m is expressed by Equation 3.4

$$r_{\mathrm{m}}(t) = A\ \cos(\omega_{\mathrm{i}} t - \phi_{\mathrm{m}} + \phi)\,. \qquad 3.4$$

Here A is the amplitude, $\omega_{\mathrm{i}} = 2\pi f_{\mathrm{i}}$, f_{i} is the frequency of the incoming signal. The comparable wavelength of the signal is $\lambda = \dfrac{c}{f_{\mathrm{i}}}$, where c denotes the speed of light in m/s, ϕ_{m} is the phase of element m relative to the reference point and is defined by Equation 3.5

$$\varphi_{\mathrm{m}} = \frac{2\pi R}{\lambda} \sin\ \theta \cos\left(\varphi - \frac{2\pi}{M} m\right) \qquad 3.5$$

Cheng *et al*., (2013: 3), states that the phase difference between various elements in an array corresponds to the phase difference vector. The correlation interferometer determines the DOA of the incoming signal by comparing the measured phase difference vector with the vectors in the sample database. The phase difference vectors correspond to a pair of angles which define the sample database. The purpose of the correlation process is to determine the phase vector that correlates well with the measured vector of the sample database, in which the pair of the angle correlated vector is considered the estimated DOA. Cheng *et al*., (2013:5) used the following steps to estimate the DOA (azimuth and elevation angles).

1. An arbitrary fixed-elevation angle was selected, with all phase difference vectors corresponding to the chosen arbitrary elevation angle, but different azimuth angles in the sample database.
2. The correlation coefficient of the measured phase difference vector and all the selected phase difference vectors in step 1 were calculated.
3. The azimuth angle that obtains the maximum correlation coefficient with the measured phase difference vector as an estimated azimuth angle was selected.
4. All the phase difference vectors which share the same azimuth angle selected in step 3 were calculated.
5. The correlation coefficient between the measured phase difference vector and the selected phase difference vectors in step 4, was calculated.
6. The elevation angle corresponding to the phase difference vector which has the maximum correlation coefficient was selected.
7. Execute two-dimensional interpolation to obtain the final estimates of azimuth and elevation angles.

A Gaussian random signal with zero-mean variable was used to represent the noise in the simulations.

Three algorithms were used by Cheng *et al*., (2013:7) to evaluate the performance of the algorithm they proposed, namely the conventional correlation interferometer (Algorithm 1), dimensional separation-based correlation interferometer algorithm without interpolation (Algorithm 2) and the dimension separation-based correlation interferometer algorithm with interpolation (Algorithm 3).

The evaluation of the proposed algorithm by Cheng *et al*., (2013:7) was done for an incident wave which arrives at a 7-element UCA with a radius of 1 m, with an azimuth angle of 103˚ and elevation of 42˚, a carrier frequency of 70 MHz, over an average of 2000 Monte Carlo simulations. The performances of the algorithms were evaluated by means of the root mean

square error (RMSE). The results show that the RMSE of azimuth and elevation estimates decreases as the SNR increases for all three algorithms. However, the RMSE of estimated azimuth and elevation for algorithm 3 converges to smaller degrees of errors. It was found out that the proposed algorithm by Cheng *et al*., (2013) offers better results with interpolation; interpolation was used to reduce the errors. Algorithm 3 was selected as the choice as far as precision is concerned. Efficiency was also compared. The conclusion was that the efficiency of the algorithm speeds up, as the size of the sample database increases.

3.3.2 Generalised Cross Correlation (GCC)

The Generalised cross correlation algorithm is a modified, improved version of the cross correlation algorithm. It was proposed by Knapp & Carter (1976). High accuracy and low computation cost are the advantages that the GCC algorithm offers. Figure 3-7 shows the block diagram of the GCC algorithm. The two added narrowband filters improve the sharp maximum peak achieved by the cross correlation. The filters play a major role in improving the time delay accuracy and SNR (Khaddour, 2011:33). After the process of filtering, the signal from filter H2 is delayed, and cross correlated with the signal from filter H1. The resultant signals from the multiplier are integrated for various delays, until the maximum peak is attained.

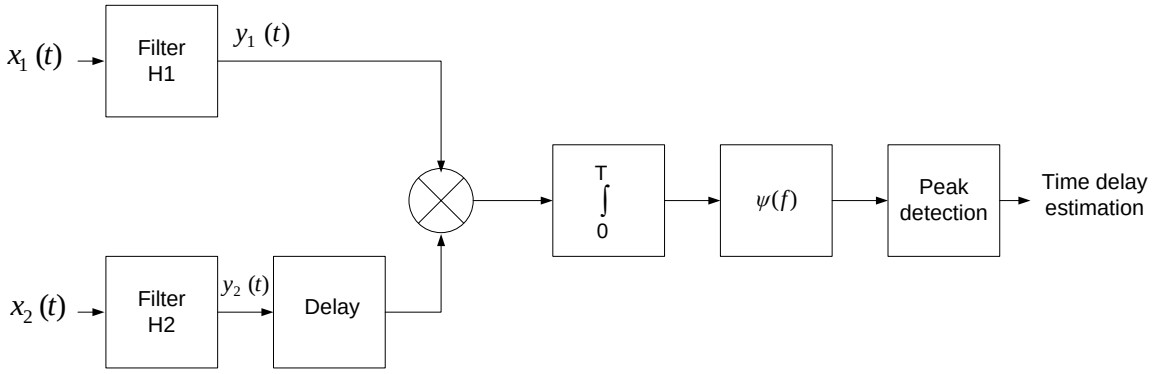

Figure 3-7: The block diagram of a GCC algorithm (Adapted from Khaddour, 2011:33)

According to Hasan (2011:33), the cross correlation between $x_1(t)$ and $x_2(t)$ is defined as the cross power spectral density, using Equation 3.6.

$$S_{x1x2} = E\left\{X_1(f)\, X_2^*(f)\right\} \qquad 3.6$$

Here E denotes the expected value, * denotes the complex conjugate, while $X_1(f)$ and $X_2(f)$ are the Fourier transform of $x_1(t)$ and $x_2(t)$ respectively.

The selection of the prefilter function is a crucial matter that affects the time delay estimation of the GCC algorithm. Khaddour,(2011:33) selected the prefilter function equal to one for the classical cross correlation method, however, other methods are also used to select the prefilter function, e.g. the Roth processor, the phase transform (PHAT) and maximum likelihood (ML). The function of the prefilter function is to maximise the sharp and large peak obtained by the cross correlation method. The GCC is very simple to implement, but the accuracy decreases with low SNR.

3.3.3 Zero crossing (ZC)

Zero crossing (ZC) is an alternative algorithm that can estimate the phase difference between two signals of the same frequency, independent of the amplitudes of the signals, and is derived from the time difference between the zero crossings of the two signals (Mazeika & Draudviliene, 2010:7). The advantage of the ZC algorithm is that in principle it needs only one cycle to obtain an estimate of the phase differences, and that is easy to implement. According to Changlin (2006), the time between the ZC points of the two signals of the same frequency is assumed to be N_x, and the phase difference between the two signals is assumed to be φ. Their relationship is defined by Equation 3.7. N is the period of the signal.

$$\varphi = \frac{N_x}{N} \times 360^{\circ}. \qquad 3.7$$

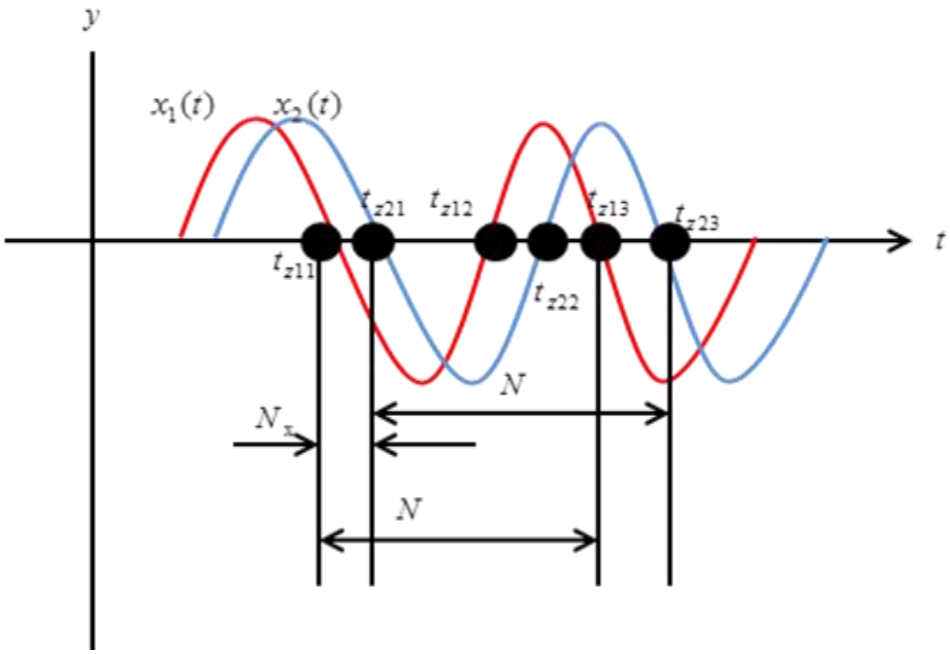

Figure 3-8: Two signals with the same frequency and a phase shift of φ between them. The ZC points are shown in the Figure with black dots (Adapted from Changlin, 2006: 395)

Changlin (2006) states that, for the ZC algorithm, the major factor is how to determine the period of the signal accurately. The time difference between the ZC points and the period of the signal are defined by Equation 3.8.

$$N_x = \frac{(t_{z21} - t_{z11}) + (t_{z22} - t_{z12}) + (t_{z23} - t_{z13})}{3}. \qquad 3.8$$
$$N = \frac{(t_{z13} - t_{z11}) + (t_{z23} - t_{z21})}{2}$$

Zhou *et al*., (2012) proposed a ZC algorithm of comparable accuracy with the FFT and high SNR, but with a low computational complexity processing latency, which was suitable for real-time applications. Zhou *et al*. (2012) observes that the accuracy of determining the time delay, using the zero crossing algorithm, depends on three factors, namely SNR, frequency of the signal and the number of the ZC points. The low computational complexity of Zhou *et al*., (2012:65), was based on the time detection of the zero crossings of the signal, i.e. when the signal level corresponds to zero.

The proposed low computational complexity algorithm is based on a single tone signal defined by Equation 3.9.

$$s(t) = A \sin\left(\omega\left(t - \tau_0\right)\right) + n(t) \qquad 3.9$$

Here A is the amplitude of the signal, ω is the angular frequency, τ_0 is the time delay and $n(t)$ represents the noise added to the received signal.

The ZC points were detected using linear interpolation method, with a threshold value of alpha, to avoid the incorrect zero crossing points that result from noise. This is illustrated by Figure 3-9. The sampling points $[t_+(n), s_+(n)]$ and $[t_-(n), s_-(n)]$ were defined by Equations 3.10

$$\begin{aligned} &s_+(n) \geq \alpha \;\&\; s_+(n-1) < \alpha, \\ &s_-(n) \geq -\alpha \;\&\; s_-(n+1) > -\alpha. \end{aligned} \qquad 3.10$$

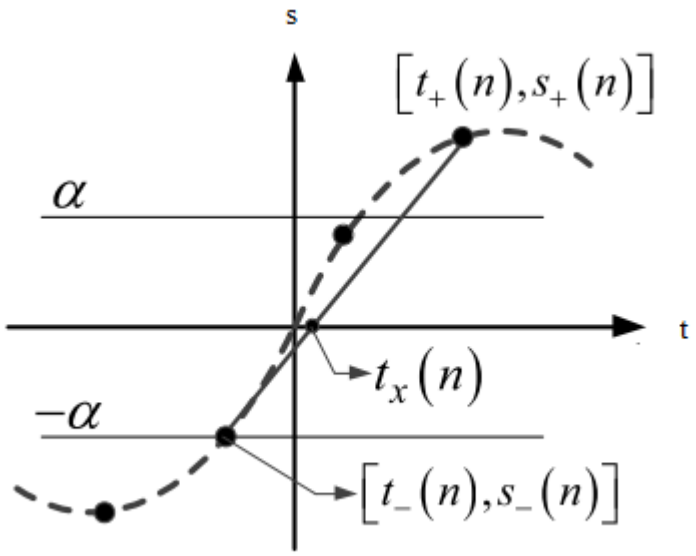

Figure 3-9: Detection of the zero crossing points using linear interpolation (Adapted from Zhou *et al*., 2012:66)

Figure 3-9 shows that $t_x(n)$ represents the real ZC point. This process was repeated for all points in the signals, where the signal changes sign from negative to positive or vice versa.

Additive noise was implemented using white Gaussian noise. The results conclude that the proposed ZC algorithm by Zhou *et al*., (2012:65) achieves the same accuracy as the FFT algorithm at high SNR levels. The computational complexity of the proposed ZC algorithm is lower than that of the FFT.

Zhou *et al*., (2012:65) states that the GCC and the FFT algorithms are considered to be the most accurate time delay estimation methods, however, their computational complexity is excessive compared to that of the ZC method. Enhancement in computational speed may require more complex hardware such as parallel processors. The complexities of higher speed depend on the number of samples, number of antennas and number of operations. The need for parallel processors or neural network algorithms or both increases the complexities of the algorithms.

3.3.4 Fast Fourier Transform (FFT)

Fourier transform is a tool that is used to convert a signal in the time domain to the frequency domain (spectrum). This is useful since some measurements are very hard to obtain in the time domain, while they are considered to be very easy to obtain in the frequency domain. FFT is used to detect the phase difference between two signals acquired simultaneously. The phase difference between two signals can be computed from the real and imaginary part of the Fourier transformed signals. The FFT is applied to a finite length snapshot of the output signals of each element in the array, to measure the phases at the peak points of the

amplitude spectrum (Xiong *et al*., 2006:1) at the operating frequency, and then to calculate the phase differences to obtain the DOA. The FFT is applied to the baseband representation of the outputs of the elements in the array, and then estimates the phase difference.

Xiong *et al*. (2006:1) took the FFT of each output signal of the elements in the array to detect the peak values of the amplitude spectrum at the frequency of operation. The source of the signal was taken to be in the far field. The phases of the peak values were measured, to calculate the phase differences and un-wrap them to get the phase delays. The DOA was estimated from the phase delay of the signals. The result proves that the phase difference technique requires less calculation and less elements. In addition, the resolution of the DOA estimation is very high. The results were evaluated with different SNR levels for 200 times, and the estimation was quite accurate (Xiong *et al*., 2006:4). Xiong observes that detecting the peak phase by means of the FFT reduces the amount of noise, which results and increased phase resolution. The inherent advantage of the FFT method is that it bases the phase estimation on all the samples of the snapshot. The disadvantage is that it requires a snapshot of fairly long duration, during which time the azimuth and elevation could changed.

3.3.5 Modified Cross Power-Spectrum Phase Method (ρ-Cross Power-Spectrum Phase)

The cross power-spectrum phase (CPSP) algorithm has a significant advantage in that its time delay estimation outperforms the normalised cross correlation and least mean square (LMS) adaptive filters, according to Omologo & Svaizer (1994: II-273). The CPSP algorithm is considered the most efficient time delay estimation in an environment when the SNR is high (Omologo & Svaizer, 1994: II-274).

However, Shen & Liu (2009:1286) proposed a modified CPSP method which is called ρ-Cross Power-Spectrum Phase (ρ-CPSP) with a coherence function. The main focus is on achieving accurate results in noisy environments. The modified CPSP method calculates the coherence of the two signals, using a novel coherence function.

The crucial factor in the CPSP method is the CPSD, which describes the random signals in the frequency domain. When the CPSD is estimated correctly, accurate results of time delay are obtained.

The accuracy is expressed in terms of the difference between the true time delay and the estimated time delay. This difference can be expressed in terms of RMSE versus SNR. The covariance matrix was used to estimate the variation of the SNR (Shen & Liu, 2009:1287). The covariance matrix can be used to compute the CPSD. Shen & Liu (2009: 1287) observe that the coherence function and the covariance matrix based on the CPSP method, improves

the accuracy in time delay estimation and reduces the errors in DOA estimation in a noisy environment.

3.4 High resolution DOA estimation algorithms

There are some high resolution DOA estimation algorithms that simultaneously estimate the DOA of multiple signals. These have not been included in this study. The high resolution algorithms have the disadvantage of instability and require complex calculations. Jha & Durrani (1991) proposed a neural – network method in the DOA estimation. The signal mainly shows unstable characteristics (limited duration and time variable) after considering that vocal and radar except a few special cases. Therefore, researchers started to apply a neural – network method in DOA estimation. The method has not been applied in practice, but has been performed in lab simulations. Some of the high resolution DOA algorithm such as MUSIC has a better resolution, moderate calculation, better stability and commonly used in different array structures after taking the neural – network into consideration. The MUSIC and ESPRIT algorithms are briefly described in following paragraphs:

MUSIC and ESPRIT are high resolution algorithms which give superior results when it comes to DOA estimation. However, their complexity and accuracy comes at a high cost when implementing such algorithms. Thus they were not considered in the present study which focuses on the estimation of DOA of signals from a single source.

Liu & Mendel (1998) proposed an ESPRIT-based algorithm to simultaneously estimate the azimuth and elevation angles of various independent sources. They tested the proposed algorithm on several array configurations, such as a uniform linear arrays and rectangular arrays. Simulation results proved that the proposed algorithm works well for different array configurations. However, the proposed algorithm fails for elevation angles near 90°. A parametric model was presented to describe the phenomenon and justify it with simulations which address the errors near 90°.

Liang (2009) proposed joint azimuth and elevation direction-finding, using cumulant for two-dimensional DOA. He was addressing some drawbacks of the Liu & Mendel (1998) algorithm. Liang (2009:6) used a particular volume array, and the objective was to estimate both the azimuth and elevation angles of several signals from multiple directions impinging on the array at the same time. The results validate the performance of his method. As the SNR increases, the RMSE decreases. In addition, the errors in estimating the DOA decrease when the distance between the elements increases and when the snapshots of the signal increase. He used special estimation operations to prevent estimation failure at elevation angles near 90°.

El-Barbary *et al*. (2013:132) proposed a modified MUSIC algorithm which works much better than the ordinary MUSIC algorithm. The results were evaluated at different SNR levels in terms of the SD of the estimated errors.

Quighua *et al*. (2013:2037) proposed a new jointly sparse decomposition method based on the Khatri-Rao (KR) product to estimate the two-dimensional DOA with an L-shaped array. The simulation results of this method demonstrated that it is efficient and gives a smaller SD of estimated errors than the existing KR-MUSIC and KR-CAPON (Ma *et al*., 2010).

3.5 Factors affecting algorithms for the estimation of DOA

The performance of DOA algorithms can be affected by various factors. The factors include SNR, number of signals samples per second, total number of samples (or snapshots) used for each DOA estimate, number of elements in the array and the distance between the elements (Sanudin *et al*., 2011:1).

Studies by Liang (2009), Shrestha *et al*. (2012) and Sanudin *et al*. (2011:1) concluded that the errors in estimating the DOA decrease when the SNR, number of snapshots and the distance between the elements increases. Adding more elements to the array also improves the accuracy of DOA estimation.

3.6 Sources of Error in DF systems

Although the focus of the research is not concerned with the hardware of the HD DF array, it is necessary to outline some general sources of error in DF systems.

Gething (1991:95) identified four categories of error in DF systems:

a) *Instrumental errors:* The DF equipment itself introduces the instrument errors. Instrument errors on DF systems depend on the condition and adjustment of the equipment. Several calibrations and adjustments have to be performed regularly with instructions from the DF equipment technical manuals.

b) *Site errors:* Site error develops at the DF site. Site errors result from one or several sources. The orientation and spacing of the DF system's antennas plays a major role in achieving maximum DF accuracy. It is crucial for the antennas to orient to a known reference point when a new DF site is set up. Accurate results are achieved by orientating the antennas to a known reference point and accurately measuring the spacing of the phase centres of the antennas.

c) *Wave interference errors*: Wave interference error occurs when two or more independent rays arrive at the DF equipment simultaneously, making the resolution of the DOA estimate difficult.

d) *Propagation errors:* Propagation errors result from fluctuation of radio waves between the transmitting antenna and the DF equipment. The fluctuation is due to radio waves being absorbed, reflected, refracted and scintillated by the ionosphere.

In terms of the practical implementation of the hardware of the HF DF array, certain factors have to be taken into consideration such as clock jitter, latencies in transmission lines, bit resolution required to meet error specification when quantised in terms of analog-to-digital conversion. Jitter is defined as the deviation of timing of a set of periodic pulses from their true values (Yamaguchi *et al*., 2001). The frequency of successive pulses, the signal amplitude and the phase of the periodic signal causes jitter to be observed. Jitters in clock signals are mostly caused by noise or other disturbances in the system. Factors that contribute to clock jitter include thermal noise, device noise, power supply variations and interference coupled from nearby circuits (Yamaguchi *et al*., 2001).

Clock jitter contributes a noise source in terms of variations in the sampled voltage for each channel which is accommodated in simulations of the algorithms by the addition of independent Gaussian noise to the ideal received signal from each channel.

The lengths of the transmission lines from the antennas to the receiver were assumed to have the same length. The differences in line lengths could lead to variations in the latencies from different antennas. This would be minimised during a calibration procedure or accommodated through a known delay which can be measured during setup and implemented as an additional time delay in the software for processing the signals. The actual derivations of these latencies from measurements on the hardware are beyond the scope of the thesis.

A 12-bit analog-to-digital sound card was used for the conversion in the hardware system. This limits the bit error to $\left(\frac{1}{2}\right)^{12}$ of the range of the signal, and thus contributes a potential noise component of 0.02% which is accommodated in the simulations of the algorithms through addition of Gaussian noise to the ideal received signals. The ADC will be run from the same clock to minimise timing differences, regarding the synchronisation of the ADC clock.

3.7 Summary

Various signal processing algorithms for the estimation of the time delay or phase differences of the signals from the elements of the HF DF receiver array were discussed. Several algorithms for the estimation of the DOA were reviewed. Possible sources of error due to the DF system were summarised. This knowledge will be used to compare the performance of various signal processing algorithms for estimating the phase difference between two signals. This is described in chapter five. The next chapter describes the method that was used to estimate the azimuth (α) and elevation (ε) angles of the DOA from the phase differences between the signals from the elements of the HF DF array.

CHAPTER FOUR: METHODOLOGY

4.1 Introduction

The DOA of an HF radio beacon signal transmitted from ZACUBE-1 (TshepisoSAT) at 14.099 MHz is expressed in terms of the two angles, azimuth (α) and elevation (ε). The DOA of the received HF signal is estimated from the phase differences between signals received by an L-shaped antenna array. It is planned that the L-shaped array will eventually consist of seven DF crossed loop dipole antennas (interferometer array). However, the initial project is based on the three elements, as depicted in Figure 1-4.

The phase differences between the signals are directly proportional to the time delay between the arrival of the signal at the reference antenna and at the other antennas. This chapter describes the method that was followed to estimate the phase differences and to derive the DOA from the phase differences, using simulated baseband signals. It also explains how the RF signals are converted to baseband signals in the hardware. The effect of Doppler shift is demonstrated. The factors that affect the accuracy of the estimation of the DOA are described. Methods that evaluate the distribution of the SD of the azimuth and elevation errors are presented.

4.2 Conversion of the RF signals to baseband signals

The RF signals received at the DF elements are converted to baseband signals by means of a series of elements, as illustrated in Figure 4-1. Figure 4-1 uses two elements as an example. The two elements shown in Figure 4-1 are the Reference antenna (at the corner of the L-array) and any one of the other antennas. The band of interest around 14.099 MHz is a down-conversion to the baseband signal (0 – 20 kHz), using a single mixing stage. The mixing process retains all the information of the signal and all signals in the pass band will be translated. However, the local oscillator (LO) that feeds the mixers does not operate at exactly same frequency as the HF signal transmitted from the CubeSat, but at 14.098 MHz. This will result in a 1 kHz baseband signal, which is the difference between the transmitted carrier of 14.099 MHz and 14.098 MHz (Coetzee, 2012).

The signals from the mixers, $z_1(t)$ and $z_2(t)$, are defined by Equations 4.1 and 4.2 respectively.

$$z_1(t) = x_1(t) \times y(t) = A_1 \cos\ (2\pi f_c\ t)\ \cos(2\pi f_o\ t)$$
$$= \frac{A_1}{2}\ \cos\ [2\ \pi(f_c + f_o)\ t] + \frac{A_1}{2}\cos\ [2\ \pi(f_c - f_o)\ t]\ , \qquad 4.1$$

$$z_2(t) = x_2(t) \times y(t) = A_2 \cos\left[2\pi f_c\left(t - \frac{d\cos\theta}{c}\right)\right]\cos(2\pi f_o t)$$
$$= \frac{A_2}{2}\cos\left[2\pi(f_c + f_o)\left(t - \frac{d\cos\theta}{c}\right)\right] + \frac{A_2}{2}\cos\left[2\pi(f_c - f_o)\left(t - \frac{d\cos\theta}{c}\right)\right], \quad 4.2$$

where f_o is the LO frequency of 14.098 MHz, f_c is the carrier frequency of 14.099 MHz, $f_c + f_o$ is the sum frequency at 28.197 MHz, $f_c - f_o$ is the difference frequency at 1 kHz, A_1 and A_2 are the amplitudes of the two received signals, (the amplitudes of the two signals are assumed to be unity without loss of generality), d is the distance between two antennas in metres, θ is the elevation angle as defined in Figure 1-8 measured in radians or degrees and c represents the speed of light in m/s.

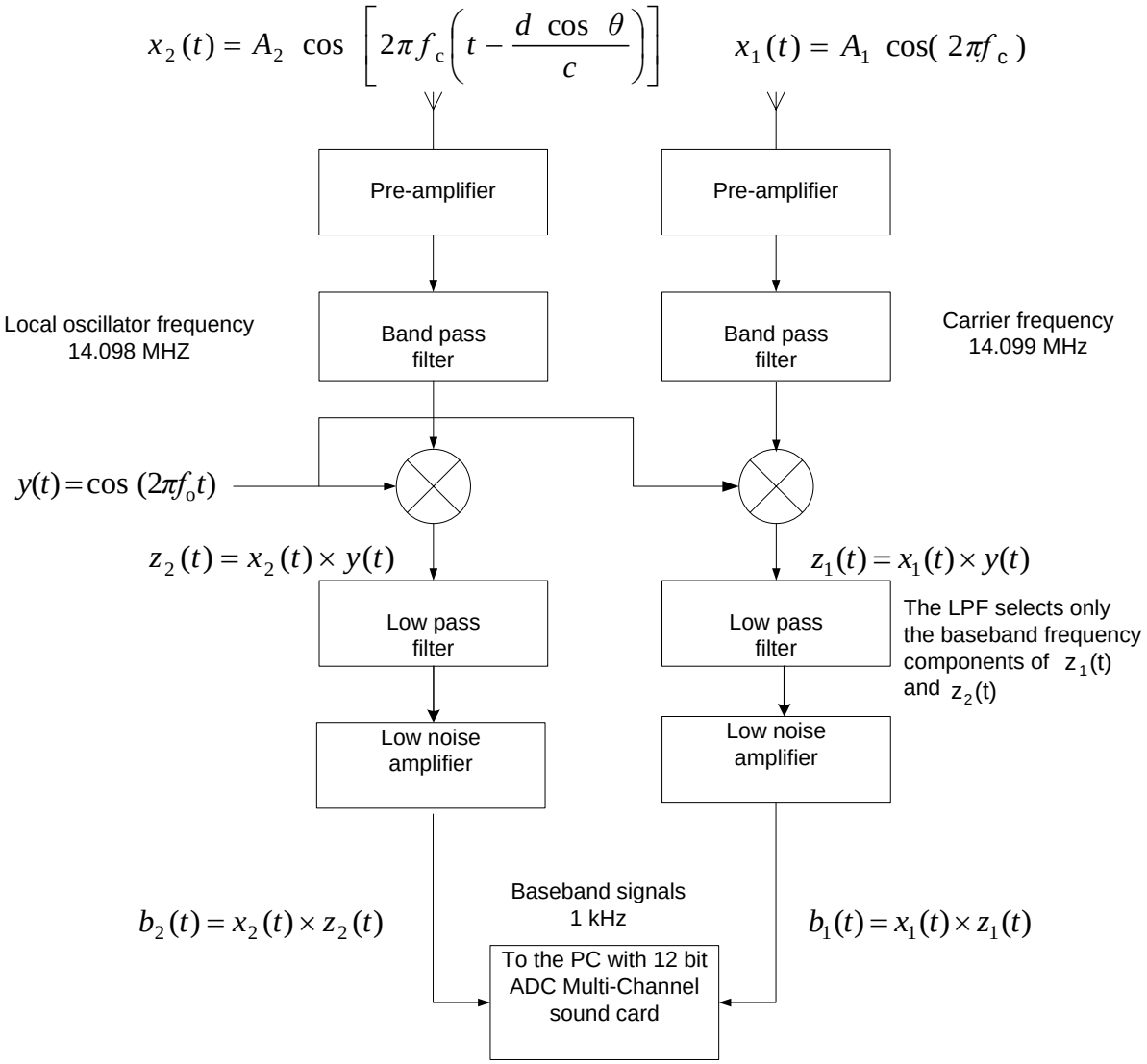

Figure 4-1: Block diagram of the elements used in the conversion of the RF signals to baseband signals

The time series representation of the two signals, $z_1(t)$ and $z_2(t)$, after the mixer are shown in Figures 4-2 and 4-3 respectively. The 1 kHz signal is multiplied by the 28.197 MHz signal.

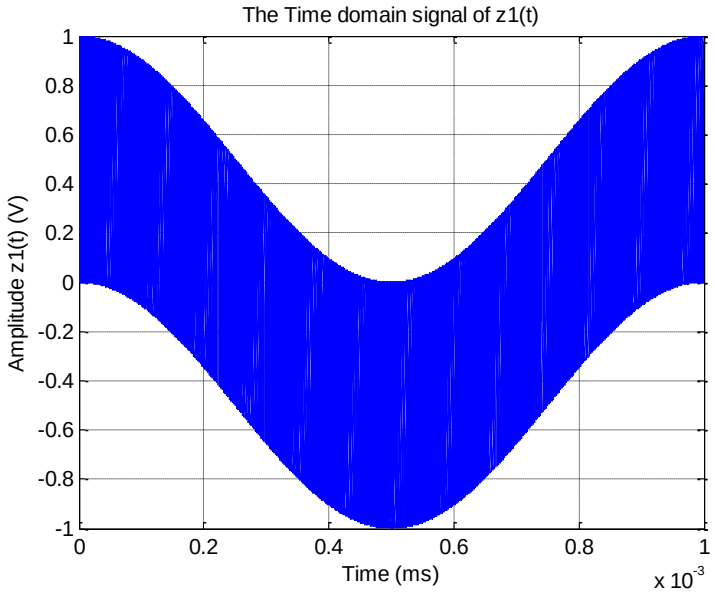

Figure 4-2: The time series representation of $z_1(t)$ over a period of 1 ms sampled at 300 ks/s (kilo sample per second)

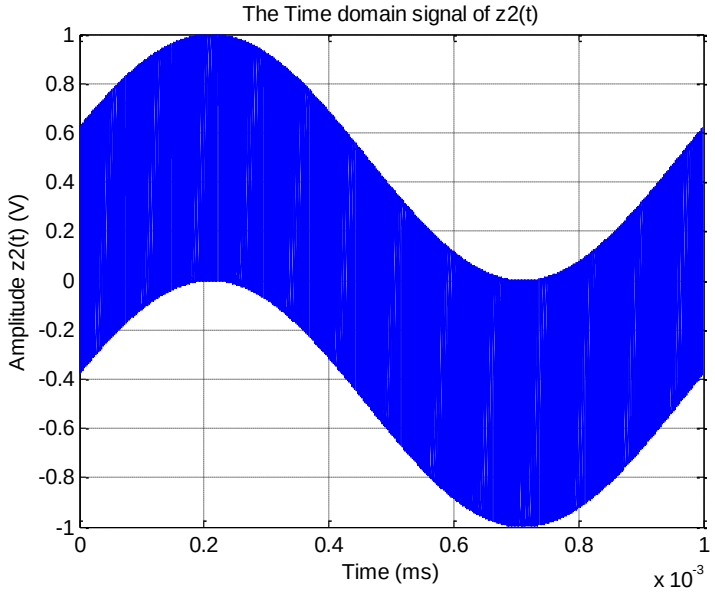

Figure 4-3: The time series representation of $z_2(t)$ over a period of 1 ms sampled at 300 ks/s shifted with a time delay of $\frac{d\cos\theta}{c}$ for the following values of d and θ: d = 10 m, θ = 90˚

It was impractical to graphically depict all the results of the RF signal manipulation, because of the limited memory of the computer. Theoretical calculations were done first on simulated signals, so as to form an idea of what to expect from the hardware implementation of the simulated system. Equations 4.1 and 4.2 illustrate that plotting $z_1(t)$ and $z_2(t)$ in the frequency domain results in Dirac delta functions sitting at $\pm$ 28.197 MHz and $\pm$1 kHz on

one graph. However, it is difficult to see both spectra on a common frequency scale. Figure 4-4 clearly shows the ± 28.197 MHz spectra and spectra near 0 MHz. Figure 4-5 shows the ± 0.001 MHz spectra, while Figure 4-6 shows the zoomed version of the spectra near 0 MHz which have components that are displaced by ±1 kHz from 0 MHz. (The unit ks/s represents kilo sample per second).

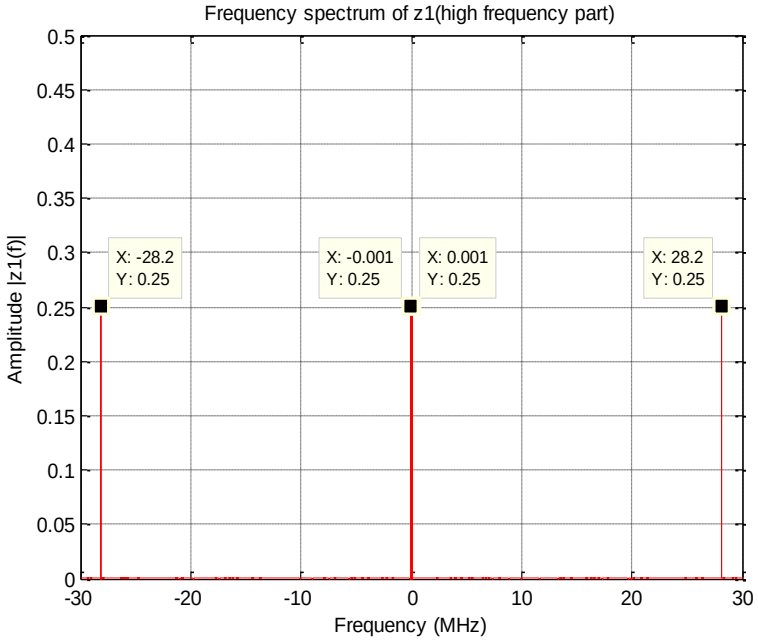

Figure 4-4: The double-sided Fourier spectrum of z1 (f) has components at the sum frequencies – 28.197 MHz and +28.197 MHz and near 0 MHz

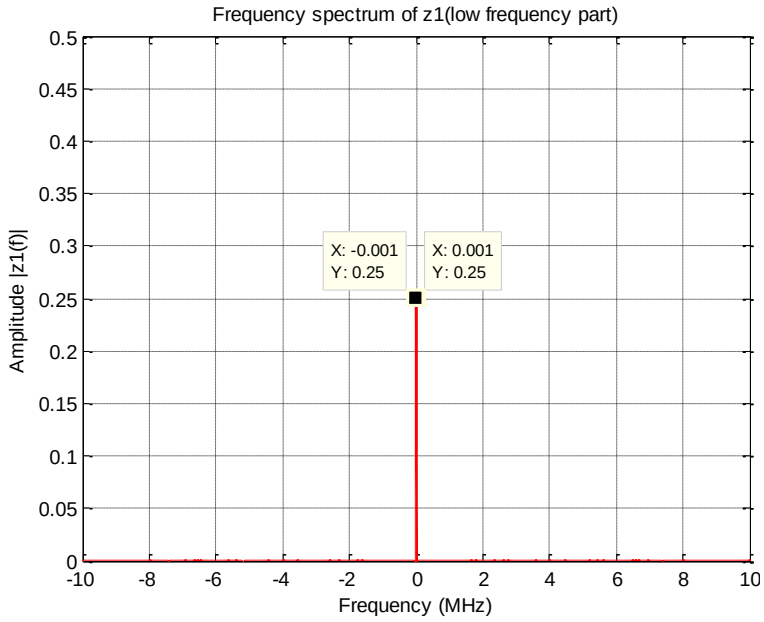

Figure 4-5: The double-sided Fourier spectrum of the low frequency part of z1 (f) shows spectral lines at –1 kHz and +1 kHz

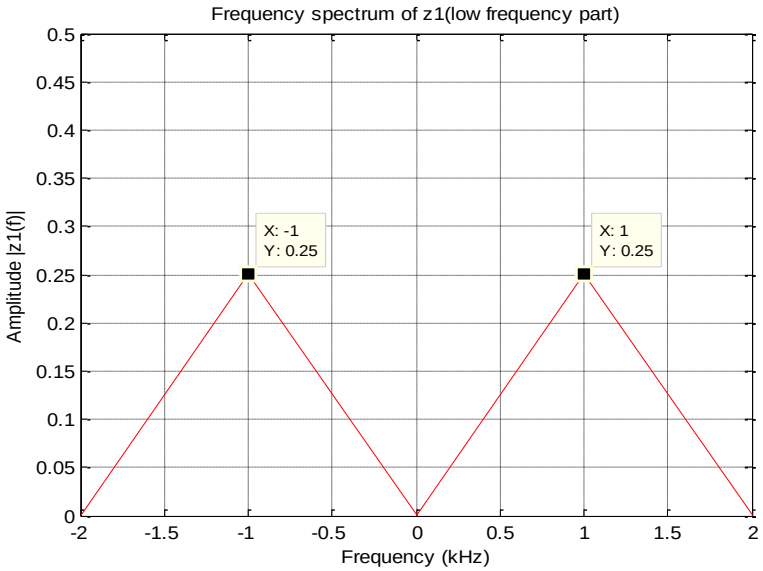

Figure 4-6: The zoomed version of the low frequency part of the spectrum z1 (f) shows spectral lines at –1 kHz and +1 kHz

The sum frequency components are removed by low pass filtering, leaving only the baseband signals. The baseband signals, $b_1(t)$ and $b_2(t)$, that have to be processed are represented by Equation 4.3 and 4.4. The same procedure is adopted for the conversion of the RF signals to baseband signals, using the three elements that resolve both azimuth and elevation angles.

$$b_1(t) = \frac{A_1}{2}\cos[2\pi(f_c - f_o)t] + n_1(t), \qquad 4.3$$

$$b_2(t) = \frac{A_2}{2}\cos\left[2\pi(f_c - f_o)\left(t - \frac{d\cos\theta}{c}\right)\right] + n_2(t). \qquad 4.4$$

4.3 Analysis of Doppler shift

Doppler shift is defined as the apparent frequency shift that takes place when the source and receiver are moving with different speeds while transmitting or receiving a signal (McNamara 1991:35). The Doppler shift causes the received frequencies of a source to differ from the transmitted frequency. The analysis of Doppler shift aims to check the sensitivity of the various algorithms for the changes in the received HF beacon carrier frequency.

Due to the Doppler shift, the frequency transmitted from the satellite changes before it reaches the receiver. Doppler shift is crucial in the context of HF beacon signal transmission. The receiving system for the HF DF array should have sufficient bandwidth to cover the range of frequencies from the carrier frequency (14.099 MHz) plus or minus the Doppler shift frequency. The Doppler shift on the carrier frequency is passed on to the baseband

frequency. The Doppler shift was calculated, using Equations 4.5 and 4.6, adopted from Liu (1999: 317).

The transmitted carrier frequency from the satellite is $f_o = 14.099\ \text{MHz}$. The observed frequency at the receiver is defined by Equation 4.5

$$\begin{aligned} f_{\text{observed}} &= f_o + f_d, \\ &= \left(1 + \frac{V_{\text{ray}}}{c}\right) f_o. \end{aligned} \qquad 4.5$$

Here f_o denotes the transmitted carrier frequency from the satellite in MHz, f_d represents the Doppler shift in Hz, V_{ray} is the radial velocity of the satellite relative to the receiver in m/s , the component that causes Doppler shift, c , denotes the speed of light in m/s. The maximum Doppler shift is related to the transmitted carrier frequency and the radial velocity by Equation 4.6.

$$\Delta f = \frac{V_{\text{ray}}}{c} f_o. \qquad 4.6$$

The Doppler shift is caused by the satellite movement relative to the earth. Two cases were considered for the Doppler shift analysis. In the first case, a special case was considered, when the satellite is on the horizon and moving away from the receiver, as shown in Figure 4-7.

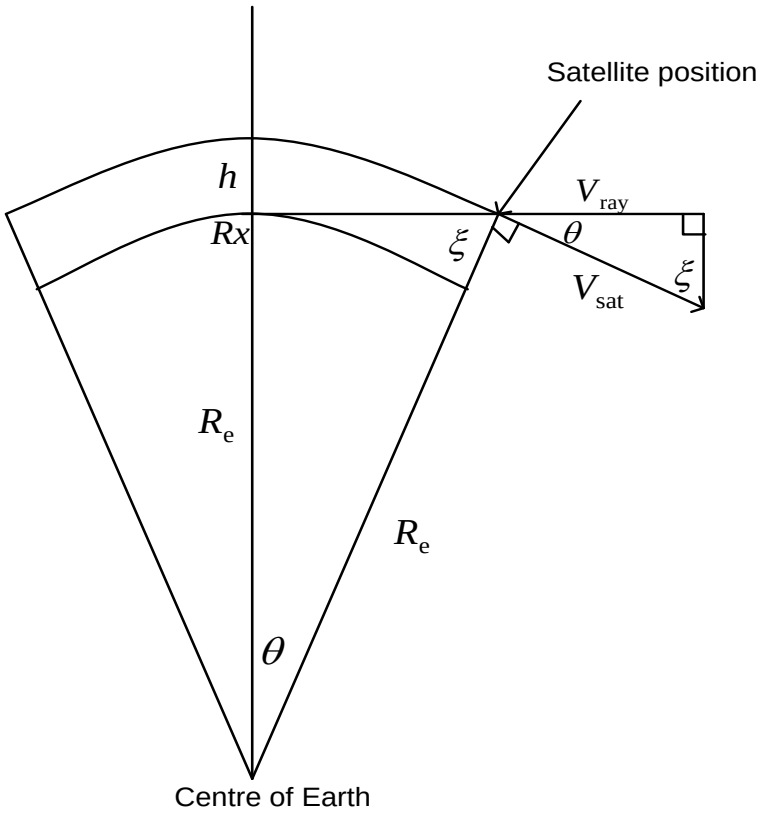

Figure 4-7: Illustration of the geometry of Doppler shift analysis for the special case when the satellite is on the horizon and moving away from the receiver Rx The satellite is travelling at a tangential velocity (V_{sat}) and at an altitude of h km

The radial velocity of the satellite relative to the receiver is defined as the product of the satellite velocity and the cosine of angle θ. Tsui (2000) defines the radial velocity as

$$\begin{aligned} V_{ray} &= V_{sat} \times \cos\theta, \\ \theta &= 90^{\circ} - \xi, \\ V_{ray} &= V_{sat} \times \cos(90^{\circ} - \xi), \\ V_{ray} &= V_{sat} \times \sin(\xi). \end{aligned} \qquad 4.7$$

In Figure 4-7 R_e represents the mean Earth radius (6371 km) and h represents the satellite altitude (642.1 km). The satellite altitude varies, since the satellite is in an elliptical orbit. The satellite altitude used for the calculation was the average value of the perigee of 597.5 km and apogee of 686.7 km. The angle ξ was calculated as follows:

$$\begin{aligned} \sin(\xi) &= \frac{R_e}{R_e + h} = \frac{6371}{6371 + 642.1} \\ \xi &= \sin^{-1}\left(\frac{6371}{6371 + 642.1}\right) \\ &= 65.29^{\circ}. \end{aligned} \qquad 4.8$$

The orbital velocity at both perigee and apogee were calculated as follows:

Velocity at perigee:

$$v_{\mathrm{p}} = \sqrt{\frac{2\mu r_{\mathrm{a}}}{r_{\mathrm{p}}(r_{\mathrm{a}} + r_{\mathrm{p}})}}$$
$$= \sqrt{\frac{2 \times 3.986005 \times 10^5 \times 7057.7}{6968.5(7057.7 + 6968.5)}}$$
$$= 7.587\,\mathrm{km/s},$$

Velocity at apogee:

$$v_{\mathrm{a}} = \sqrt{\frac{2\mu r_{\mathrm{p}}}{r_{\mathrm{a}}(r_{\mathrm{a}} + r_{\mathrm{p}})}}$$
$$= \sqrt{\frac{2 \times 3.986005 \times 10^5 \times 7057.7}{7057.7(7057.7 + 6968.5)}}$$
$$= 7.491\,\mathrm{km/s}.$$

4.9

$$r_{\mathrm{a}} = R_{\mathrm{e}} + h_{\mathrm{a}} = 6371 + 686.7 = 7057.7\ \mathrm{km}$$
$$r_{\mathrm{p}} = R_{\mathrm{e}} + h_{\mathrm{p}} = 6371 + 597.5 = 6968.5\ \mathrm{km}$$

Here μ = Earth gravitational parameter ($3.986005 \times 10^5\,\mathrm{km^3 s^{-2}}$), R_{e} is the mean Earth radius (6371 km), h_{a} is the apogee altitude (686.7 km) and h_{p} is the perigee altitude (597.5 km). The orbital velocity at the perigee and apogee differ by less than 1.2 %. The average orbital velocity which is within 1.2 % of the velocity at either perigee or apogee was used for the remaining discussion of the Doppler effect since the Doppler shift itself is much larger than the effect of perigee and apogee.

The velocity of the satellite was calculated from the angular velocity as a function of the elevation angle, time and the orbital period. The orbital period for the CubeSat was calculated by using Equation 4.10 using the semi-major axis and the Earth gravitational parameter.

$$a = R_{\mathrm{e}} + h = 6371 + 642.1 = 7013.1\,\mathrm{km}$$

$$P = \frac{2\pi}{\sqrt{\mu}} a^{3/2}$$
$$= \frac{2\pi}{\sqrt{3.986005 \times 10^5}} \times (7013.1)^{3/2}$$
$$= 5844.887\mathrm{s}$$
$$= 97.41\ \mathrm{min}.$$

4.10

Here μ = Earth gravitational parameter ($3.986005 \times 10^5\,\mathrm{km^3 s^{-2}}$), R_{e} is the mean Earth radius (6371 km), h is the average altitude and a is the semi-major axis.

After calculating the orbital period, the angular velocity was calculated with Equation 4.11,

$$\begin{aligned}\dot{\theta} &= \frac{d\theta}{dt} = \frac{2\pi}{P}, \\ &= \frac{2\pi}{(97.41)\times 60} \\ &= 1.057\times 10^{-3}\ \text{rad/s}.\end{aligned} \tag{4.11}$$

Knowing the angular velocity using the average value, the velocity of the satellite was calculated as

$$\begin{aligned}V_{\text{sat}} &= (R_{\text{e}} + h)\times \frac{d\theta}{dt}, \\ &= (6371 + 642.1)\times 1.057\times 10^{-3} \\ &= 7412.84\ \text{m/s}.\end{aligned} \tag{4.12}$$

Using the satellite velocity, the velocity component that causes Doppler shift (radial velocity) was calculated as

$$\begin{aligned}V_{\text{ray}} &= V_{\text{sat}}\times \sin(\xi), \\ &= 7412.84\times \sin(65.29^{\circ}) \\ &= 6734\ \text{m/s}.\end{aligned} \tag{4.13}$$

The Doppler frequency was calculated from the velocity of the satellite along the ray path, the transmitted carrier frequency and speed of light, as

$$\begin{aligned}f_{\text{d}} &= V_{\text{ray}}\times \frac{f_{\text{c}}}{c} \\ &= 6734\times \frac{14.099\times 10^{6}}{3\times 10^{8}} \\ &= 316.47\ \text{Hz}.\end{aligned} \tag{4.14}$$

All the calculations above were done for the special case when the satellite is on the horizon. The special case was generalised for all elevation angles and using the altitude as an average value. Figure 4-8 depicts the geometry for the general case.

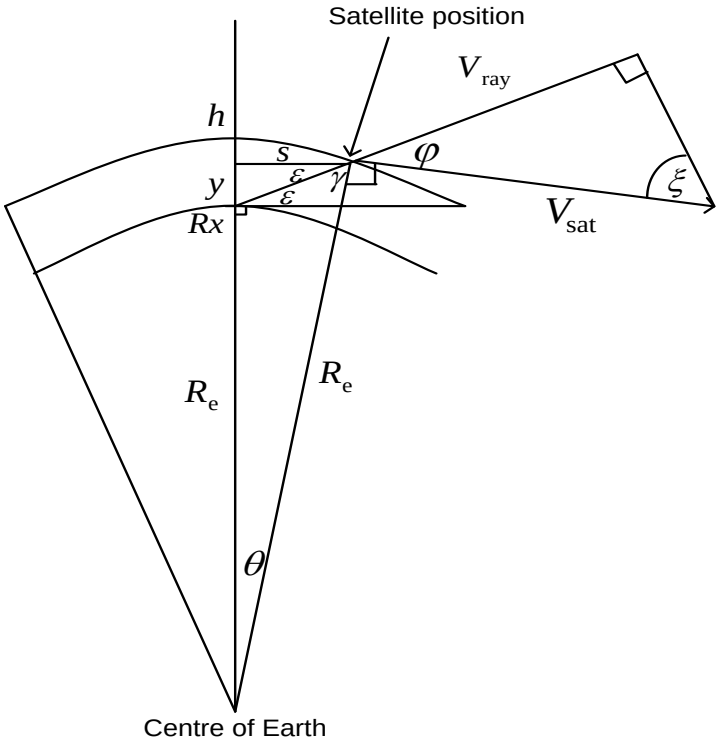

Figure 4-8: The geometry of the Doppler shift analysis for the general case

The Doppler frequency for the general case was obtained as follows. The angles and distances from Figure 4-8 were derived, using Equation 4.15,

$$\begin{aligned}
&\cos\theta = \frac{R_e + y}{R_e + h} \\
&R_e + y = (R_e + h)\cos\theta, \\
&s = (R_e + h)\sin\theta, \\
&\varepsilon = \tan^{-1}\left(\frac{y}{s}\right).
\end{aligned} \qquad 4.15$$

Here y is the height above the horizon in km, s is the horizontal distance to the satellite in km, θ denotes the central angle of the Earth in degrees, h is the satellite altitude and R_e is the Earth radius.

The angle between the velocity of the satellite along the ray path and the speed of the satellite was defined from Figure 4-8 as,

$$\begin{aligned}
&\theta + 90^\circ + \varepsilon + \gamma = 90^\circ + \varphi + \gamma, \\
&90^\circ + \varphi = \theta + 90^\circ + \varepsilon.
\end{aligned} \qquad 4.16$$

Having calculated the angle between the velocity of the satellite along the ray path and the speed of the satellite, the radial velocity could be calculated as

$$V_{ray} = V_{sat}\sin(\xi) = V_{sat}\cos(\varphi). \quad 4.17$$

After obtaining the radial velocity component, the Doppler frequency was calculated with Equation 4.14. Since θ, the angle of the satellite at the centre to the Earth varies, the radial velocity of the satellite, the Doppler frequency and the Doppler shifted baseband frequency vary as θ varies. Figures 4-9 to 4-11 demonstrate the variation of the velocity of the radial component of the satellite velocity along the visible part of the satellite trajectory, the Doppler frequency and the Doppler-shifted baseband frequency respectively, plotted as a function of θ.

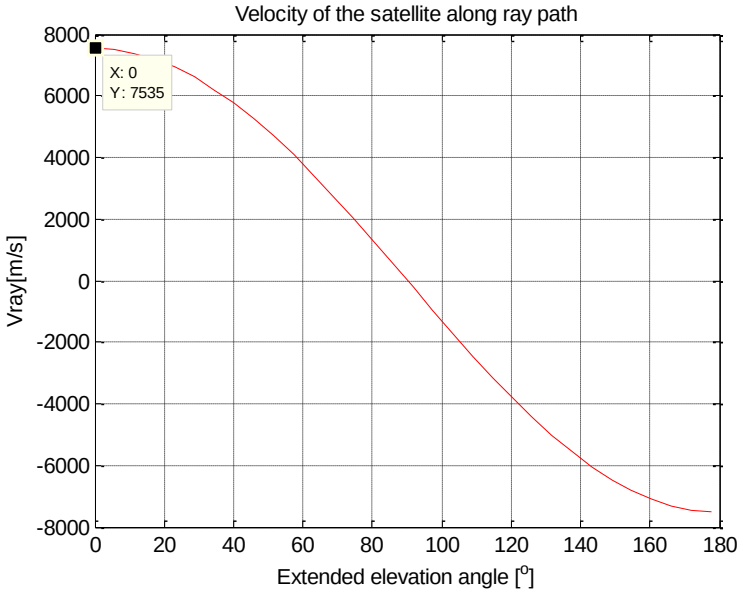

Figure 4-9: The velocity of the satellite along the ray path during polar orbit overpass over the receiver. The radial component of the velocity of the satellite is at maximum when the satellite is on the horizon and starts decreasing as the satellite moves towards the receiver. When the satellite is directly overhead, the radial component of the velocity of the satellite is 0, and continues decreasing as the satellite moves away from the receiver. The extended elevation angle on the x-axis illustrates that when the satellite is moving away, the values of the elevation angles go above 90˚. This is contrary to the normal definition of the elevation angle which does not support values above 90˚

The Doppler shift on the carrier frequency was plotted as a function of the extended elevation angle and it was calculated to be a maximum of 354.1 Hz, as shown the Figure 4-9.

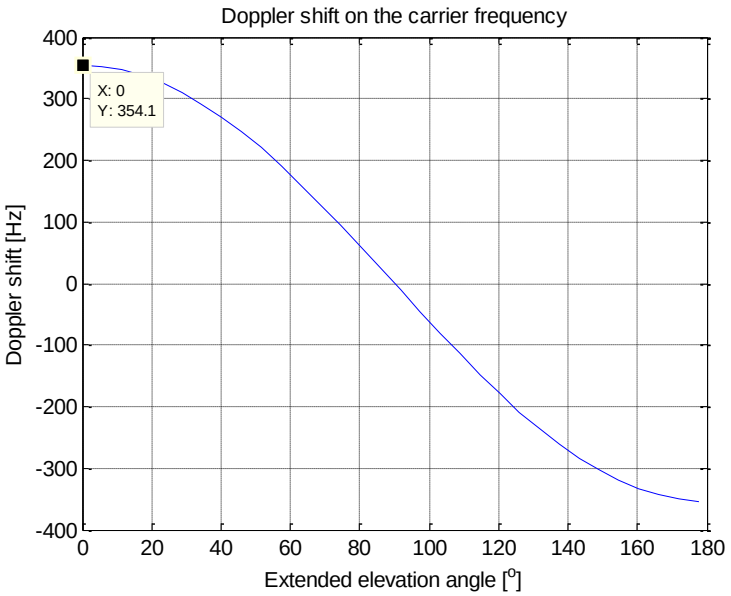

Figure 4-10: Doppler shift on the carrier frequency during polar orbit overpass over the receiver. The maximum Doppler frequency occurs when the satellite is on the horizon. When the satellite is directly overhead, the Doppler frequency is 0 Hz and it decreases as the satellite moves away from the receiver. The extended elevation is used to show the difference between the case when the satellite moves towards the receiver (elevation angles 0˚ to 90˚) and the case when the satellite moves away from the receiver. {Extended elevation angle (180˚ – theta)=90˚ to 180˚, where theta is the conventional elevation angle.}

The Doppler shift is passed through to the baseband signal, which is the difference between the varying frequency at the receiver and the fixed local oscillator frequency of 14.098 MHz. When the satellite moves toward the receiver, the baseband frequency is derived by

$$\begin{aligned} f_b &= (f_c + f_d) - f_{LO}, \\ &= (14.099\times10^6 + 354.1) - (14.098\times10^6) \\ &= 1354.1 \text{ Hz}. \end{aligned} \qquad 4.18$$

Here f_b represents the baseband frequency, f_d denotes the Doppler shift of 354.1 Hz and f_{LO} represents the LO frequency.

Similarly, when the satellite moves away from the receiver, the baseband frequency is calculated as follows:

$$\begin{aligned} f_b &= (f_c - f_d) - f_{LO}, \\ &= (14.099\times10^6 - 354.1) - (14.098\times10^6) \\ &= 645.9 \text{ Hz}. \end{aligned} \qquad 4.19$$

The Doppler shift on the baseband frequency as a function of the extended elevation angle is illustrated in Figure 4-11.

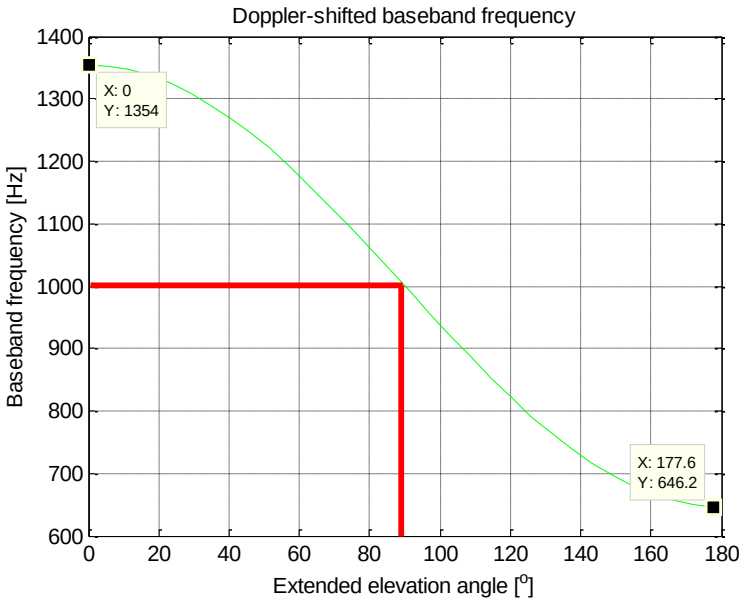

Figure 4-11: Doppler shifted baseband frequency during polar orbit overpass over the receiver. When the satellite is directly overhead, the received baseband frequency is 1 kHz. The extended elevation angle is defined in the caption of Figure 4-10.

4.4 Three-dimensional interferometric principle

At least three antennas are required to estimate the azimuth and elevation angles from the phase differences between the signals received at the three antennas. McNamara, (1999:150) suggested a method of calculating the azimuth and elevation from the three signals, by using the phase difference between the antennas as shown in Figure 4-12. His method was adopted to calculate the DOA from the phase differences between the three signals.

The azimuth and elevation angles were calculated as follows:

$$\alpha = \tan^{-1}\left\{\frac{\Delta\psi_{EW}}{\Delta\psi_{NS}}\right\}\times\frac{180}{\pi}, \tag{4.20}$$

$$k = \left\{\frac{\lambda}{2\pi\times d}\right\}^{2}\times\left\{\Delta\psi_{NS}{}^{2}+\Delta\psi_{EW}{}^{2}\right\}, \tag{4.21}$$

$$\varepsilon = \tan^{-1}\left\{\sqrt{\frac{1}{k}-1}\right\}\times\frac{180}{\pi}. \tag{4.22}$$

Here α denotes the azimuth angle and ε denotes the elevation angle in degrees. k represents the angular wave number, $\Delta\psi_{NS}$ and $\Delta\psi_{EW}$ refer to the phase difference between the reference and first antenna in the southern leg of the array, and between the reference and the first antenna in the western leg of the array respectively.

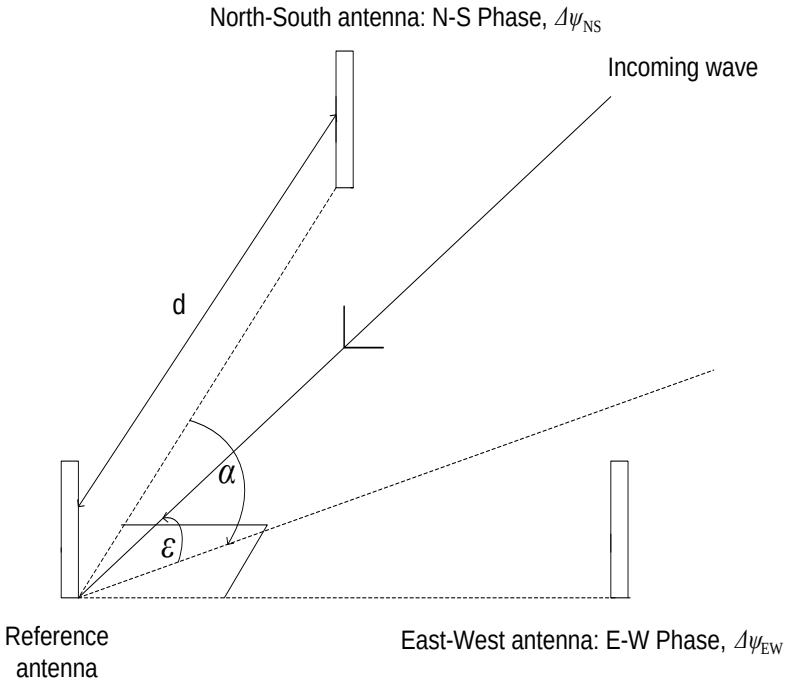

Figure 4-12: Diagram defines the azimuth (α) and elevation (ε) angles to be determined from the phase differences ($\Delta\psi_{NS}$ and $\Delta\psi_{EW}$) of the incoming wave front, using the three-dimensional interferometric principle. The inter-antenna spacing d is the same in the North-South direction and in the East-West direction (Adapted from McNamara, 1999:150)

The method suggested by McNamara, was applied to the three element array arranged in a 3D situation as shown in Figure 4-13, to estimate the phase difference from the time delays.

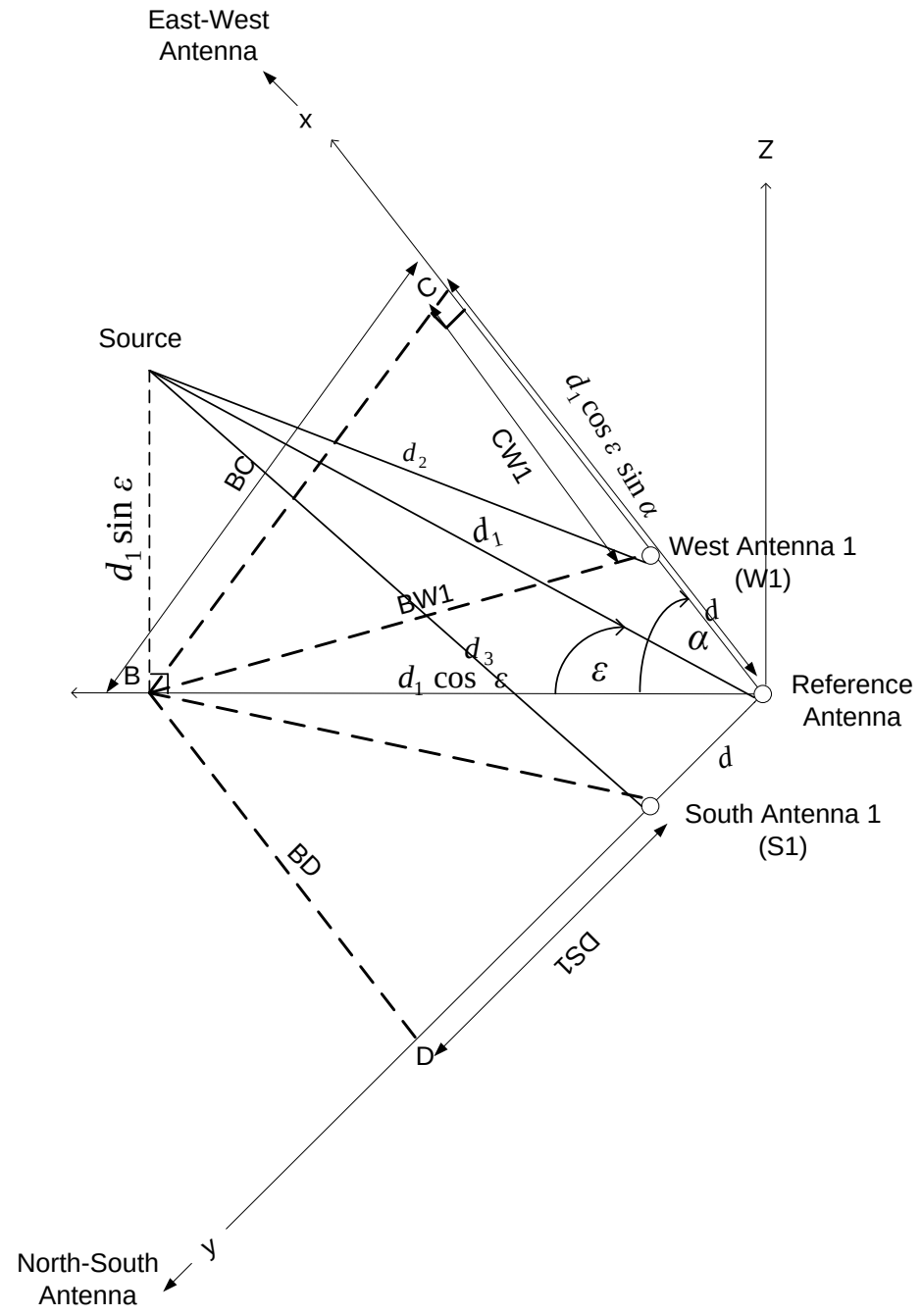

Figure 4-13: The basic geometry to illustrate the azimuth (α) and elevation (ε) angles of a plane wave propagating to three elements at different distances from the source. The elements are Reference antenna, West antenna 1 (W1) and South antenna 1 (S1) (Adapted from McNamara, 1999:150)

An expression for the time delays between the Reference and the West antenna 1 and between the Reference antenna and the South antenna 1 was derived from the differences in the distances of the wave front to the three antennas. The time delays were converted to the phase difference, by multiplying the time delay with the radian frequency (ω).

The following assumptions were made:

1. The phase of the Reference antenna is zero.

2. The distance d between the Reference and West antenna 1 is equal to the distance between the Reference and the South antenna 1.
3. The source is assumed to be very far away, so that d_1, d_2 and d_3 can be assumed to be parallel relative to the dimensions of the L-array, allowing plane wave approximation.

The following notations were used in the formulas to calculate the time delays and phase differences.

BC = $d_1 \cos\varepsilon \cos\alpha$

BD = $d_1 \cos\varepsilon \sin\alpha$

BW1 = $\sqrt{(d_1 \cos\varepsilon \sin\alpha - d)^2} + \sqrt{(d_1 \cos\varepsilon \cos\alpha)^2}$

CW1 = $d_1 \cos\varepsilon \sin\alpha - d$

DS1 = $d_1 \cos\varepsilon \cos\alpha - d$

The time delays and phase differences were calculated as follows.

$$d_2^2 = \left[\sqrt{(d_1 \cos\varepsilon \sin\alpha - d)^2 + (d_1 \cos\varepsilon \cos\alpha)^2}\right]^2 + \left[d_1 \sin\varepsilon\right]^2$$

$$d_2^2 = \left[d_1 \cos\varepsilon \sin\alpha - d\right]^2 + \left[d_1 \cos\varepsilon \cos\alpha\right]^2 + \left[d_1 \sin\varepsilon\right]^2$$

$$= d_1^2 \cos^2\varepsilon \sin^2\alpha - 2d_1 d \cos\varepsilon \sin\alpha + d^2 + d_1^2 \cos^2\varepsilon \cos^2\alpha + d_1^2 \sin^2\varepsilon$$

$$= d_1^2 \cos^2\varepsilon - 2d_1 d \cos\varepsilon \sin\alpha + d^2 + d_1^2 \sin^2\varepsilon$$

$$= d_1^2 + d^2 - 2d_1 d \cos\varepsilon \sin\alpha$$

$$d_2 = \sqrt{\left(d_1^2 + d^2 - 2d_1 d \cos\varepsilon \sin\alpha\right)}$$

$$= d_1 \sqrt{\left(1 + \left[\frac{d}{d_1}\right]^2 - 2\left[\frac{d}{d_1}\right]\cos\varepsilon \sin\alpha\right)}$$

Assume d_1 >> d, then $\left[\frac{d}{d_1}\right]^2$ is negligible compared to 1 and to $\frac{d}{d_1}$, can be neglected, therefore d_2 yields to

$$d_2 = d_1 \sqrt{1 - 2\left[\frac{d}{d_1}\right]\cos\varepsilon \sin\alpha}\ . \qquad 4.23$$

Now a binomial expansion can be used, $(1+x)^n \approx 1 + nx$, for $x << 1$

$$d_2 \approx d_1\left[1 - \frac{d}{d_1}\cos\varepsilon \sin\alpha\right]$$

$$d_2 \approx d_1 - d \cos\varepsilon \sin\alpha$$

The time delay between the Reference and West antenna 1 was then calculated, using Equation 4.24,

$$\Delta t_{W1} = \frac{d_1 - d_2}{c} = \frac{d_1 - (d_1 - d\ \cos\varepsilon \sin\alpha)}{c} = \frac{d\ \cos\varepsilon \sin\ \alpha}{c}. \qquad 4.24$$

Here d_1 is the distance between the source and the Reference antenna in metres, d_2 is the distance between the source and the West antenna 1 in metres, c is the speed of light in m/s, ε is the elevation angle in degrees and α represents the azimuth angle in degrees.

d_3 was calculated as follows:

$$\begin{aligned}
d_3^2 &= \left[d_1\ \cos\varepsilon\cos\ \alpha - d\right]^2 + \left[d_1\ \cos\varepsilon\sin\ \alpha\right]^2 + \left[d_1\ \sin\ \varepsilon\right]^2 \\
&= d_1^2\ \cos^2\varepsilon\ \cos^2\alpha - 2d_1 d\ \cos\varepsilon\cos\ \alpha + d^2 + d_1^2\ \cos^2\varepsilon\ \sin^2\alpha + d_1^2\ \sin^2\varepsilon \\
&= d_1^2\cos^2\varepsilon - 2d_1 d\ \cos\varepsilon\cos\ \alpha + d^2 + d_1^2\ \sin^2\varepsilon \\
&= d_1^2 + d^2 - 2d_1 d\ \cos\varepsilon\cos\ \alpha \\
d_3 &= \sqrt{\left(d_1^2 + d^2 - 2d_1 d\ \cos\varepsilon\sin\ \alpha\right)} \\
&= d_1\sqrt{\left(1 + \left[\frac{d}{d_1}\right]^2 - 2\left[\frac{d}{d_1}\right]\cos\varepsilon\cos\ \alpha\right)}
\end{aligned}$$

Assume d_1 >> d, then $\left[\frac{d}{d_1}\right]^2$ is negligible compared to 1, and to $\frac{d}{d_1}$ can be neglected, therefore d_3 yields Equation 4.25.

$$d_3 = d_1 = \sqrt{1 - 2\left[\frac{d}{d_1}\right]\cos\varepsilon\cos\ \alpha}\ . \qquad 4.25$$

Now a binomial expansion can be used, $(1+x)^n \approx 1 + nx$, for $x << 1$

$$d_3 \approx d_1\left[1 - \frac{d}{d_1}\cos\varepsilon\cos\ \alpha\right]$$

$$d_3 \approx d_1 - d\ \cos\varepsilon\cos\ \alpha$$

The time delay between the Reference antenna and South antenna 1 was calculated, using Equation 4.26, with d_3 the distance between the source and the South antenna 1 in metres.

$$\Delta t_{S1} = \frac{d_1 - d_3}{c} = \frac{d_1 - (d_1 - d\ \cos\varepsilon\cos\alpha)}{c} = \frac{d\ \cos\varepsilon\cos\ \alpha}{c} \qquad 4.26$$

For the given geometry of the array, a positive time delay of the signal received at the West and South antennas means that the signal received by the Reference antenna will be advanced with respect to the West and South antennas. A negative time delay of the signal received at the West and South antennas means that the signal is advanced with respect to the Reference antenna. From the time delays calculated in Equation 4.24 and 4.26, the phase differences between the Reference and the West antenna 1 ($\Delta\psi_{W1}$) and between the Reference and the South antenna 1 ($\Delta\psi_{S1}$) are defined by Equation 4.27 and 4.28 respectively.

$$\Delta\psi_{W1} = \omega\,\Delta t_{W1} = 2\pi f_c\,\frac{d\,\cos\varepsilon\sin\,\alpha}{c} = \frac{2\,\pi}{\lambda_c} d\,\cos\varepsilon\sin\,\alpha\,, \qquad 4.27$$

$$\Delta\psi_{S1} = \omega\,\Delta t_{S1} = 2\pi f_c\,\frac{d\,\cos\varepsilon\cos\,\alpha}{c} = \frac{2\,\pi}{\lambda_c} d\,\cos\,\varepsilon\cos\,\alpha\,. \qquad 4.28$$

Here d is the distance between the Reference and South antenna 1, and is assumed to be the same as the distance between the Reference and the West antenna 1 in metres. λ_c is the wavelength at the carrier frequency (f_c) in metres, ε is the elevation angle in degrees and α represents the azimuth angle in degrees.

The azimuth and elevation angles were derived using Equation 4.29, 4.30 and 4.31. The angles of interest are the azimuth angles in the range 0˚ to 360˚ and elevation angles in the range 0˚ to 90˚.

$$\frac{\Delta\psi_{W1}}{\Delta\psi_{S1}} = \frac{\sin\,\alpha}{\cos\,\alpha}$$

$$\tan\,\alpha = \frac{\Delta\psi_{W1}}{\Delta\psi_{S1}} \quad . \qquad 4.29$$

$$\alpha = \tan^{-1}\left[\frac{\Delta\psi_{W1}}{\Delta\psi_{S1}}\right]$$

Here $\Delta\psi_{W1}$ represents the phase difference between the Reference and the West antenna 1, and $\Delta\psi_{S1}$ represents the phase difference between the Reference and the South antenna 1. The elevation angle was calculated as follows:

$$
\begin{aligned}
k &= \left[\frac{\lambda}{2\pi d}\right]^2 \times \left[\Delta\psi_{W1}{}^2 + \Delta\psi_{S1}{}^2\right] \\
&= \left[\frac{\lambda}{2\pi d}\right]^2 \times \left[\left(\frac{2\pi}{\lambda}\right)^2 \sin^2\alpha\ \cos^2\varepsilon\, d^2 + \left(\frac{2\pi}{\lambda}\right)^2 \cos^2\alpha\ \cos^2\varepsilon\, d^2\right] \\
&= \left[\frac{\lambda}{2\pi d}\right]^2 \times \left[\left(\frac{2\pi}{\lambda}\right)^2 (\sin^2\alpha + \cos^2\alpha)\ \cos^2\varepsilon\, d^2\right] \\
&= \left[\frac{\lambda}{2\pi d}\right]^2 \times \left[\left(\frac{2\pi}{\lambda}\right)^2 \cos^2\varepsilon\, d^2\right] \\
&= \cos^2\varepsilon
\end{aligned}
\qquad 4.30
$$

$$
\begin{aligned}
&\sin^2\varepsilon = 1 - \cos^2\varepsilon \\
&\frac{\sin^2\varepsilon}{\cos^2\varepsilon} = \frac{1-\cos^2\varepsilon}{\cos^2\varepsilon} \\
&\tan^2\varepsilon = \frac{1}{k} - 1 \\
&\tan\varepsilon = \sqrt{\left(\frac{1}{k}\right) - 1} \quad . \\
&\varepsilon = \tan^{-1}\sqrt{\left(\frac{1}{k}\right) - 1}
\end{aligned}
\qquad 4.31
$$

Equations 4.29, 4.30 and 4.31 were used to estimate the azimuth and elevation angles from the estimates of the phases $\Delta\psi_{S1}$ and $\Delta\psi_{W1}$.

The three baseband signals that were used in simulations to determine the phase difference between the Reference antenna, and the two orthogonal antennas are represented by Equation 4.32,

$$
\begin{aligned}
b_{ref}\ (t) &= \frac{1}{2}\ A_{ref}\ \times A_o \times\ \cos\left[2\pi\left(f_c - f_o\right)t\right] + n_{ref}\ (t), \\
S_1\ (t) &= \frac{1}{2} A_{S1}\ \times A_o \times\ \cos\left[2\pi\left(f_c - f_o\right)t - \Delta\psi_{S1}\right] + n_{S1}(t), \\
W_1\ (t) &= \frac{1}{2} A_{W1}\ \times A_o\ \times \cos\left[2\pi\left(f_c - f_o\right)t - \Delta\psi_{W1}\right] + n_{w1}(t).
\end{aligned}
\qquad 4.32
$$

Here b_{ref} , $S_1(t)$ and $W_1(t)$ represent the three baseband signals observed at the Reference, South and West antennas respectively. A_{ref} , A_{S1}, A_{W1} and A_o are the amplitudes of the Reference, South, West and the LO signals. In the simulations all amplitudes were assumed to be unity without loss of generality, since none of the algorithms are affected by the

amplitudes of the signals, but in reality the amplitude may vary. The angles $\Delta\psi_{W1}$ and $\Delta\psi_{S1}$ represent the phase differences of the RF signals which appear also in the baseband signals between the Reference, South and West antenna 1 signals (see Equations 4.27 and 4.28). The parameters $n_{ref}(t)$, $n_{S1}(t)$, $n_{w1}(t)$ represent the Gaussian noise added to the three baseband signals, while f_c denotes the carrier frequency of 14.099 MHz plus or minus the Doppler shift and f_o represents the LO frequency of 14.098 MHz.

Equations 4.27 and 4.28 were used to compute the values of the phase differences $\Delta\psi_{W1}$ and $\Delta\psi_{S1}$ for selected values of azimuth and elevation angles. Equations 4.32 with $f_c - f_o$ were used to generate time series to simulate the baseband signals derived from the signals at each antenna. These noisy time series were then processed by each of the algorithms to recover the values of the azimuth and elevation angles. The method used to map the phase differences $\Delta\psi_{S1}$ and $\Delta\psi_{W1}$ to azimuth and elevation angles, is the same for every algorithm and is given by Equations 4.29 through 4.31. The algorithms to extract the phase differences $\Delta\psi_{S1}$ and $\Delta\psi_{W1}$ from the time series will be discussed in the next chapter. Theoretical calculations of the phase differences for selected azimuth and elevation angles set from different quadrants now follow. These calculations both serve to demonstrate typical values of the parameters, and to check the computer implementation of these algorithms.

Quadrant 1: Azimuth in the range of 0˚ to 90˚: For a selected azimuth of 68˚ and elevation of 65˚, the signals at the South and West antenna 1 are both delayed relative to the Reference antenna signal. Therefore the values of the two angles $\Delta\psi_{S1}$ and $\Delta\psi_{W1}$ are both positive.

$$\Delta\psi_{S1} = \omega\,\Delta t_{S1} = 2\pi f_c \frac{d\,\cos\varepsilon\,\cos\alpha}{c} = \frac{2\pi}{\lambda_c} d\,\cos\,\varepsilon\,\cos\,\alpha$$
$$= \frac{2\pi}{21.28} \times 10 \times \cos(65^\circ) \times \cos(68^\circ)$$
$$= 0.467 \times \frac{180}{\pi} \qquad 4.33$$
$$= 26.78^\circ$$

$$\Delta\psi_{W1} = \omega\ \Delta t_{W1} = 2\pi f_c \ \frac{d\,\cos\varepsilon \sin\,\alpha}{c} = \frac{2\pi}{\lambda_c} d\,\cos\,\varepsilon\,\sin\,\alpha$$
$$= \frac{2\pi}{21.28} \times 10 \times \cos(65^\circ) \times \sin(68^\circ) \qquad 4.34$$
$$= 1.1569 \times \frac{180}{\pi}$$
$$= 66.28^\circ$$

Quadrant 2: Azimuth in the range of 90˚ to 180˚: For a selected azimuth of 120˚ and elevation of 75˚, the signal at the West antenna 1 is delayed, leading to a positive value of $\Delta\psi_{W1}$ relative to the Reference antenna. The South antenna 1 signal is advanced, leading to a negative value of $\Delta\psi_{S1}$ relative to the Reference antenna signal.

$$\Delta\psi_{S1} = \omega\,\Delta t_{S1} = 2\pi f_c \frac{d\,\cos\varepsilon\,\cos\alpha}{c} = \frac{2\pi}{\lambda_c} d\,\cos\,\varepsilon\,\cos\,\alpha$$
$$= \frac{2\pi}{21.28} \times 10 \times \cos(75^\circ) \times \cos(120^\circ)$$
$$= -0.3821 \times \frac{180}{\pi} \qquad 4.35$$
$$= -21.89^\circ$$

$$\Delta\psi_{W1} = \omega\,\Delta t_{W1} = 2\pi f_c \frac{d\,\cos\varepsilon\sin\,\alpha}{c} = \frac{2\pi}{\lambda_c} d\,\cos\,\varepsilon\,\sin\,\alpha$$
$$= \frac{2\pi}{21.28} \times 10 \times \cos(75^\circ) \times \sin(120^\circ) \qquad 4.36$$
$$= 0.662 \times \frac{180}{\pi}$$
$$= 37.92^\circ$$

Quadrant 3: Azimuth in the range of 180˚ to 270˚: For a selected azimuth of 247˚ and elevation of 55˚, the South and West antenna 1 signals are both advanced, leading to negative values of both $\Delta\psi_{S1}$ and $\Delta\psi_{W1}$ relative to the Reference antenna signal.

$$\Delta\psi_{S1} = \omega\,\Delta t_{S1} = 2\pi f_c \frac{d\,\cos\varepsilon\,\cos\alpha}{c} = \frac{2\pi}{\lambda_c} d\,\cos\,\varepsilon\,\cos\,\alpha$$
$$= \frac{2\pi}{21.28} \times 10 \times \cos(55^\circ) \times \cos(247^\circ)$$
$$= -0.6617 \times \frac{180}{\pi} \qquad 4.37$$
$$= -37.91^\circ$$

$$\Delta\psi_{W1} = \omega\,\Delta t_{W1} = 2\pi f_c \frac{d\,\cos\varepsilon\sin\,\alpha}{c} = \frac{2\pi}{\lambda_c} d\,\cos\,\varepsilon\,\sin\,\alpha$$
$$= \frac{2\pi}{21.28} \times 10 \times \cos(55^\circ) \times \sin(247^\circ) \qquad 4.38$$
$$= -1.558 \times \frac{180}{\pi}$$
$$= -89.31^\circ$$

Quadrant 4: Azimuth in the range of 270˚ to 360˚: For a selected azimuth of 355˚ and elevation of 65˚, the West antenna 1 signal is advanced, therefore, the value of $\Delta\psi_{W1}$ is negative relative to the Reference signal. The South antenna 1 signal is delayed, leading to the positive value of $\Delta\psi_{S1}$ relative to the Reference antenna signal.

$$\Delta\psi_{S1} = \omega\,\Delta t_{S1} = 2\pi f_c \frac{d\,\cos\varepsilon\,\cos\alpha}{c} = \frac{2\pi}{\lambda_c} d\,\cos\,\varepsilon\,\cos\,\alpha$$
$$= \frac{2\pi}{21.28} \times 10 \times \cos(65^\circ) \times \cos(355^\circ)$$
$$= 1.2430 \times \frac{180}{\pi} \qquad 4.39$$
$$= 71.22^\circ$$

$$\Delta\psi_{W1} = \omega\,\Delta t_{W1} = 2\pi f_c \frac{d\,\cos\varepsilon\sin\,\alpha}{c} = \frac{2\pi}{\lambda_c} d\,\cos\,\varepsilon\,\sin\,\alpha$$
$$= \frac{2\pi}{21.28} \times 10 \times \cos(65^\circ) \times \sin(355^\circ) \qquad 4.40$$
$$= -0.1087 \times \frac{180}{\pi}$$
$$= -6.23^\circ$$

4.5 Noise Evaluation

Noise is considered a limiting factor in the performance of any communication system. Noise is defined as an unwanted signal that corrupts a wanted signal. In signal measurements, there is always a problem of distinguishing the noise from the real signal (Pozar, 2009:486). The quality of the signal is often expressed as the SNR, which is defined as the ratio of the power of the wanted signal to the power of the unwanted signal (noise), or the ratio of the amplitude of the wanted signal to the amplitude of the unwanted signal. There is a difference between noise that is added to the transmitted signal and the noise measured in the receiver. The noise that is added to the signal is generated externally along the ray path of the signal. The external noise includes atmospheric noises, extraterrestrial noise and man-made noises. External noise is uncontrollable. The noise in the receiver is generated internally by the receiver circuitry, however, internal noise can be controlled, by optimising the design of some of the devices in the receiver, such as a low noise amplifier (LNA) (Pozar, 2009:486). For the simulations, the computer-generated random Gaussian noise of a selected SD was added to the simulated baseband signals to control the SNR.

The idea is to determine the input SNR from the signal power and applied noise power or from signal amplitude and applied noise amplitude. Let S be the signal power in mW and N be the noise power in mW, then the S/N can be expressed as in Equation 4.40. The S/N is derived from amplitude ratios using Equation 4.42 (Pozar, 2009:493).

$$\left(\frac{S}{N}\right)_{\text{ratio}} = \frac{S}{N}$$
$$\left(\frac{S}{N}\right)_{\text{dB}} = 10\ \log\left(\frac{S}{N}\right) \quad , \tag{4.41}$$

$$\left(\frac{S}{N}\right)_{\text{dB}} = 20\ \log\left(\frac{A_{\text{signal}}}{A_{\text{noise}}}\right). \tag{4.42}$$

The SNR varies at each stage in a communication system and gives an indication of the system quality and the performance of the system in terms of errors. When the SNR is larger, the system generally performs better, and as the value of the SNR decreases, the performance of the system deteriorates. The performance of each algorithm was also evaluated for accuracy. The noise added to the baseband signals, $n_{\text{ref}}(t)$, $n_{\text{S1}}(t)$ and $n_{\text{w1}}(t)$ in Equation 4.32, was assumed to be uncorrelated Gaussian noise (Dhull *et al*., 2010:29), which takes into account all the external and internal noises generated by signal transmission. An example of a Gaussian noise signal plot is seen in Figure 4-14. The Gaussian noise added to the baseband signals result in errors in the estimation of the azimuth and elevation angles.

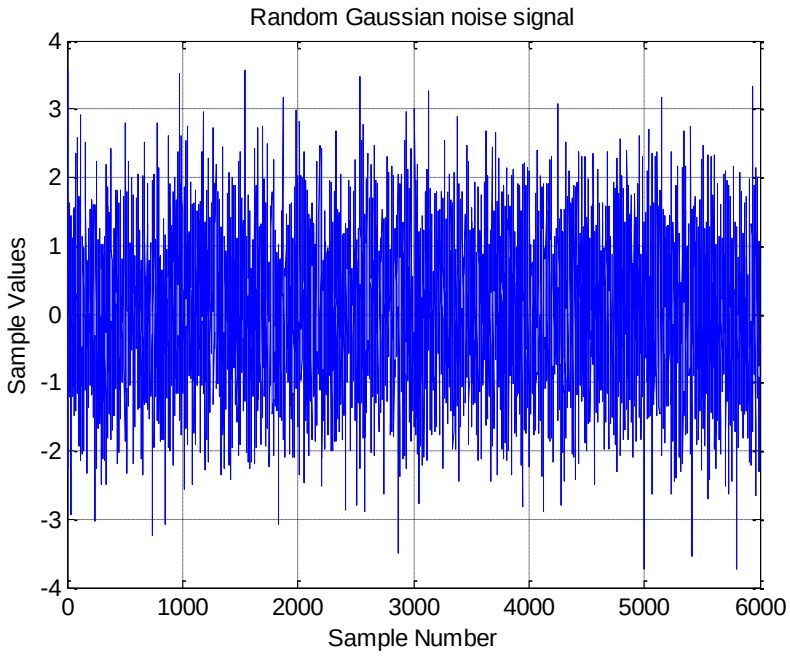

Figure 4-14: Plot of Gaussian noise signal with a zero mean and a variance of 1 over 6000 samples

4.6 DOA Error estimation

The estimation errors for the azimuth and elevation angles are calculated as the difference between the estimated (azimuth angle, elevation angle) and the input (azimuth angle, elevation angle) of the simulated baseband signals. The SD of the DOA error was determined for each algorithm by means of Monte Carlo simulations for every set of angles.

A Monte Carlo simulation is a mathematical technique that does multiple runs to estimate the probability of certain outcomes, using random variables. The main aim of the Monte Carlo simulation is to determine how the estimated errors are distributed. A typical Monte Carlo simulation calculates the outcomes a hundred or thousand times for every run, using selected values and independent noise for each run. The estimation errors of each set of input angles were calculated for every simulation. The results were used to calculate the mean and the SD for each set of angles that were tested.

4.7 Characterisation of the distribution of the DOA errors

Five different methods were used to characterise or evaluate the distribution of the DOA errors in the simulation. They are error maps, error mean maps, SD maps, histograms and probability distribution functions (PDF).

4.7.1 Error maps

Error maps characterise the distribution of the DOA errors for all azimuth (0˚ to 360˚) angles in steps of 18˚ and elevation angles (0˚ to 90˚) in 9˚ steps. The error maps were used to characterise the distribution of the errors for various combinations of DOA. Error maps were generated for a single simulation of each DOA.

4.7.2 Error mean maps

Mean error maps characterise the distribution of the mean of the DOA errors for all azimuth angles (0˚ to 360˚) in steps of 18˚ and elevation angles (0˚ to 90˚) in steps of 9˚. The error mean maps were used to characterise the distribution of the mean of the errors for various combinations of DOA. The error mean maps were generated from several Monte Carlo simulations of each DOA.

4.7.3 SD maps

SD maps demonstrate the distribution of the SD of the DOA errors for all azimuth angles (0˚ to 360˚) in steps of 18˚ and elevation angles (0˚ to 90˚) in steps of 9˚. The SD maps were

used to characterise the distribution of the SD of the DOA errors for various combinations of DOA. The SD maps were generated from several Monte Carlo simulations of each DOA.

4.7.4 Histograms

Histograms are very useful for characterising the spread of data from Monte Carlo simulations and for determining the probability of the experimental data. Histograms are used regularly to calculate the mean and the SD of very large sets of data (Smith, 1997:20). The number of Monte Carlo simulations used significantly influences the smoothness of the histograms. A large number of runs results in a much smoother appearance of the histogram (Smith, 1997:20). The histograms were used to display the distribution of the estimation DOA errors versus the number of occurrences of a particular error, for specific azimuth and elevation angles.

4.7.5 Probability distribution

Probability distribution describes all the possible values that a random variable can take in a certain range. Gaussian noise is assumed to have a Gaussian distribution or normal distribution. The probability distribution function (PDF) of Gaussian noise is expressed by Equation 4.43 (Cheng *et al*., 2013:7)

$$P(x)=\frac{1}{\sigma\sqrt{2\pi}}e^{-\frac{(x-\mu)^2}{2\sigma^2}}. \qquad 4.43$$

Here μ denotes the mean, σ represents the SD or root mean square error (RMSE) and x represents the experimental values or the measured data. The mean of the normal distribution is the centre of the distribution, while the SD indicates how the distribution is spread around the mean (Smith, 1997:27).

In this thesis, the focus is on the SD of the estimated errors. Figure 4-15 gives an example of a theoretical PDF fitted on simulated histograms of the error distribution.

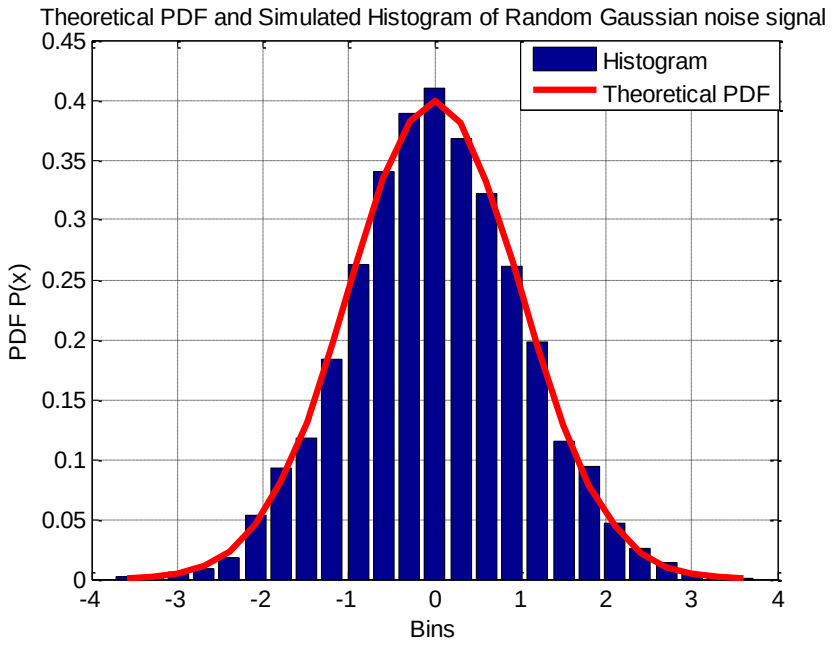

Figure 4-15: The theoretical PDF and simulated histogram of a Gaussian noise signal with a zero mean and a variance of 1

4.8 SD of the estimated errors (azimuth and elevation errors)

The SD of the errors in the estimation of the DOA is computed from a square root of averaged square errors taken over repeated DOA estimation trials (Liang, 2009).The SD of the estimated errors is described by:

$$\text{SD (estimated errors)} = \sqrt{\frac{1}{N}\sum_{n=1}^{N}(\theta_n - \hat{\theta}_n)^2}\ . \qquad 4.44$$

N = number of Monte Carlo simulations

θ_n = specific estimated azimuth or elevation angle of the simulated received signal

$\hat{\theta}_n$ = specific input azimuth or elevation angle of the simulated received signal

The results of the estimated DOA errors vary for every combination set of angles. The magnitude of the SD of the estimated DOA errors was used to evaluate the accuracy of each algorithm averaged over repeated Monte Carlo simulations. The SD measures the spread of the estimated DOA errors over a certain range. When the estimated DOA errors have a wide range, the SD is large. The SD is smaller when the estimated DOA errors are spread closer to the mean. The SD of the Gaussian curve that fits the histogram of the estimated DOA errors results in a wider curve for a high SD and narrower curve for a low SD of the estimated errors (Bland & Altman, 1996).

4.9 Summary

The process of deriving the baseband signals from the RF signals was demonstrated. The influence of Doppler shift was investigated. The effects of Doppler shift will be presented in the next chapter to determine whether the algorithms are affected by the Doppler shift. The method of detecting the DOA from the phase difference between two signals was described. The effects of noise on the estimation of the DOA were highlighted. The SD of the estimated DOA errors as a measure of the accuracy of the DOA estimation was discussed, and the methods that were used to evaluate the SD of the estimated DOA errors were explained. The application of the theory offered in this chapter to the evaluation of the algorithms for phase difference estimation is discussed in the next chapter.

CHAPTER FIVE: RESULTS

5.1 Introduction

In this chapter algorithms that estimate the phase difference between signals of the same frequency are evaluated. The algorithms are Zero Crossing (ZC), Fast Fourier Transform (FFT), Cross Correlation (CC) and Cross Power Spectral Density (CPSD). The process of generating the time series baseband signals for each of the antennas is described. The effect of Doppler shift on the algorithms is evaluated. The characteristic of each algorithm in the estimation of the phase difference between signals is highlighted and the estimations derived from each algorithm are given.

The performance of each algorithm is evaluated with simulated baseband signals. All simulations are for a three-element L-shaped array with a distance of half a wavelength (10 m) between the elements. Gaussian noise was added to the simulated baseband signals. The SNR was controlled by setting the noise amplitude. The algorithms were demonstrated to estimate the DOA correctly for high SNR levels. The performances of the algorithms were poor at low SNR levels.

Baseband signal generation:

The time series representation of the three baseband signals as would be received by each antenna, was generated. In theory, one cycle at baseband should be sufficient to estimate the phase difference between signals. However, simulations indicated that increasing the total time for receiving signals to get more cycles at baseband, resulted in a smaller SD of the estimation errors, as compared to fewer cycles. This is shown in Appendix A. Figure 5-1 and Figure 5-2 shows the time series representation of the baseband signals with a good SNR of 40 dB and a poor SNR of 10 dB, respectively.

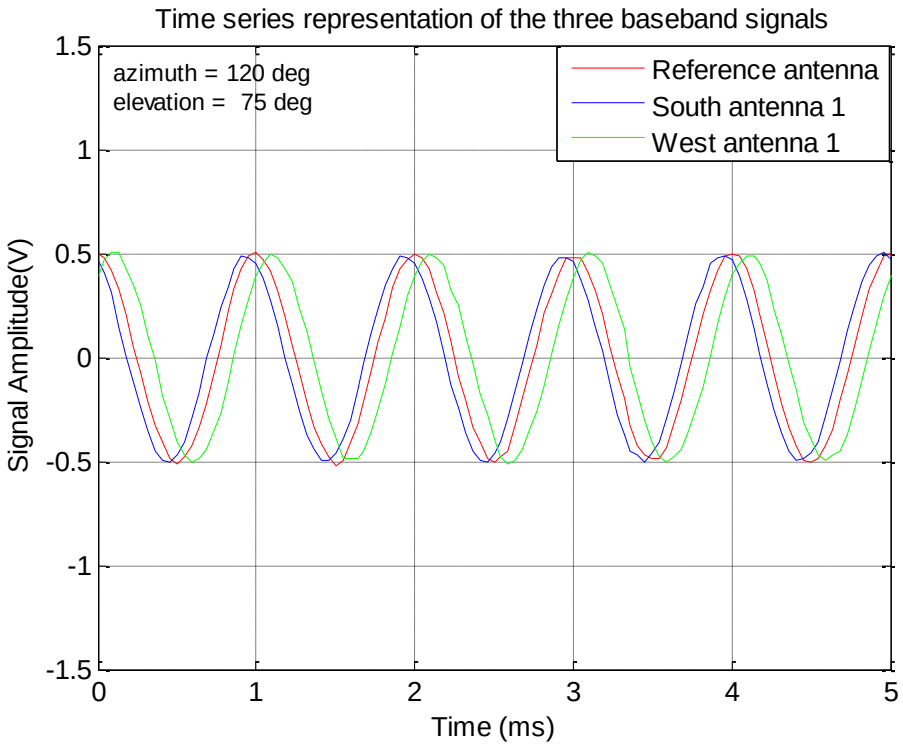

Figure 5-1: The first 5 ms of the time series representation of the baseband signals, with the incoming signal at an azimuth angle of 120° and elevation angle of 75°, and an SNR of 40 dB. The South antenna signal is advanced relative to the Reference antenna signal, while the West antenna signal is delayed relative to the Reference antenna signal. The duration of the realisation of the signal was 1 s sampled at 22 ks/s (kilo samples per second)

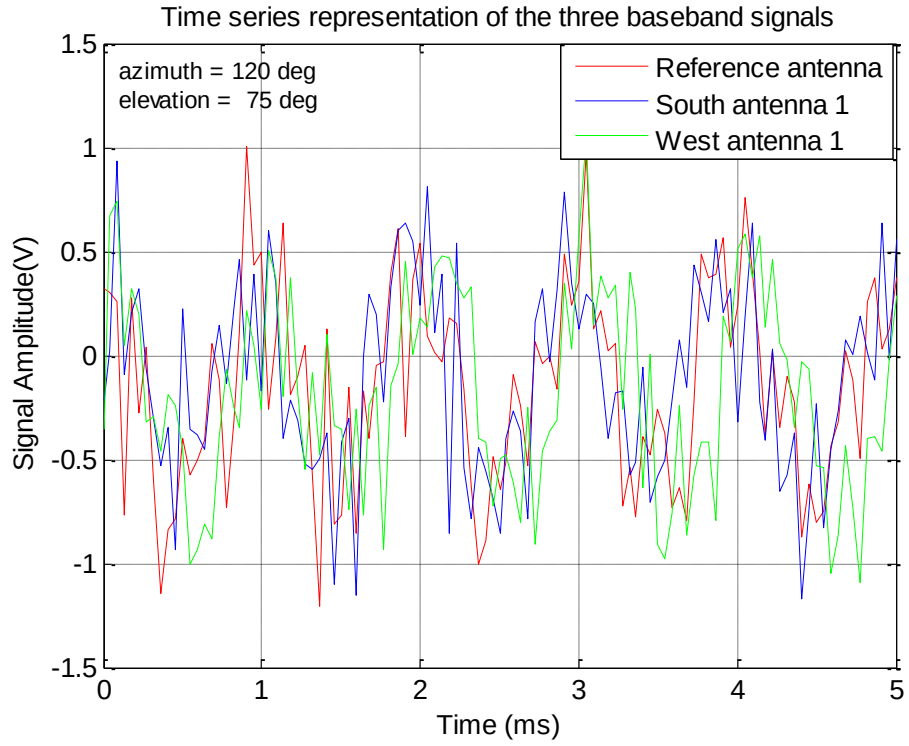

Figure 5-2: The first 5 ms of the time series representation of the baseband signals, with the incoming signal at an azimuth angle of 120° and elevation angle of 75°, and an SNR of 10 dB. In other respects, the same conditions apply as in Figure 5-1

5.2 Effects of Doppler shift on the results

A calculation of Doppler shift was done to determine how sensitive the algorithms are to the Doppler shift. Figures 5-3 to 5-4 illustrate the effect of Doppler shift on all the algorithms for the case when the satellite moves toward the receiver (when the Doppler shift is maximum and positive). Figures 5-5 to 5-6 illustrate the effect of the Doppler shift on all the algorithms for the case when the satellite moves away from the receiver (when the Doppler shift is maximum and negative). The analyses were based on the SD of the azimuth and elevation errors for a good SNR of 40 dB for each algorithm. The results are presented by means of SD error maps. The SD error maps illustrate the distribution of the SD of the azimuth and elevation errors for all combination sets of angles. Each block on the SD error maps represents the SD of the errors for a particular azimuth and elevation combination.

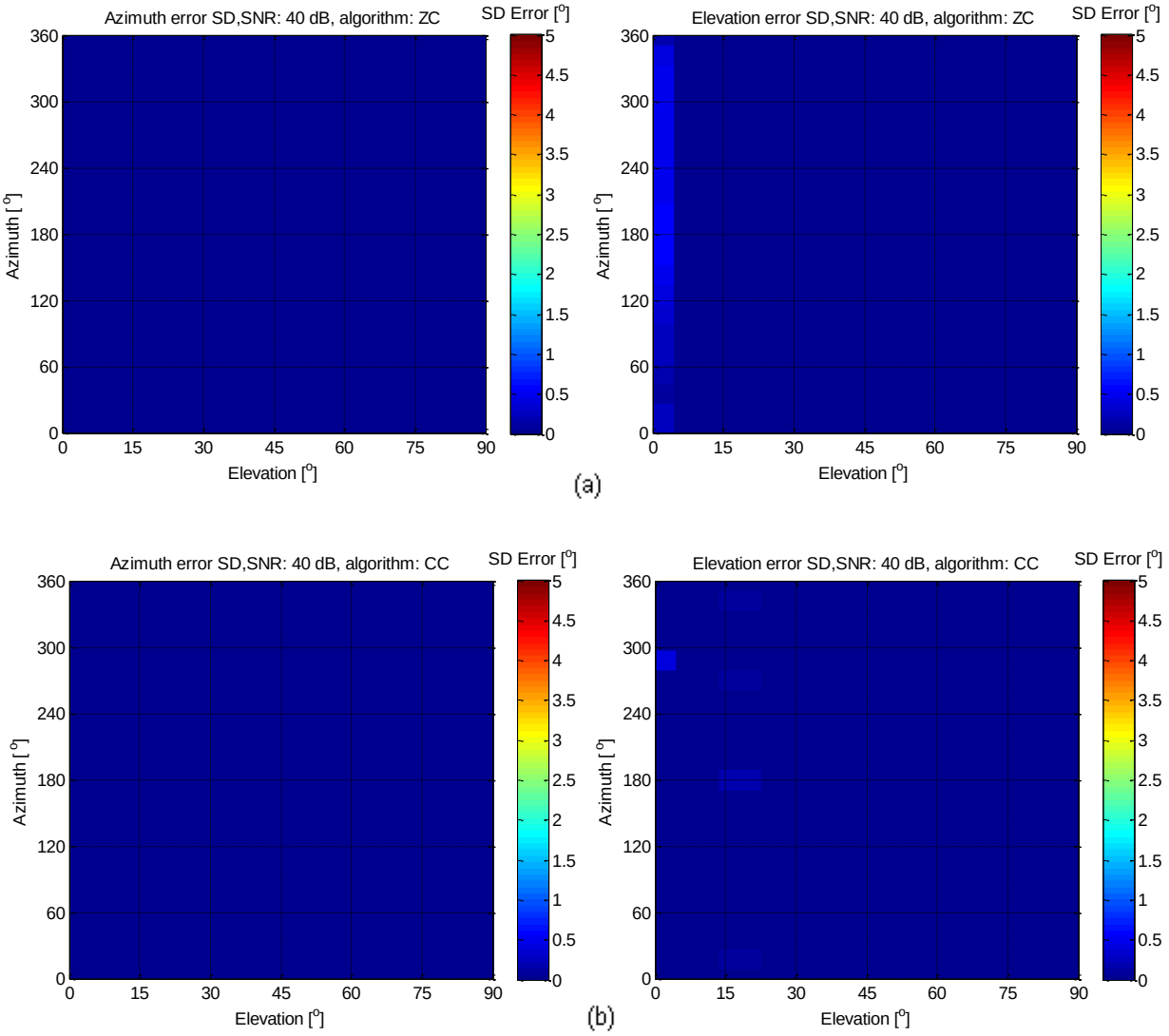

Figure 5-3: The SD of the azimuth and elevation error distribution for all azimuth and elevation angles for the (a) ZC algorithm and (b) CC algorithm. The duration of the signal is 1 s sampled at 22 ks/s. The SD of the azimuth and elevation errors was determined after 50 Monte Carlo simulations. The baseband frequency is 1000 Hz + 354.1 Hz. The RF frequency is 14.099 MHz + 354.1 Hz while the satellite approaches the receiver

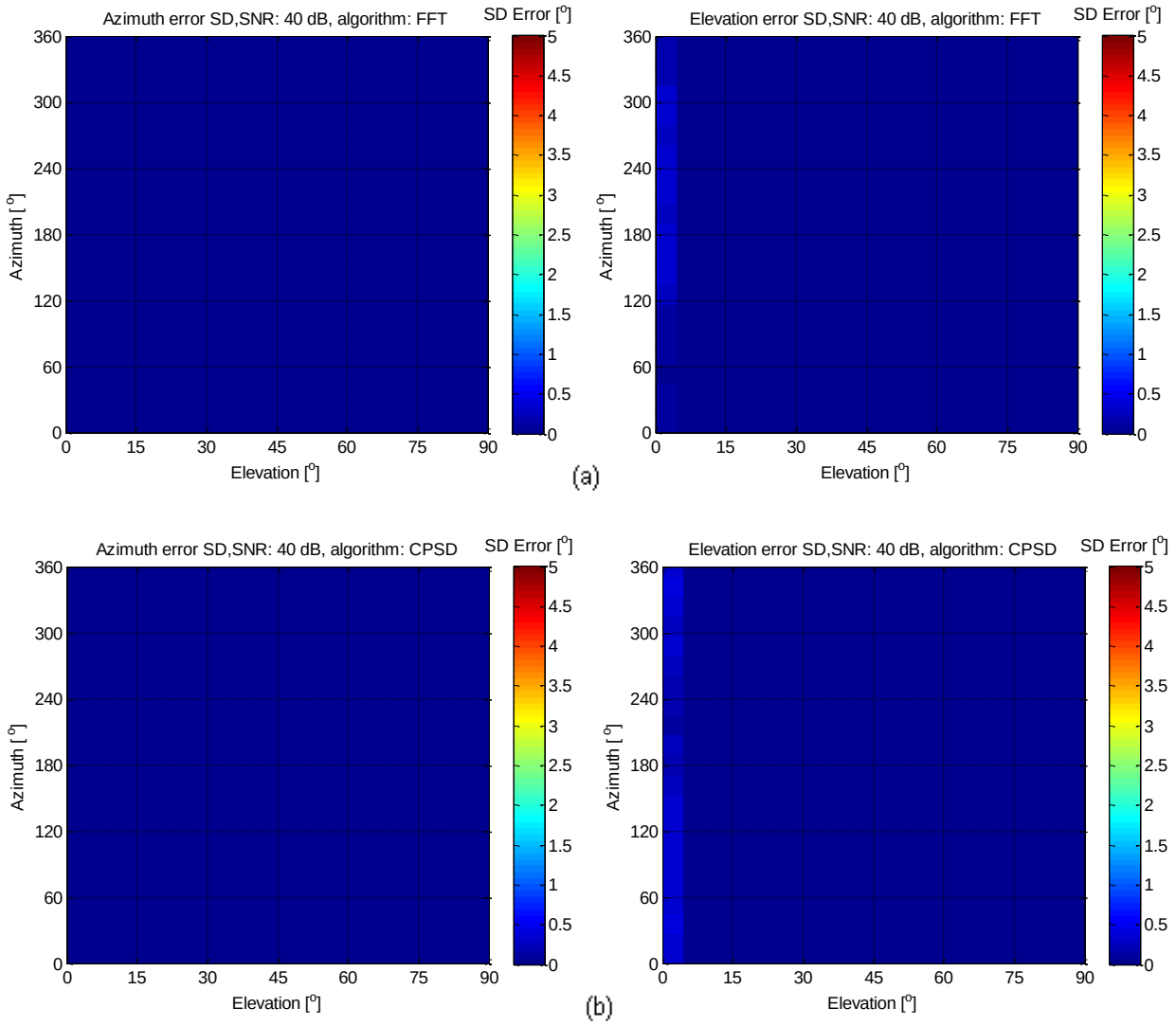

Figure 5-4: The SD of the azimuth and elevation error distribution for all azimuth and elevation angles for the (a) FFT algorithm and (b) CPSD algorithm. The duration of the signal is 1 s sampled at 22 ks/s. The SD of the azimuth and elevation errors was determined after 50 Monte Carlo simulations. The baseband frequency is 1000 Hz + 354.1 Hz. The RF frequency is 14.099 MHz + 354.1 Hz while the satellite approaches to the receiver

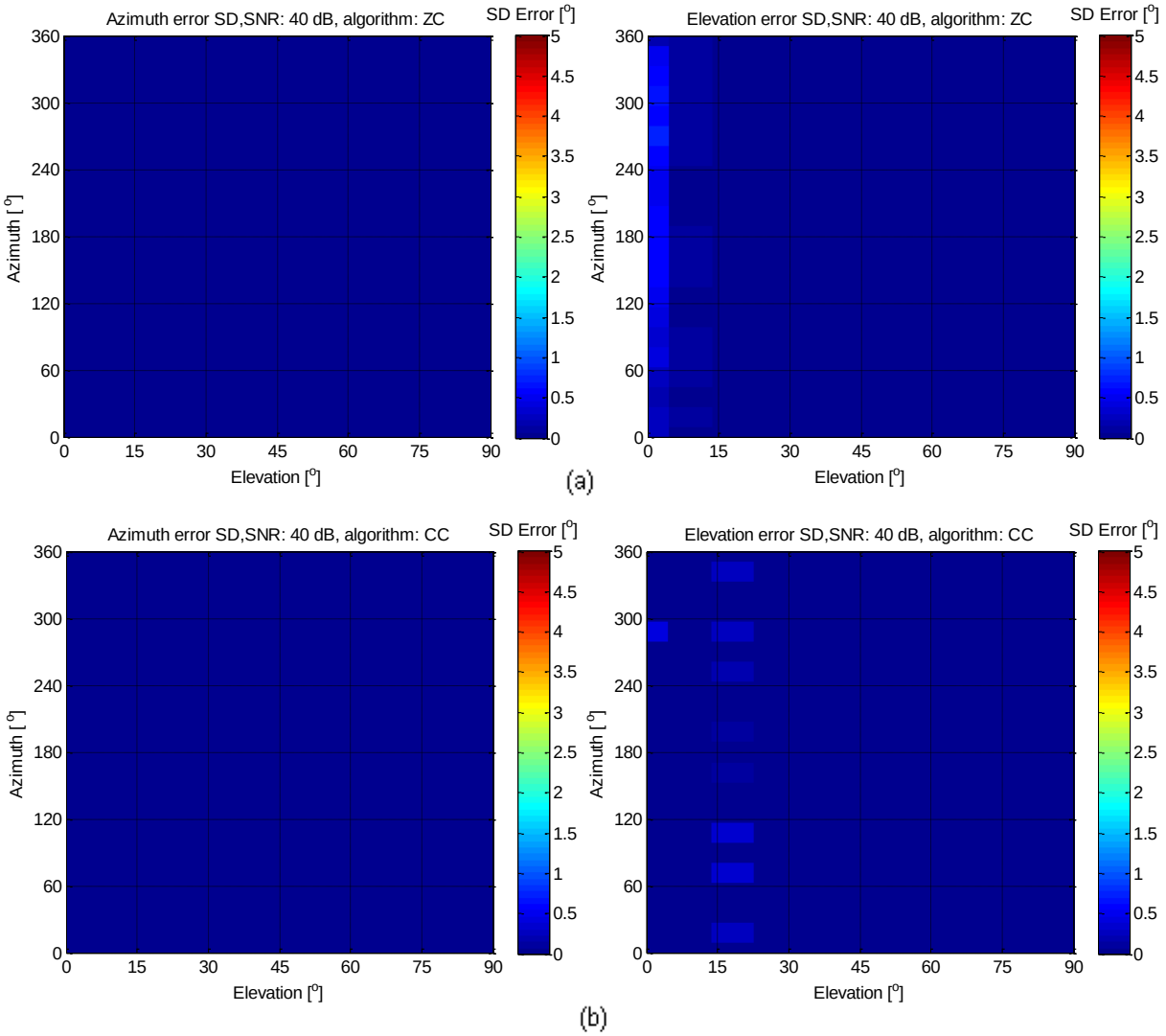

Figure 5-5: The SD of the azimuth and elevation error distribution for all azimuth and elevation angles for the (a) ZC algorithm and (b) CC algorithm. The baseband frequency is 1000 Hz – 354.1 Hz. The RF frequency is 14.099 MHz − 354.1 Hz as the satellite moves away from the receiver. In other respects, the same conditions apply as in Figure 5-3

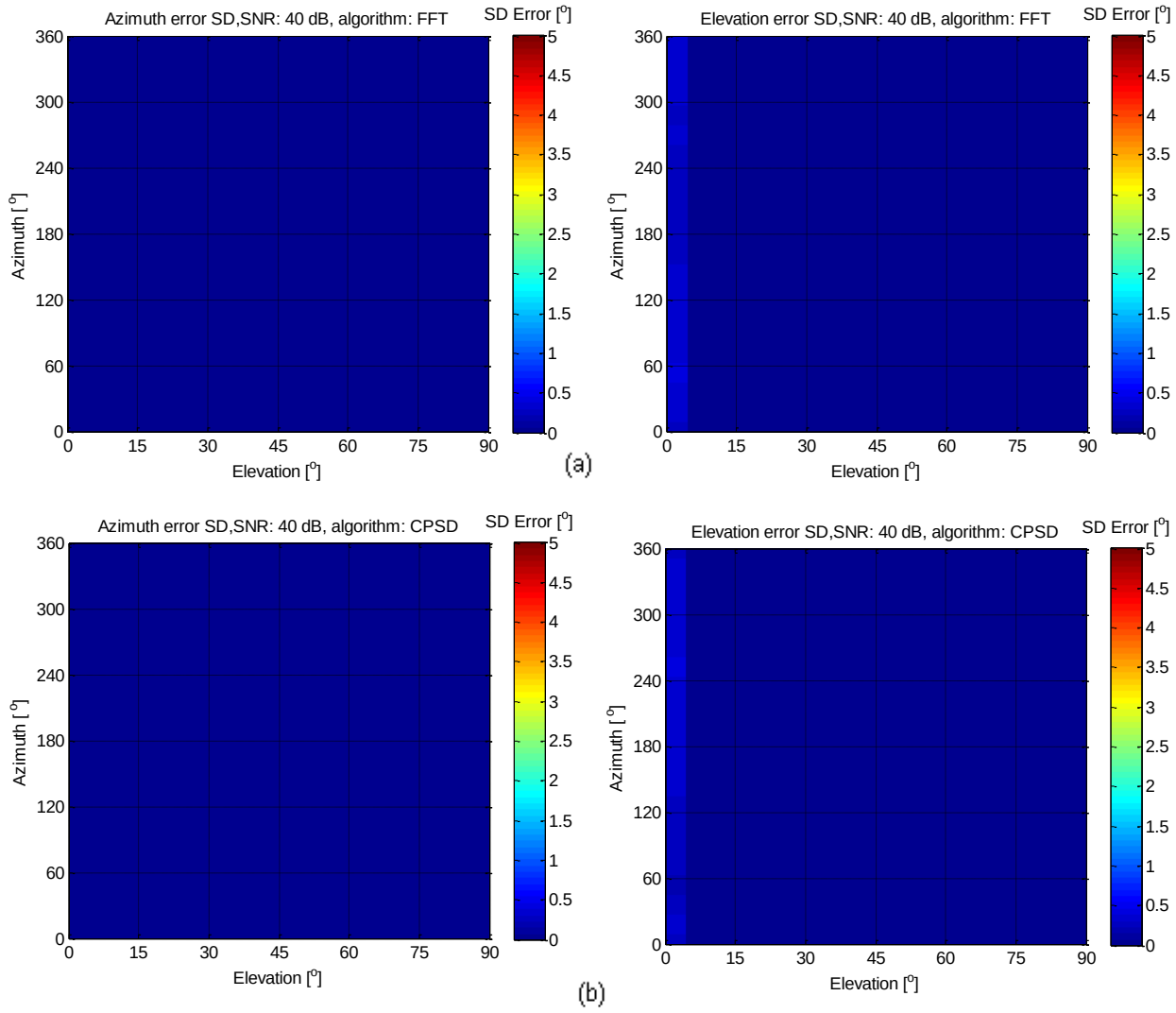

Figure 5-6: The SD of the azimuth and elevation error distribution for all azimuth and elevation angles for the (a) FFT algorithm and (b) CPSD algorithm. The baseband frequency is 1000 Hz – 354.1 Hz. The RF frequency is 14.099 MHz − 354.1 Hz as the satellite moves away from the receiver. In other respects, the same conditions apply as in Figure 5-4

Figures 5-3 through 5-6 prove that the algorithms evaluated in this thesis are robust and not affected by the Doppler shift. The Doppler shift has no effect on the SD of the azimuth and elevation errors. The SD of the azimuth and elevation errors of all algorithms remains smaller than 1°. The results of the error analysis and for the selection of the optimum algorithm are based on a baseband frequency of 1 kHz.

The fact that a sufficient number of samples will be collected for the estimation of the DOA even at the lowest Doppler shifted frequency, and that the number of samples per cycle at the highest Doppler shifted frequency (which is 22 ks/s) are sufficient, was demonstrated through the negligible effect of the variation in the received baseband frequency on the performance of the algorithms.

5.3 Zero Crossing (ZC) algorithm

The ZC is one of the most common techniques for estimating the time delay (time difference) between propagating signals. The phase difference is estimated from detection of the time difference when the signals cross the zero point with either positive or negative slope. The ZC algorithm is independent of the amplitude of the signals. However, due to noise, some incorrect ZC points occur that may result in incorrect estimate of the phase difference. There are many ways to detect or measure the ZC points. These are described by Ankita *et al*. (2013:835). In Figure 5-7 the real ZC point between points a and b was computed with a simple linear interpolation method. Point a represents a point before the real ZC point and point b represents a point after the real ZC point.

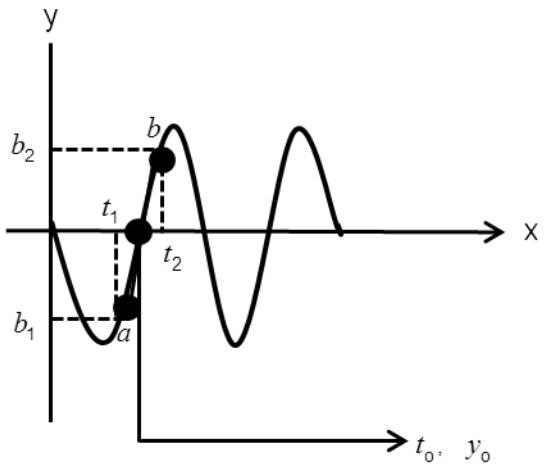

Figure 5-7: The real ZC point on the positive slope between points a and b was computed with simple linear interpolation method

5.2.1 Phase difference estimation using the ZC algorithm

This section describes how the ZC algorithm estimates the phase difference between the signals. Figure 5-8 shows the ZC points detected on the Reference, South and West antenna signals simultaneously.

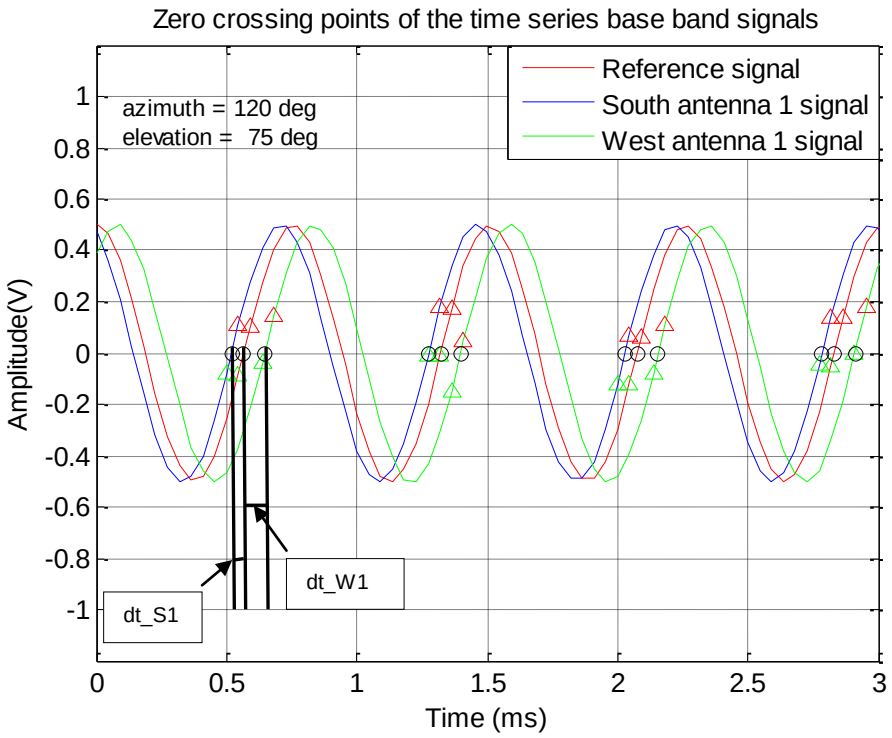

Figure 5-8: The time series representation of the three simulated baseband signals for a specific azimuth angle of 120° and elevation angle of 75°. The SNR is 40 dB. The actual ZC points are represented by the black dots in the Figure. The green triangle represents the point before the real ZC point, while the red triangle represents the point after the real ZC point

The excerpt of the code attached in Appendix D illustrates how the ZC points of each baseband signal from each antenna were calculated. The code calculates the ZC points on the Reference antenna (t0_ref), South antenna 1 (t0_S1) and West antenna 1 (t0_W1) signals by means of the linear interpolation method.

In Figure 5-8, with a 1 s time series and SNR = 40 dB, four ZC points were calculated for each of the Reference, South and West simulated baseband antenna signals. Since the x-axis is limited to 3 ms, only four ZC points are shown. However, in reality, with the time series of the 1 s baseband signals, 1000 ZC points are calculated for each of the Reference, South and West antenna 1 signals. When the SNR is poor, the ZC algorithm detects incorrect multiples of the ZC points. Incorrect ZC points cause the number of ZC points detected for each of the Reference, South antenna 1 and West antenna 1 signals to differ. Consequently, the subtraction of the time differences between the Reference, South antenna 1 and West antenna 1 will be difficult to perform. At low SNR the ZC algorithm results in large errors, because the estimated time differences may not be correct, due to incorrect ZC points. Figure 5-9 illustrates the incorrect ZC for a poor SNR of 10 dB.

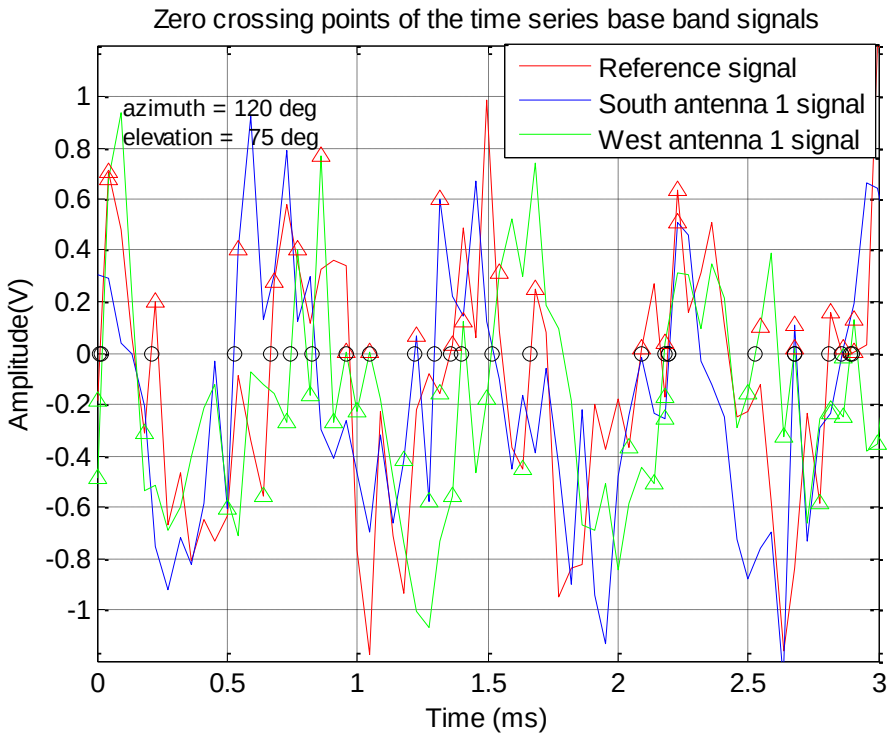

Figure 5-9: The time series representation of the three baseband signals for an azimuth angle of 120° and elevation angle of 75°. The SNR is 10 dB. The signals are sampled at 22 ks/s and the duration of the realisation of the signal is 1 s

After obtaining the number of ZC points for each of the Reference, South antenna 1 and West antenna 1 signals, the minimum values of the ZC points were computed for the Reference antenna, South antenna 1 and West antenna 1 signals. An excerpt of the code is shown below.

```
mMax1=min(mref,m2); % Finding the minimum value for mref and m2
mMax2=min(mref,m3); % Finding the minimum value for mref and m2
```

The code establishes that the array lengths are the same before subtraction and that the numbers of points match in order to calculate the time difference between the Reference and South antenna 1 and West antenna 1 signals.

The time difference between the Reference and South antenna 1 (dt_S1) signals and between the Reference and West antenna 1 (dt_W1) signals, were calculated, as shown in Figure 5-8. An excerpt of the code which calculates the time difference is shown below.

```
dt_S1=t0_S1(1:mMax1)-t0_ref(1:mMax1);% The time difference between the
South antenna 1 signal and the Reference signal
dt_W1=t0_W1(1:mMax2)-t0_ref(1:mMax2); % The time difference between the
West antenna 1 signal and the Reference signal
```

The mean of the time differences between the Reference and South antenna 1 signals and between the Reference and West antenna 1 signals were calculated as follows.

```
dt_S1_mean=mean(dt_S1); % The mean of the time difference, average
dt_W1_mean=mean(dt_W1); % The mean of the time difference, average
```

The mean value of the time differences between matching zero crossings was then used to calculate the phase differences, as shown in the excerpt of the code below.

```
chi_S1=(2*pi*fb*dt_S1_mean); %The phase difference between the South
antenna 1 and the Reference signal
chi_W1=(2*pi*fb*dt_W1_mean); %The phase difference between the West antenna
1 and the Reference signal
```

The azimuth and elevation angles were then calculated from the phase differences, using Equations 4.28 through 4.30. This process was repeated for a number of 1 s time series, giving a spread in the estimated elevation and azimuth angles. The results of the spread are discussed below.

5.2.2 Results

In order to further analyse the azimuth and elevation errors in the ZC algorithm, estimates of the azimuth and elevation errors associated with a combination of azimuth and elevation angles were evaluated. The results presented are for the azimuth of 120˚ and elevation of 75˚. Figure 5-10 shows the SD of azimuth and elevation errors when varying the SNR levels in steps of 5 dB, from −10 dB to 50 dB. Each SNR level is associated with an SD of the azimuth and elevation errors.

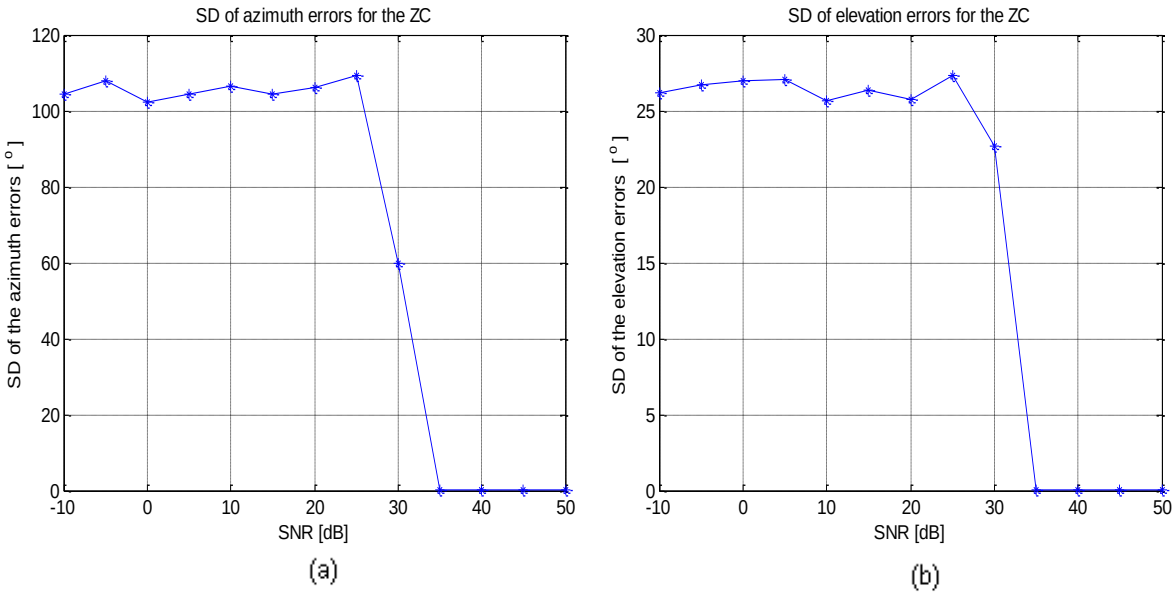

Figure 5-10: Performance of the ZC algorithm for the SD of (a) azimuth and (b) elevation errors versus SNR for a particular azimuth angle of 120˚ and elevation angle of 75˚. The SD of the azimuth and elevation errors was determined after 500 Monte Carlo simulations. The duration of the realisation of the signal was 1 s, and the three baseband signals from the three antennas were sampled at 22 ks/s. The resulting SD of azimuth and elevation errors has some ripple in the range up to 35 dB due to the finite number of runs that were used for the Monte Carlo simulation and the large errors in the ZC results for SNR below 35 dB.

In real world conditions, the realistic SNR for the baseband of the HF DF signals is estimated to be about 10 dB for 150 mW transmitter power on the 1U satellite (Visser, 2009).

Figure 5-10 shows that as the SNR decreases, the SD of the azimuth and elevation errors increases. It is reasonable that the SD of the azimuth and elevation errors would increase as the SNR decreases, since the noise level increases at low SNR levels. Noise causes the estimated azimuth and elevation angles to change their true values. After analysing the SD of the azimuth and elevation errors for a particular combination of azimuth and elevation angles, the size/ magnitude and distribution of the errors was investigated. Histograms were used to illustrate the error distribution. A Gaussian curve was fitted to the histogram to estimate the SD of the error distribution of the particular combination of azimuth and elevation angles. Figure 5-11 shows the histogram and Gaussian distribution fit. Note that the SD of zero error corresponds to the azimuth of 120˚ and elevation of 75˚. From Figure 5-11, an estimate of the SD of the azimuth and elevation errors were obtained. Figure 5-10 shows that above 35 dB, the SD of the azimuth and elevation errors approaches 0˚. However, considering the real world the ZC algorithm perform poorly at 10 dB, the SD of the azimuth and elevation errors increases by 105˚ and 26˚ respectively.

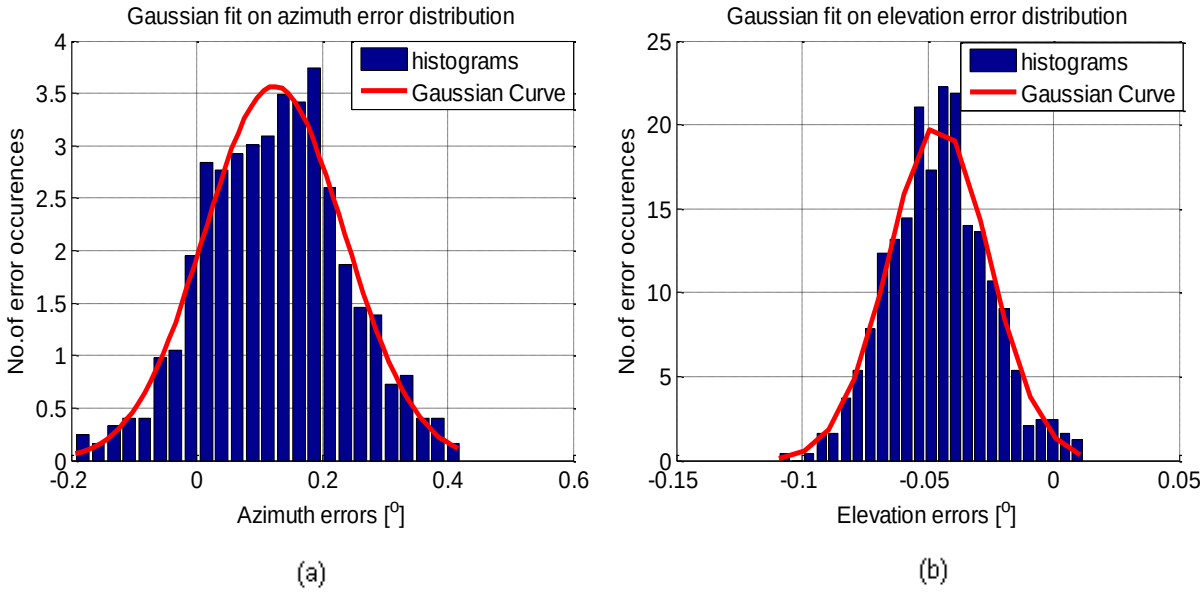

Figure 5-11: Normalised Gaussian curve fit on the normalised histograms of the distribution of (a) azimuth errors with an estimated SD of 0.11˚ and (b) elevation errors with an estimated SD of 0.02˚. The duration of the realisation of the simulated baseband signals was 1 s sampled at 22 ks/s. The SD of the azimuth and elevation errors was determined after 500 Monte Carlo simulations. This was for a good SNR of 35 dB, when the SD of azimuth and elevation errors approaches 0˚

Figure 5-11 clearly shows that the azimuth and elevation errors follow an approximated Gaussian distributed. The results presented from Figures 5-10 to 5-11 were for a particular combination of azimuth and elevation angles. The following evaluation of the distribution of

the SD of the azimuth and elevation errors is for a range of azimuth and elevation values. The SNRs were 40 dB and 0 dB. The distribution covers all the azimuth angles (0˚ to 360˚) in steps of 18˚ and all elevation angles (0˚ to 90˚) in steps of 9˚. The results are illustrated by means of SD error maps. The SD maps demonstrate the distribution of the SD of the azimuth and elevation errors for all combination sets of angles for a single SNR level. Each block on the SD error map represents the SD of the errors resulting from a particular azimuth and elevation combination. Figure 5-12 depicts the SD error maps for a good SNR of 40 dB and low SNR of 0 dB.

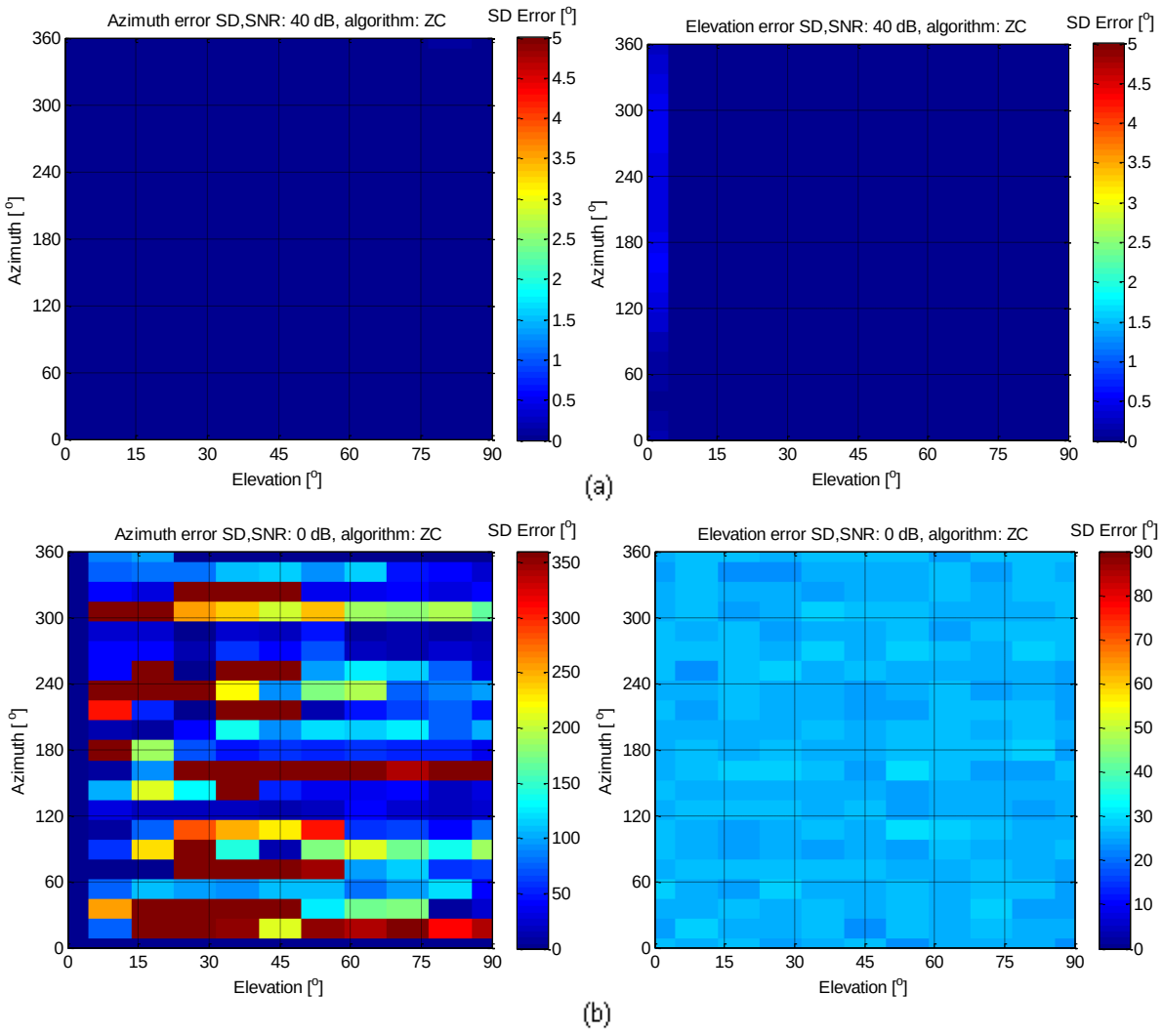

Figure 5-12: SD of azimuth and elevation error distribution for all azimuth and elevation angle combinations for the ZC algorithm (a) SNR = 40 dB and (b) SNR = 0 dB. The duration of the signals is 1 s sampled at 22 ks/s. The SD of azimuth and elevation errors was determined after 100 Monte Carlo simulations. The lower limit of SNR was chosen at a level where either the azimuth or elevation errors became unacceptably large.

The numbers of runs in the Monte Carlo simulation were reduced when demonstrating the distribution of the SD of azimuth and elevation errors for all combination sets of angles for a single SNR level. This was performed because some of the simulations will take longer than

1 day to execute. For a good SNR of 40 dB, the ZC estimated the azimuth and elevation angles correctly, with most SDs of error below 1˚. This is to be expected, because the noise level decreases when the SNR increases. Likewise, when the SNR decreases, the estimation ability of the ZC algorithm weakens, since the noise level increases. This leads to multiple incorrect ZC points, resulting in the wrong estimation of the time differences between the signals. The phase differences are then estimated incorrectly, leading to incorrect estimation of the azimuth and elevation angles. The SD of the azimuth errors increases for most combinations of azimuth and elevation angles. For poor SNR most of the combinations of azimuth and elevation angles are estimated incorrectly, leading to large errors in the estimation of the azimuth and elevation angles. The SD of the elevation errors are below 35˚ for most combinations of angles. The SD of azimuth errors are closer to 360˚ for most combinations of azimuth and elevation angles. The ZC algorithm breaks down when the SNR level decreases below 35 dB. The ZC algorithm starts estimating incorrect azimuth and elevation angles for SNRs below 35 dB. At the realistic SNR level of 10 dB, the ZC algorithm performs poorly. When considering a specific azimuth of 120˚ and elevation of 75˚, the SD of azimuth and elevation errors increases by 105˚ and 26˚ respectively. Most of the combinations of azimuth and elevation angles are estimated incorrectly, resulting in large errors in the estimation of the DOA of the beacon transmission from the CubeSat in real world conditions.

5.3 Fast Fourier Transform (FFT) algorithm

The Fourier transform is a tool that is used to convert a signal in the time domain to the frequency domain (spectrum).

The advantage of the Fourier transform in signals analysis is that it is a simple way of revealing the spectral structures that are used to characterise the signal (Smith, 1997:519). All the samples of the signal are used for the estimation of the spectrum, thus averaging out the noise in any particular part of the time series. Equations 5.1 and 5.2 represent the synthesis equation for the inverse Fourier transform and the analysis equation for the Fourier transform respectively (Roberts & Mullis, 1987:101).

$$f[n] = \frac{1}{2\pi} \int_{-\pi}^{\pi} F(\omega).e^{i\omega n} d\omega. \qquad 5.1$$

$$F(\omega) = \sum_{n=-\infty}^{\infty} f[n].e^{-i\omega n} \qquad 5.2$$

The FFT is used to detect the phase difference between signals acquired simultaneously. The phase difference between signals was computed from both the real and imaginary part

of the Fourier transform. The Fourier transform returns a two-sided spectrum in terms of real and imaginary parts, which can be converted to polar form in order to obtain the magnitude and phase. The magnitude is the square root of the sum of the real (cosine) part squared and the imaginary (sine) part squared (Smith, 1997:227) The magnitude of the FFT is a real number that represents the total signal amplitude in each frequency bin independent of the phase. The amplitude spectrum is related to the real and imaginary parts of the spectrum by Equation 5.3

$$\text{Mag} = \sqrt{\left((\text{real})^2 + (\text{imag})^2\right)}. \qquad 5.3$$

The phase of the FFT is calculated by taking the arc tangent of the ratio of the imaginary and real parts of each frequency component, using Equation 5.4. The phase difference is then obtained by subtracting the phase of the S1 and W1 signals from the phase of the Reference signal at the carrier frequency.

$$\text{Phase} = \tan^{-1}\left[\frac{\text{imag}}{\text{real}}\right]. \qquad 5.4$$

5.3.1 Phase difference estimation using the FFT algorithm

The signal frequencies are detected by applying the FFT to the simulated baseband signals for the Reference antenna, South antenna 1 and West antenna 1. The phases of the Reference antenna, South antenna 1 and West antenna 1 are estimated around the frequencies that are detected by the FFT. In this case, the phases were detected at the baseband frequency of 1 kHz for each of the Reference, South antenna 1 and West antenna 1 simulated baseband signals. The phase differences were then calculated from the phases detected at the baseband frequency of 1 kHz.

The excerpt of the code shows how the FFT for each of the Reference, South antenna 1 and West antenna 1 simulated baseband signals were calculated by using the MATLAB built-in function fft.

```
REF=1/numel(ref)*fft(ref);      %Taking FFT of the reference signal [V]
S1_Antenna=1/numel(S1)*fft(S1);%Taking FFT of the South antenna signal [V]
W1_Antenna=1/numel(W1)*fft(W1);%Taking FFT of the West antenna signal [V]
```

After applying the FFT to each of the Reference, South antenna 1 and West antenna 1, the magnitudes and the phases of the FFT of the three simulated baseband signals were calculated. The magnitudes and phases were detected as shown in the excerpt of the code below.

```
R_mag = abs(REF);          %Magnitude of the FFT of the Reference signal [V]
S1_mag = abs(S1_Antenna); %Magnitude of the South antenna 1 signal [V]
W1_mag = abs(W1_Antenna); %Magnitude of the West antenna 1 signal [V]

REF_pha = 180/pi*unwrap(angle(REF)); %Phase angle of the FFT of Reference
signal [deg]
S1_pha = 180/pi*unwrap(angle(S1_Antenna)); %Phase angle of the FFT of the
South antenna 1 signal [deg]
W1_pha = 180/pi*unwrap(angle(W1_Antenna)); %Phase angle of the FFT of the
West antenna 1 signal [deg]
```

The magnitudes and the phases for the FFT between the Reference and South antenna 1, and between the Reference and West antenna 1 signals were plotted on the magnitude and phase spectrums, as depicted in Figures 5-13 and 5-14.

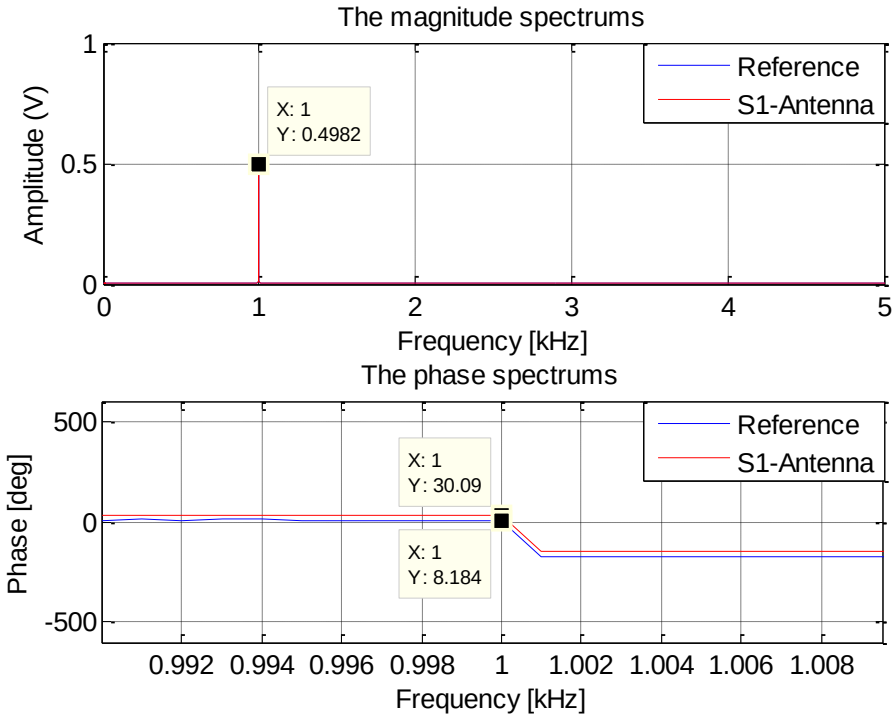

Figure 5-13: The magnitude and zoomed version of the phase spectrum for the Reference and South antenna 1 signal for a specific azimuth angle of 120° and elevation of 75°. The phase spectrum shows the phase angle at 1 kHz for a good SNR of 40 dB. The three simulated baseband signals were sampled at 22 ks/s and the duration of the realisation of the signal of was 1 s

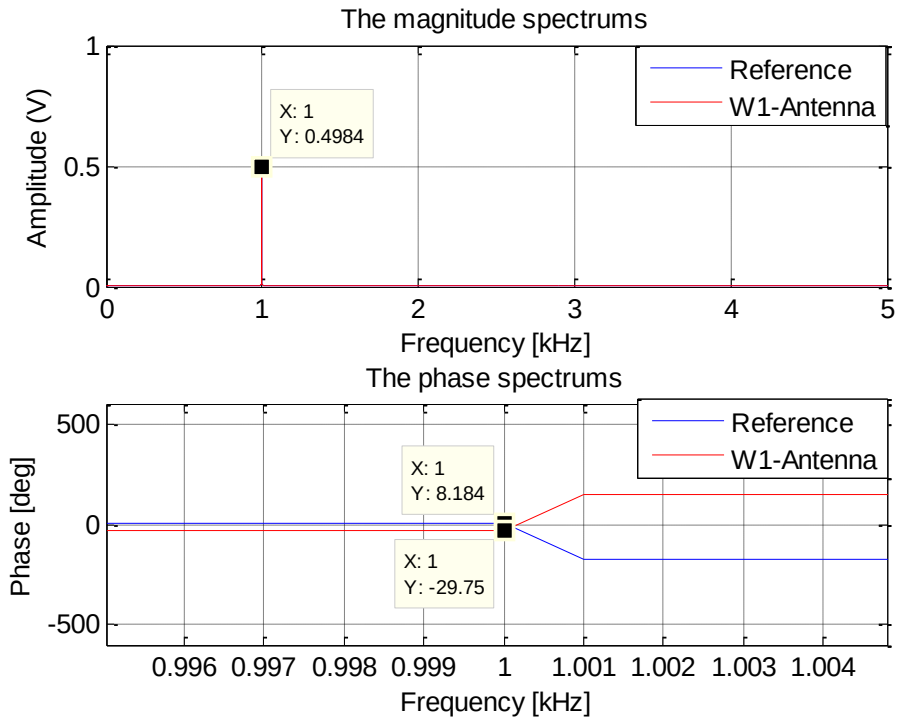

Figure 5-14: The magnitude and zoomed version of the phase spectrum for the Reference and West antenna 1 signal for an azimuth angle of 120° and elevation of 75°. The phase spectrum shows the phase at 1 kHz for a good SNR of 40 dB. The simulated baseband signals are sampled at 22 ks/s and the total duration of the signals was 1 s

In the simulation studies windowing was not applied before the FFT was taken. Windowing is used primarily to minimise the effects of leakage, which is a computational issue related to the application of the FFT algorithm. Simulation involving cases with and without windowing indicated that at SNR of 10 dB the effects of leakage did not affect the phase shift at the estimated carrier frequency.

The code below illustrates how the two phase differences were calculated. In the code chi_S1 _est represents the estimated phase difference between the Reference and South antenna 1 ($\Delta\psi_{S1}$) and chi_W1_est represents the estimated phase difference between the Reference and West antenna 1 ($\Delta\psi_{W1}$).

```
chi_S1_est =-(S1_pha_deg-REF_deg);%The phase difference between the
Reference antenna and the South antenna 1
chi_W1_est =-(W1_pha_deg-REF_deg);%The phase difference between the
Reference antenna and the West antenna 1
```

The estimated phase difference between the Reference and the South antenna 1 signal ($\Delta\psi_{S1}$) and between the Reference and the West antenna signal ($\Delta\psi_{W1}$) were calculated from the phase angle detected by the South antenna 1 and West antenna 1 signals relative to the Reference antenna signal, using Equations 5.5 and 5.6 respectively. The azimuth and

elevation angles were then derived from the two phase differences $\Delta\psi_{S1}$ and $\Delta\psi_{W1}$ using Equations 4.28 through 4.30.

$$\begin{aligned}\Delta\psi_{S1} &= \text{Phase angle of S1 - antenna} - \text{Phase angle of the Reference antenna} \\ &= -(30.09^{\circ} - 8.184^{\circ}) \\ &= -21.90^{\circ}\end{aligned} \qquad 5.5$$

$$\begin{aligned}\Delta\psi_{W1} &= \text{Phase angle of W1 - antenna} - \text{Phase angle of the Reference antenna} \\ &= -(-29.75^{\circ} - 8.184^{\circ}) \\ &= 37.91^{\circ}\end{aligned} \qquad 5.6$$

The process of applying the FFT to the simulated baseband signals was repeated for a number of 1s time series, giving a spread in the estimation of the azimuth and elevation. The results are discussed in the next section.

5.3.2 Results

To analyse the estimation of the SD of the azimuth and elevation errors when using the FFT algorithm, an azimuth of 120˚ and elevation of 75˚ was selected and the SNR levels varied in steps of 5 dB from – 10 dB to 50 dB. Each SNR level is associated with a specific SD of the azimuth and elevation errors.

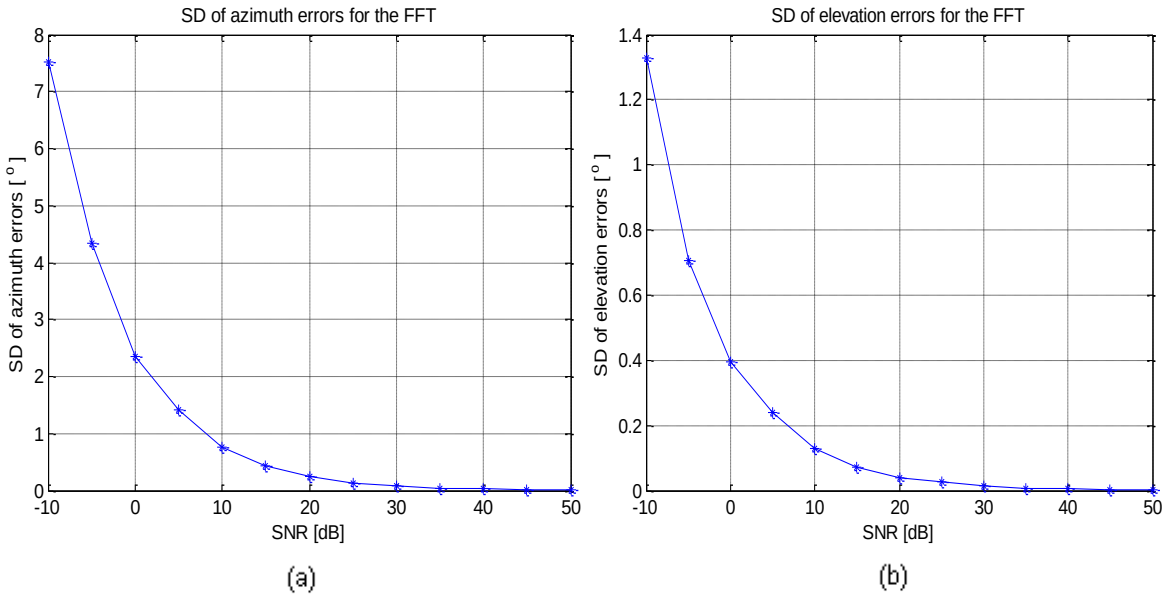

Figure 5-15: Performance of the FFT algorithm for the SD of (a) azimuth and (b) elevation errors versus SNR for a particular azimuth angle of 120˚ and elevation angle of 75˚. The SD of azimuth and elevation errors was determined after 500 Monte Carlo simulations. The duration of the realisation of the signal is 1 s, and the three baseband signals from the three antennas were sampled at 22 ks/s.

When the SNR decreases, the SD of the azimuth and elevation errors increases due to the increased level of noise. An analysis of the distribution of the azimuth and elevation estimation on errors for a single SNR was performed. Histograms were used to illustrate how the errors are distributed. A Gaussian curve was fitted to the histogram to determine the error distribution. Figure 5-16 shows a histogram of the number of occurrences of error versus the azimuth and elevation errors. Figure 5-16 also shows the Gaussian fit to the histograms to estimate the SD of the azimuth and elevation errors. An investigation was done using an SNR of – 10 dB. At this SNR the SD of the azimuth and elevation angles begins to increase as observed in Figure 5-15.

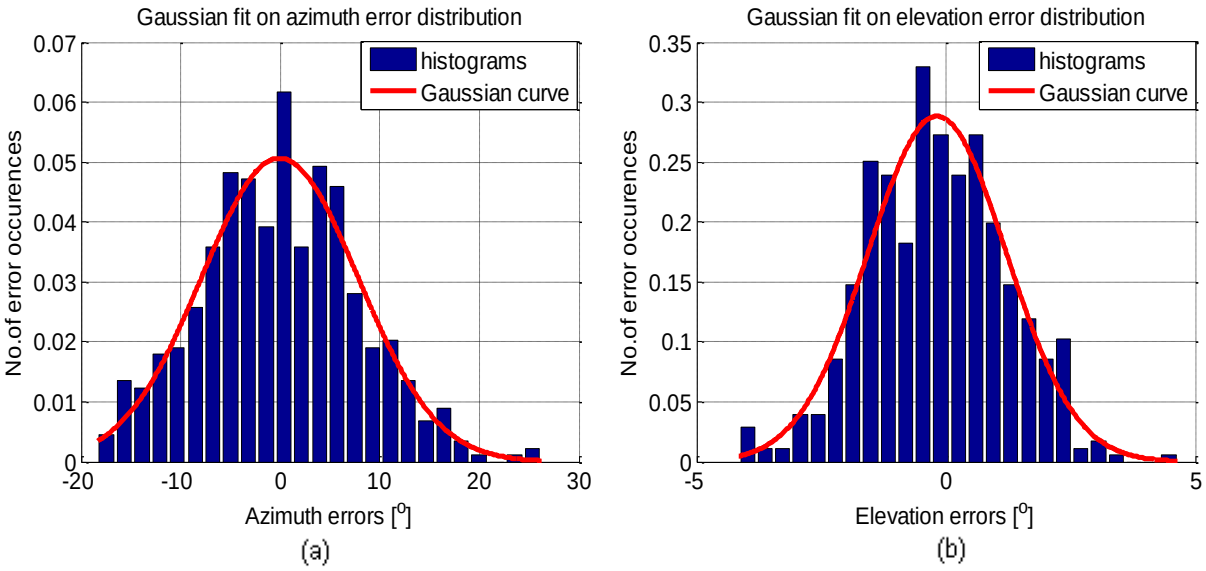

Figure 5-16: Normalised Gaussian curve fit on the normalised histograms of the error distribution for (a) azimuth errors with an estimated SD of 7.45˚ and (b) elevation errors with an estimated SD of 1.22˚. The duration of the realisation of the simulated base band signals was 1 s sampled at 22 ks/s. The SD of the azimuth and elevation errors was determined after 500 Monte Carlo simulations. This was for a poor SNR of – 10 dB, where the SD of azimuth and elevation errors begins to increase

Figure 5-16 shows clearly that the azimuth and elevation errors have a Gaussian distribution. Most of the errors are distributed around the mean of 0˚. The results obtained with an SNR of – 10 dB correlate well with the results shown in Figure 5-15, where the SNR varies. An SD of 7.45˚ for the azimuth errors and 1.22˚ for the elevation errors were obtained with an SNR of – 10 dB. The author continued to investigate the distribution of the SD of the azimuth and elevation errors for all the azimuth angles (0˚ to 360˚) in steps of 18˚ and elevation angles (0˚ to 90˚) in steps of 9˚, using SD error maps. The SD error maps illustrate the distribution of the SD of the azimuth and elevation errors for all combination sets of angles for a single SNR level. Each block on the SD error map represents the SD of the errors resulting from a particular azimuth and elevation combination. With an azimuth angle of 120˚ and elevation

angle of 75˚ the FFT algorithm estimated the DOA correctly with minimum errors even at low SNR levels (see Figure 5-15). The distribution of the SD of azimuth and elevation errors was performed with both a good SNR of 40 dB and as poor SNR of – 20 dB. In the latter case the FFT started to estimate the DOA with large errors. Figure 5-17 depicts the SD error maps for a good SNR of 40 dB and a poor SNR of – 20 dB.

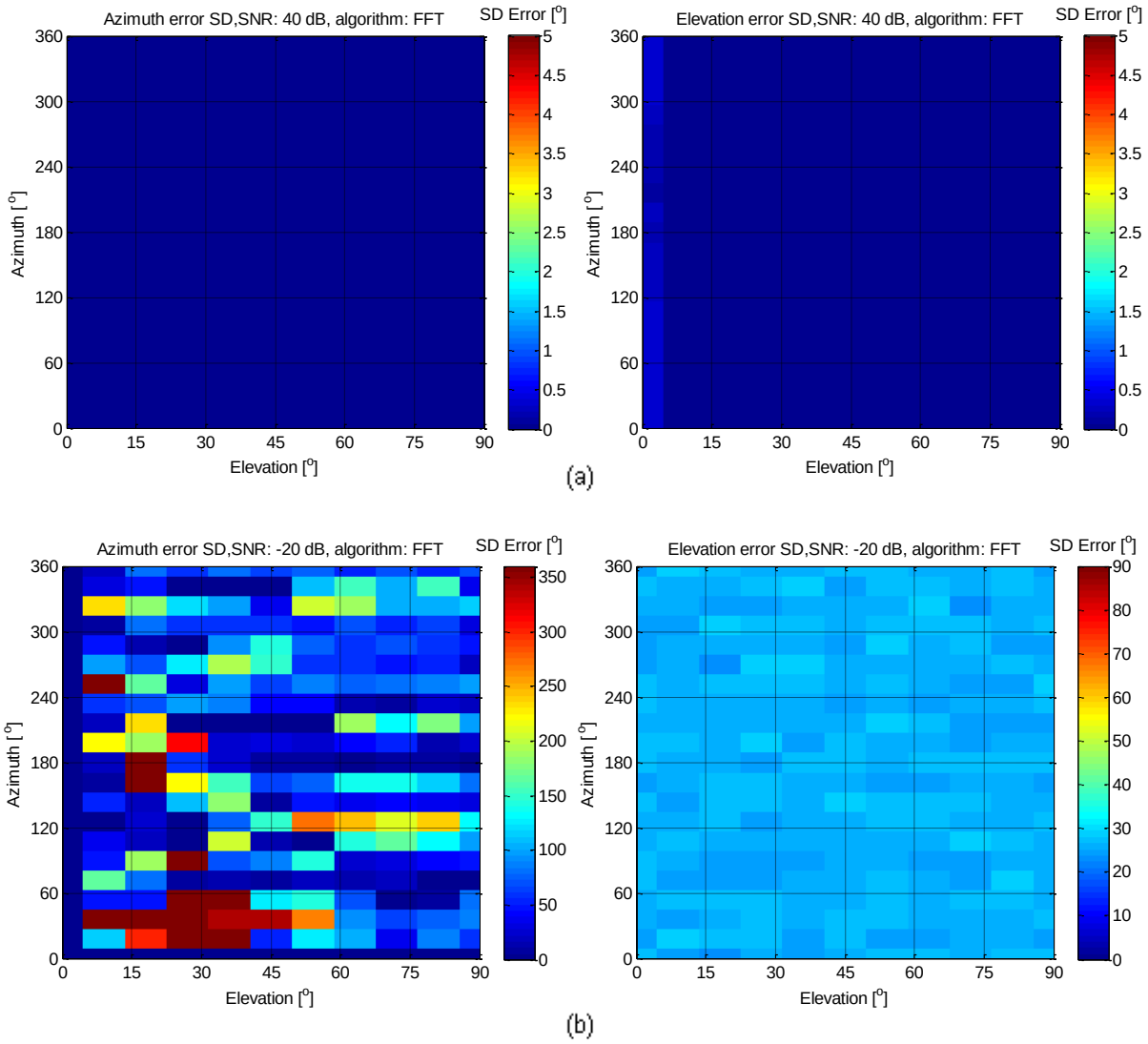

Figure 5-17: SD of azimuth and elevation error distribution for all azimuth and elevation angles for the FFT algorithm (a) SNR = 40 dB and (b) SNR = −20 dB. The duration of the signal is 1 s sampled at 22 ks/s. The SD of azimuth and elevation errors was determined after 100 Monte Carlo simulations. The lower limit of SNR was chosen at a level where either the azimuth or elevation errors became unacceptably large.

When the SNR is 40 dB the FFT algorithm estimates most combination sets of azimuth and elevation angles correctly, with an SD of the errors less than 1˚.This is to be expected, because as the SNR increases, the noise level decreases. When the SNR decreases to – 20 dB, the FFT algorithm breaks down for most combination sets of angles in the estimation of the azimuth and elevation angles. For an SNR of – 20 dB, large SD of azimuth errors were

experienced at elevation angles between 1˚ and 85˚ for all azimuth angles. In this region, it is obvious that the accuracy of FFT estimation deteriorates. The FFT algorithm estimates the azimuth and elevation angles with minimum errors even at an SNR of – 20 dB for some combinations of azimuth and elevation angles. For a specific azimuth angle of 120˚ and elevation of 75˚, the SD of azimuth and elevation errors is 0.8˚ and 0.12˚, which are still less than 1˚ at a realistic SNR of 10 dB. This algorithm will be best to compute the DOA of the beacon signal from the CubeSat in real world conditions.

5.4 Cross Correlation (CC)

CC is one of the signal processing techniques that is commonly used to find time delays between two received signals. Many other signal processing techniques are based on this technique. CC measures the degree to which the signals are correlated. The CC between two signals is the matching of the one signal and the time delay version of another signal. The time delay is obtained from the time lag that maximises the CC function (Paulose *et al*., 2013:934). The time lag that maximises the CC was used to estimate the phase difference between the signals.

5.4.1 Phase difference estimation using the CC algorithm

The CC between the Reference and the South antenna 1 signals, and between the Reference and the West antenna 1 signals are defined by Equation 5.7 in a discrete time representation.

$$R_{brefS_1}[\tau 1] = \sum_{n=-\infty}^{\infty} b_{ref}[n] S_1^*[n-\tau 1]$$
$$R_{brefW_1}[\tau 2] = \sum_{n=-\infty}^{\infty} b_{ref}[n] W_1^*[n-\tau 2] \qquad 5.7$$

Here $\tau 1$ and $\tau 2$ represent the delay parameters which are related to the phase differences $\Delta\psi_{S1}$ and $\Delta\psi_{W1}$ between the Reference antenna signal and the other two signals from the South and West antennas. The CC represents the overlapping area between the signals, and the delay parameter determines the maximum possible correlation between two signals. The code below illustrates how the simulated baseband signals from the Reference antenna, South antenna 1 and West antenna 1 were correlated. It also shows how the two estimated phase difference were obtained at the maximum lags.

```
[xS1,lag_S1] =xcorr(ref_hsr,S1_hsr,Nshift,'coeff'); %Computing the cross
correlation between the interpolated Reference antenna signal and the South
antenna 1 signal
[xW1,lag_W1] =xcorr(ref_hsr,W1_hsr,Nshift,'coeff'); %Computing the cross
correlation between the interpolated Reference antenna signal and the West
antenna 1 signal
```

```
[max_xS1,imax]=max(xS1); %Find the index of the highest peak value of xS1
chi_S1_est1=-lag_S1(imax)*d_psi;%S1-antenna phase difference relative to
Reference [deg]
[max_xW1,imax]=max(xW1); %Find the index of the highest peak value of xS1
chi_W1_est1=-lag_W1(imax)*d_psi;%W1-antenna phase difference relative to
Reference [deg]
```

The maximum time lags defined by lag_S1 and lag_W1 represent the two estimated phase differences $\Delta\psi_{S1}$ (chi S1) and $\Delta\psi_{W1}$ (chi W1). Figure 5-18 depicts the maximum time lags that represent the two phase differences $\Delta\psi_{S1}$ (chi S1) and $\Delta\psi_{W1}$ (chi W1). The phase differences $\Delta\psi_{S1}$ and $\Delta\psi_{W1}$ were then used to calculate the azimuth and elevation angles, using Equations 4.28 through 4.30.

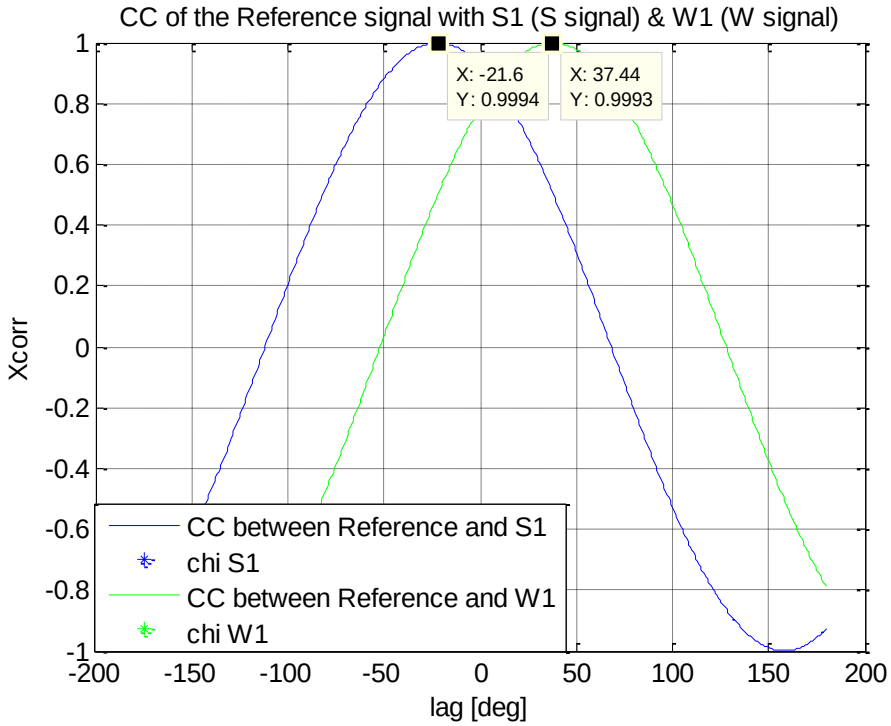

Figure 5-18: An illustration of the cross correlation between the Reference and the South antenna 1 signals, and between the Reference and the West antenna 1 signals for an azimuth angle of 120° and elevation angle of 75°. The simulated baseband signals were sampled at 22 ks/s with the total duration of the signal of 1 s. A phase difference of – 21.6° was obtained between the cross correlation of the Reference and South antenna 1. A phase difference of 37.44° was obtained between the cross correlation of the Reference and West antenna 1 with maximum amplitude of 1

The cross correlation between the Reference antenna and South antenna 1 and between the Reference antenna and West antenna 1 signal was repeated for a number of 1 s time series. This gives us the spread in the estimation of the elevation and azimuth angles. The results are discussed below.

5.4.2 Results

To illustrate the distribution of the SD of the azimuth and elevation errors by means of the CC algorithm, the first step is to evaluate the azimuth and elevation errors associated with a specific azimuth of 120˚ and elevation of 75˚ with varying SNR levels. The experiment demonstrates the effect of SNR on the performance of the CC algorithm, because each SNR level is associated with a certain SD of the azimuth and elevation errors. Figure 5-19 illustrates the effect of SNR on the performance of the CC algorithm for a selected azimuth of 120˚ and elevation of 75˚.

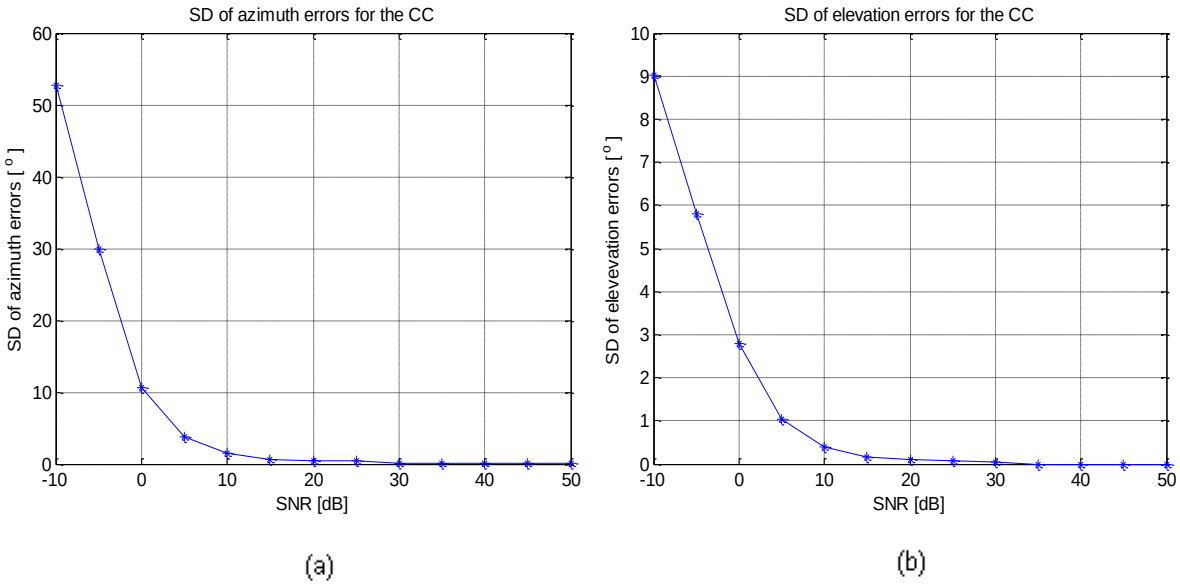

Figure 5-19: Performance of the CC algorithm for the SD of (a) azimuth and (b) elevation errors versus SNR for an azimuth angle of 120˚ and elevation angle of 75˚. The SD of azimuth and elevation errors was determined after 500 Monte Carlo simulations. The duration of the realisation of the signal is 1 s, and the simulated baseband signals are sampled at 22 ks/s

It is to be expected that the SD of the azimuth and elevation errors would decrease as the SNR increases (see Figure 5-19). It can be seen that the CC algorithm estimates the azimuth angle with large errors when the SNR starts decreasing from 0 dB, however, the elevation estimates give small errors even at an SNR of 0 dB. The author continued to investigate the error distribution by means of histograms for a single SNR of 0 dB. When the SNR = 0 dB, the SD of the errors of the estimated azimuth and elevation begins to rise. A Gaussian curve was fitted to the histograms of the errors, to evaluate error distribution.

Figure 5-20 shows the number of error occurrences versus the azimuth and elevation errors using histograms, with a Gaussian curve fit on the histograms to estimate the SD of the azimuth and elevation errors.

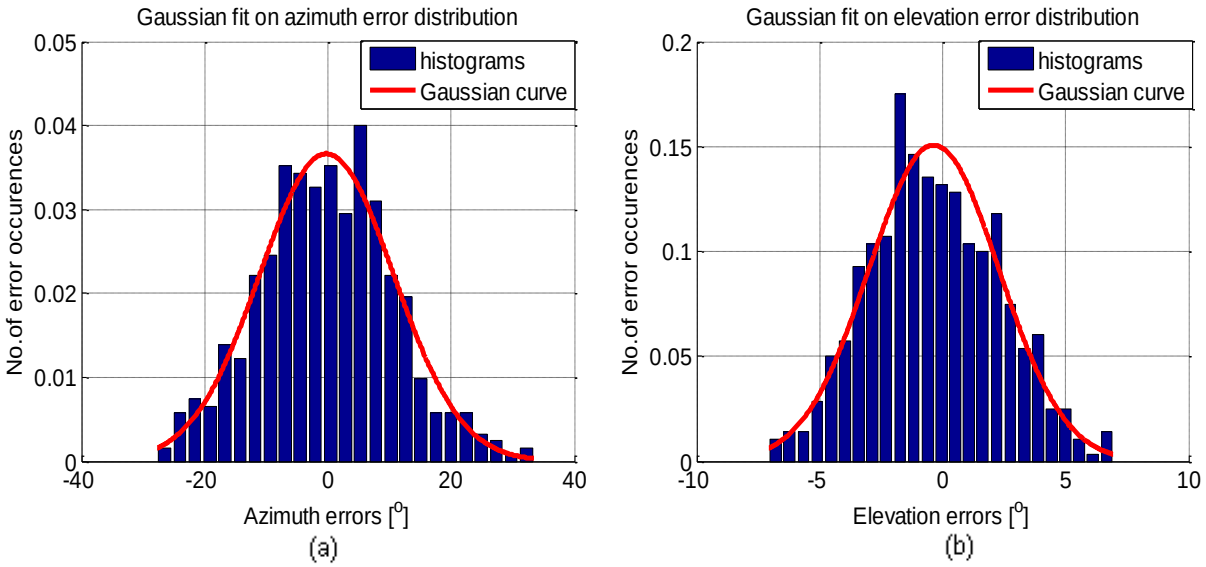

Figure 5-20: Normalised Gaussian curve fit on the normalised histograms of the error distribution of (a) azimuth errors with an estimated SD of 14.25˚ and (b) elevation errors with an estimated SD of 2.77˚. The duration of the realisation of the simulated base band signals was 1 s sampled at 22 ks/s. The SD of the azimuth and elevation errors was determined after 500 Monte Carlo simulations. This was for a poor SNR of 0 dB, when the SD of azimuth and elevation errors begin to increase

Figure 5-20 proves that most of the azimuth and elevation errors are distributed around the mean of 0˚. This shows that the azimuth and elevation errors follow a Gaussian distribution. The error distribution for a single SNR of 0 dB correlates well with the results obtained for the SD of the azimuth and elevation angles versus a range of SNR levels (see Figure 5-19). An SD of 14.25˚ for the azimuth errors and 2.77˚ for the elevation errors was obtained with a single SNR of 0 dB for an azimuth of 120˚ and elevation of 75˚.

The author continued to investigate the distribution of the SDs of the azimuth and elevation error for all azimuth angles (0˚ to 360˚) in steps of 18˚ and elevation angles (0˚ to 90˚) in steps of 9˚ by means of SD error maps. Figure 5-21 shows the SD error maps for a good SNR of 40 dB and a poor SNR of – 10 dB.

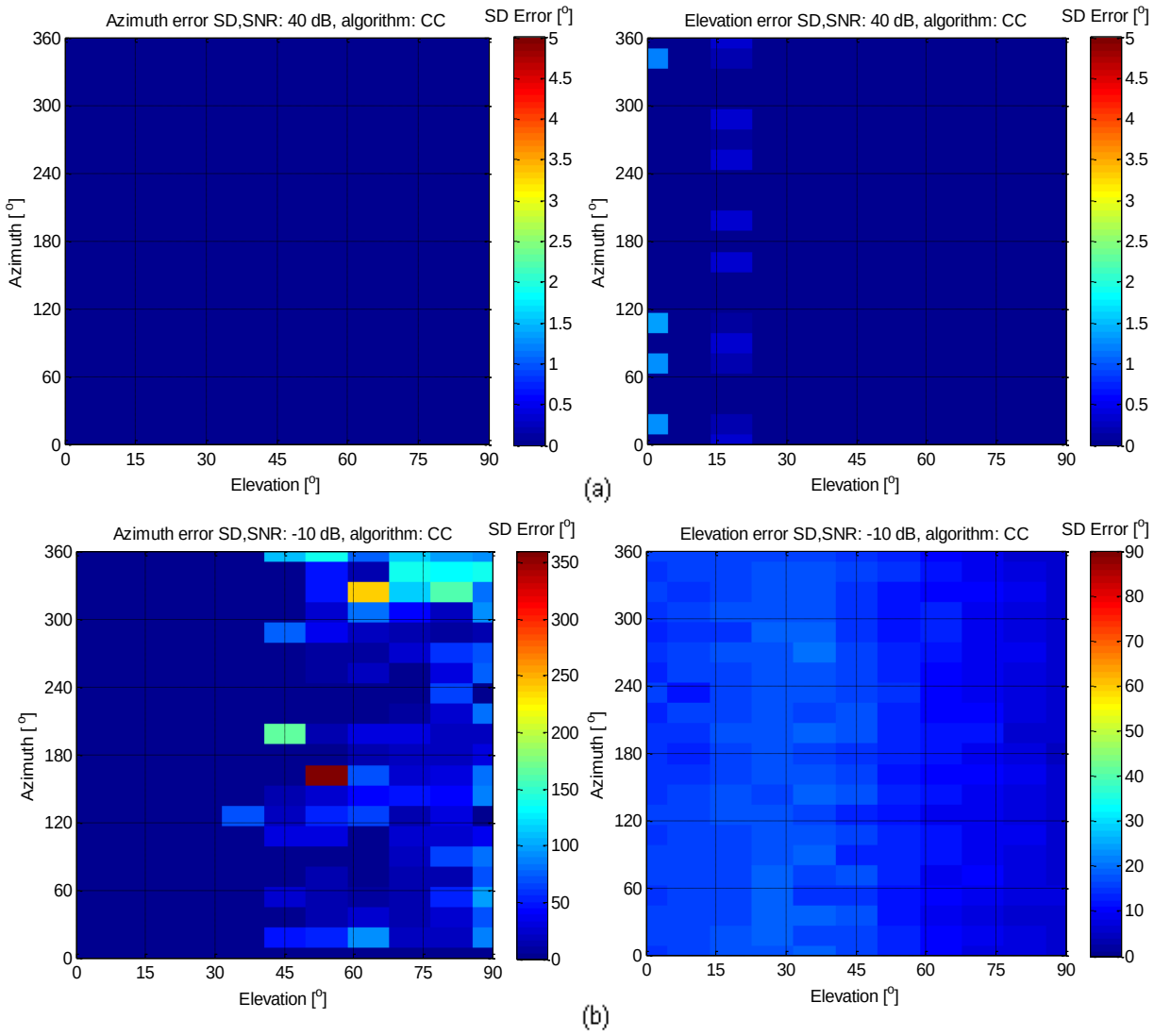

Figure 5-21: The SD of azimuth and elevation error distribution for all azimuth and elevation angles for the CC algorithm (a) SNR = 40 dB and (b) SNR = −10 dB. The total duration of the signal is 1 s sampled at 22 ks/s. The SD of azimuth and elevation errors was determined after 100 Monte Carlo simulations. The lower limit of SNR was chosen at a level where either the azimuth or elevation errors became unacceptably large.

With a good SNR of 40 dB, the CC algorithm estimates the azimuth and elevation angles correctly with most of the SD errors below 1˚, although some elevation errors occurred at low elevation angles. The expectation is that with a good SNR the errors will be small, due to the low level of noise. However, when the SNR decreases to – 10 dB, there are large azimuth errors when elevation angles are between 45˚ and 90˚. In this region, the estimation accuracy of the CC algorithm is poorer in comparison with the other regions. Large errors were detected at elevations between 0˚ to about 75˚. The estimation accuracy is lower in region of elevations between 0˚ to about 75˚ than in the other regions. The SD of the elevation errors are below 40˚ for most combination sets of azimuth and elevation angles.

The magnitude of the SD of azimuth and elevation errors detected at the realistic SNR of 10 dB is 3˚ and 0.2˚ respectively for a specific azimuth angle of 120˚ and elevation of 75˚.

5.5 Cross Power Spectral Density (CPSD)

The evaluation of the of the CPSD algorithm was done by means of a built-in MATLAB command (cpsd), that evaluates the CPSD of the Reference, South antenna 1 and West antenna 1 signals using the Welch averaged method (Welch, 1967). The CPSD is defined as the distribution of power per unit frequency and is calculated as follows by Equation 5.9

$$Pxy(\omega) = \sum_{m=-\infty}^{\infty} R_{xy}(m)\, e^{-j\omega m}. \qquad 5.9$$

Here $Pxy(\omega)$ denotes the CPSD between signal x and y and R_{xy} is the CC between signal x and y. The CPSD uses CC signals, and it returns a one-sided CPSD for a real signal and two-sided CPSD for the complex signal. The built-in command for the CPSD in MATLAB uses default values, for example, the length of the FFT, the sampling frequency and the window function. Empty matrices [ ] are used to represent the default values. The CPSD is a complex quantity that is made up of the magnitude and phase of the signal. The phase of the signal is the parameter that was used to compute the phase difference between two signals.

5.5.1 Phase difference estimation using CPSD the algorithm

The CPSD of the Reference and the South antenna 1 signals and of the Reference and the West antenna 1 signals was determined as shown in the code below.

```
[PxyRS1,fp1] = cpsd(ref,S1,[],[],[],fs,'twosided');% CPSD of ref and S1,
fp1 represent the frequency vector at which the cpsd is estimated in hertz
[PxyRW1,fp2] = cpsd(ref,W1,[],[],[],fs,'twosided');% CPSD of ref and W1,fp2
represent the frequency vector at which the cpsd is estimated in hertz
PxyRS1_mag = abs(PxyRS1) % Magnitude of the cpsd of ref and S1 [V^2]
PxyRS1_pha = 180/pi*unwrap(angle(PxyRS1));% Phase angle [deg]
PxyRW1_mag = abs(PxyRW1); %Magnitude of the cpsd of ref and W1 [V^2]
PxyRW1_pha = 180/pi*unwrap(angle(PxyRW1));% Phase angle [deg]
```

The CPSD method correlates the Reference signal with the signals from each of the other two antennas. The phase difference is taken as the shift required for maximum correlation. The CPSD uses the Fourier transform of the correlated signals. The phase difference is taken at the frequency at which the CPSD is estimated. The two steps are performed by the built-in command (cpsd) in MATLAB. The FFT calculates the magnitude and the phase of the signals as a function of frequency. The $PxyRS1$ and $PxyRW1$ denotes the CPSD of the Reference signal and the South antenna 1 signal, and of the Reference signal and the West antenna 1 signal respectively.

The two phase differences $\Delta\psi_{S1}$ (S1_pha0) and $\Delta\psi_{W1}$ (W1_pha0) are detected by getting the phases at the frequency of operation (f0_index). In this case it is the baseband frequency of 1 kHz. The code below shows how the two phase differences were obtained from the CPSD of the Reference antenna signal and the other two simulated baseband signals. The two phase differences $\Delta\psi_{S1}$ and $\Delta\psi_{W1}$ were then used to estimate the azimuth and elevation angles, using Equations 4.28 through 4.30.

```
S1_pha0=PxyRS1_pha(f0_index); %Phase difference between the ref and S1
W1_pha0=PxyRW1_pha(f0_index); %Phase difference between the ref and W1
```

The process of taking the CPSD of the Reference signal and the other two simulated baseband signals was repeated for a number of 1 s time series. Then repeating the process gives the distribution of the estimated elevation and azimuth. The results of the distribution of the SD of the errors are discussed below.

5.5.2 Results

The purpose of this section is to characterise the distribution of the SD of the azimuth and elevation errors by means of the CPSD algorithm. Figure 5-22 shows the effect of SNR on the performance of the CPSD algorithm. An azimuth of 120˚ and elevation of 75˚ was selected to investigate the distribution of the errors associated with that particular DOA and is depicted in Figure 5-22. The SNR levels vary in steps of 5 dB from – 10 dB to 50 dB, where each SNR level is related to a specific SD of the azimuth and elevation errors.

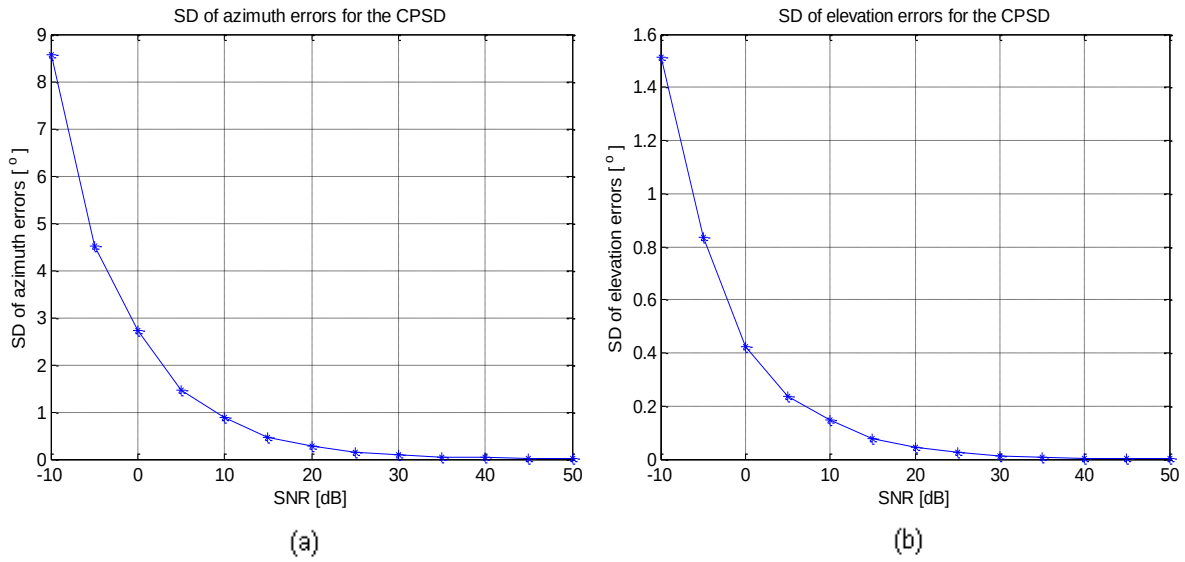

Figure 5-22: Performance of the CPSD algorithm for the SD of (a) azimuth and (b) elevation errors versus SNR for an azimuth angle of 120˚ and elevation angle of 75˚. The SD was determined after 500 Monte Carlo simulations. The duration of the realisation of the signal is 1 s, and the simulated base band signals are sampled at 22 ks/s

It can be seen that the SD of the estimated azimuth and elevation errors decreases as SNR increases. This is to be expected, due to the low level of noise with a good SNR. When the SNR decreases, the SD of the azimuth and elevation errors increases. The author continued to evaluate the distribution of the errors by means of histograms for a single SNR level. Figure 5-22 shows that large SDs of azimuth and elevation errors are experienced at an SNR of – 10 dB. A Gaussian curve was fitted to the histograms to evaluate the error distribution. Figure 5-23 depicts the number of error occurrences versus the azimuth and elevation errors, with a Gaussian curve fit on the histograms to estimate the SD of the azimuth and elevation errors.

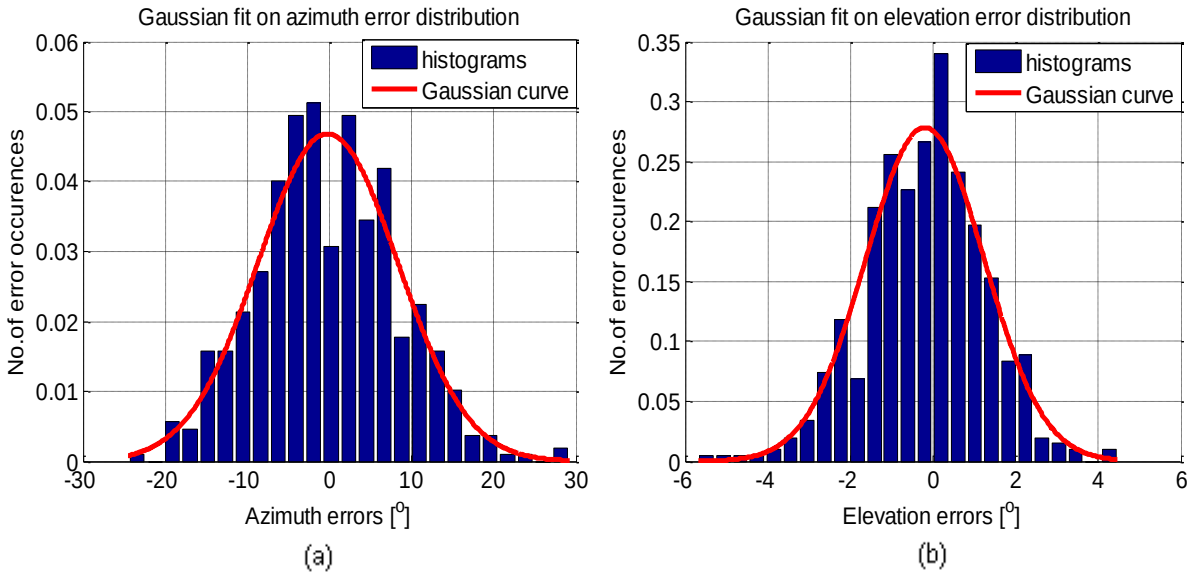

Figure 5-23: Normalised Gaussian curve fit on the normalised histogram of the error distribution for (a) azimuth errors with an estimated SD of 8.62˚ and (b) elevation errors with an estimated SD of 1.46˚. The duration of the realisation of the simulated baseband signals is 1 s sampled at 22 ks/s. The SD of the azimuth and elevation errors was determined after 500 Monte Carlo simulations. This was for a poor SNR of – 10 dB, when the SD of azimuth and elevation errors begin to rise

In Figure 5-23 it can be seen that the azimuth and elevation errors have a Gaussian-shaped distribution. Most of the errors are found close to the mean of 0˚. The results of the distribution of the SD of azimuth and elevation errors obtained for a single SNR of – 10 dB correspond well with the results illustrated in Figure 5-22, where the SNR varies. An SD of 8.62˚ for the azimuth errors and 1.46˚ for the elevation errors were obtained for a single SNR of – 10 dB for an azimuth of 120˚ and elevation of 75˚.

The distribution of the SD of the azimuth and elevation errors for all azimuth angles (0˚ to 360˚) in steps of 18˚ and elevation angles (0˚ to 90˚) in steps of 9˚ is illustrated with SD error maps. Figure 5-24 shows the SD error maps for a good SNR of 40 dB and a poor SNR of – 20 dB.

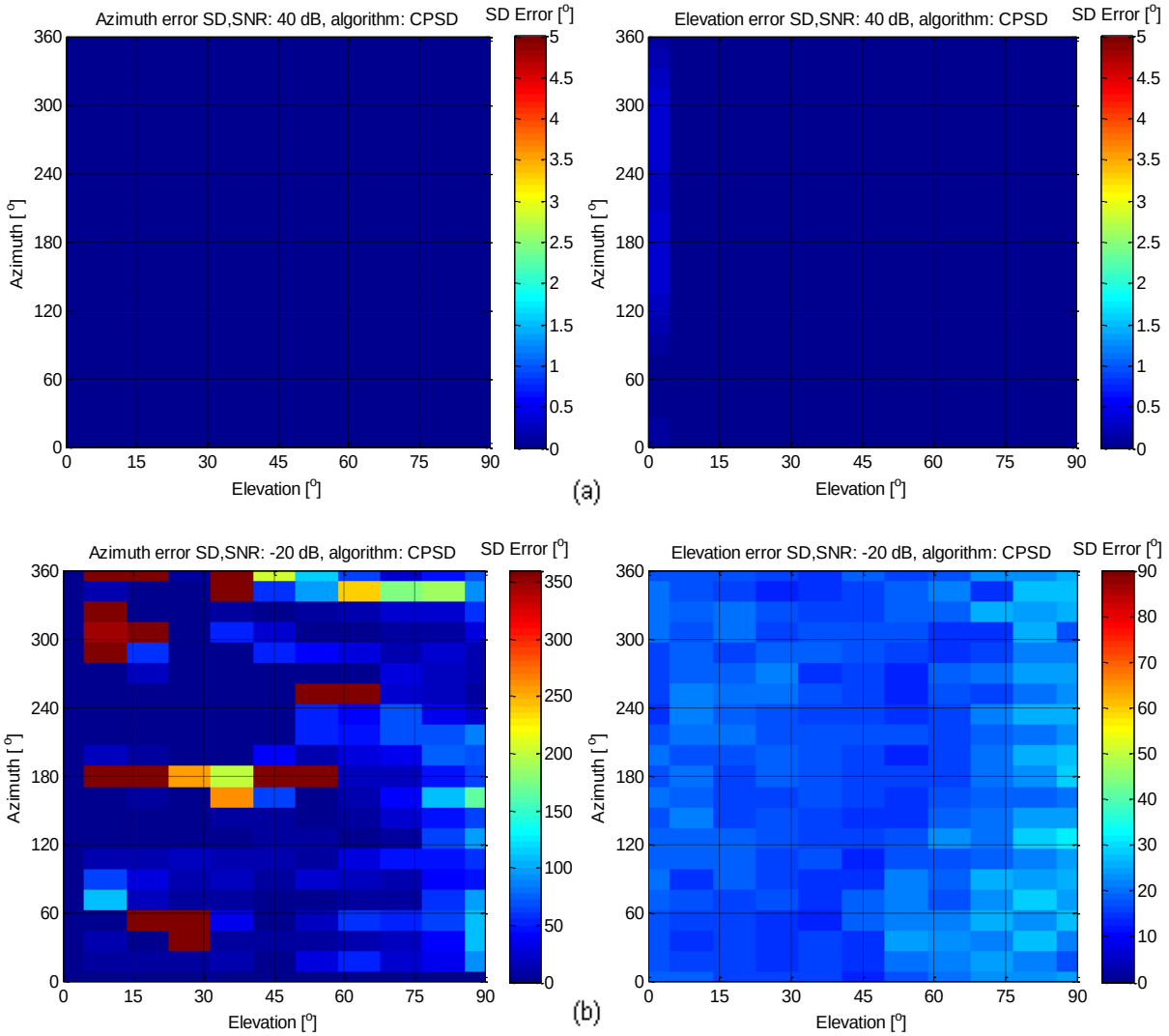

Figure 5-24: The SD of azimuth and elevation error distribution for all azimuth and elevation angles for the CPSD algorithm (a) SNR = 40 dB and (b) SNR = −20 dB. The total duration of the signal is 1 s sampled at 22 ks/s. The SD of azimuth and elevation errors was determined after 100 Monte Carlo simulations. The lower limit of SNR was chosen at a level where either the azimuth or elevation errors became unacceptably large.

With a good SNR of 40 dB, the CPSD algorithm performs significantly better than the ZC and CC algorithms for the estimation of most combination of angles. The SD of the errors is less than 1˚.The SD of the azimuth and elevation errors decreases as the SNR increases. Yet, when the SNR decreases to – 20 dB, the CPSD still estimates the azimuth angles correctly with the minimum errors. However, in some regions the estimation accuracy deteriorates, especially at azimuth angles closer to 180˚, 360˚, 60˚, and near 250˚. The azimuth is estimated incorrectly around those regions. For elevations below 30˚, most of the combination sets of angles are estimated incorrectly. However, some combinations of DOA angles are estimated with a small SD of errors with an SNR of – 20 dB. In real world condition at the SNR of 10 dB, the CPSD estimates the DOA of the beacon signal with a SD of azimuth and elevation errors of 1˚ and 0.13˚ respectively.

5.6 Summary

Four signal processing algorithms for phase difference estimation, from which the DOA can be computed, were discussed and evaluated. The results of the evaluation of each algorithm were presented. The four algorithms perform well when the SNR is high; however, the performance of each algorithm deteriorates when the SNR decreases with increasing noise. However considering the results for real world conditions, the realistic SNR for the baseband of the HF DF signals is estimated to be about 10 dB. Table 5-1 illustrates a summary of magnitude of the SD of azimuth and elevation errors at a realistic SNR level of 10 dB for a specific azimuth angle of 120˚ and elevation of 75˚ for the four algorithms.

Table 5-1: Magnitude of SD of azimuth and elevation errors at SNR of 10 dB for a specific azimuth of 120˚ and elevation of 75˚ angles

Algorithms	SD of azimuth errors [˚]	SD of elevation errors [˚]
FFT	0.8	0.12
CPSD	1	0.13
CC	3	0.2
ZC	105	26

From Table 5-1 it can seen that the CPSD and FFT algorithms outperform the ZC and CC algorithms, with the SD of azimuth and elevation errors less than or equal to 1˚, at a realistic SNR level of 10 dB. The CPSD and FFT perform better than others since the SNR could be reduced to much lower levels before one of the errors became unacceptably large. Large azimuth errors did not always correspond to large elevation errors due to the different non-linear expressions used for the derivation of the errors from the phase differences. However when considering all combination sets of angles, the SD of azimuth and elevation errors were evaluated at high SNR level of 40 dB. These correspond to values that pertain to a very large aperture receiver antenna and a transmitter with much more power than would actually be available for transmission. The point of evaluating high SNR simulations is simply to verify that the algorithms are working properly and that no systematic errors are being introduced in the implementation of the simulation of the algorithms. In chapter six these four algorithms are compared in order to select the best algorithm. The criteria for evaluation of the best algorithm are accuracy and speed.

CHAPTER SIX: COMPARISON AND DISCUSSION OF ALGORITHMS

6.1 Introduction

In this chapter the azimuth errors that occur at elevation angles near 90˚ are highlighted, as well the method for addressing the errors. The algorithms were compared and evaluated for accuracy and speed. The accuracy was determined by the SD of the azimuth and elevation errors. The speed of the algorithm was evaluated in terms of the time required to compute the estimation of the azimuth and elevation angles.

The performance of each algorithm as a function of SNR was investigated for a particular combination of azimuth and elevation angles. When the SNR increased, the accuracy in estimation of azimuth and elevation angles improved. The purpose was to achieve sufficient accuracy in the estimation of the azimuth and elevation angles in the shortest time. The selection of the best algorithm is discussed in this chapter.

6.2 Errors in the estimation of azimuth angles near vertical (90˚)

Large errors were found in the azimuth estimation when the associated elevation angle is near vertical (90˚) or close to the horizon (0˚). When the elevation angle is close to 90˚, the signals reaches all three antennas at approximately the same time, hence, the time delay is minimal. The phase differences are very small, and the elevation angle estimation has large errors. This problem also encountered by other researchers (Liu & Mendel, 1998). Liang (2009) proposed a new cumulant-based algorithm that addresses the estimation failure problem when elevation angles are between 70˚ and 90˚. In this research, an extrapolation algorithm was used to estimate the azimuth at a near 90˚ elevation. The extrapolation algorithm assumes that the estimated azimuth angle is the extrapolated value. The relevant excerpt of the extrapolation algorithm is shown below.

```
if elv>70 && it>1 && ia>1  % start testing the elevation angles from 70˚
 if (el_array(ia,it)-el_array(ia,it-1))>0 % increasing elevation
% extrapolate the azimuth from a quadratic match to the preceding azimuth
vs. elevation values
elv_prev=el_array(ia,1:it-1);% preceding elevation values
azi_prev=az_array(ia,1:it-1);% preceding azimuth values
cfit=polyfit(elv_prev,azi_prev,2);% quadratic polynomial fit
azi_fit=polyval(cfit,elv);% extrapolate azimuth to current elevation value
az_array(ia,it)=azi_fit;% assume the estimated azimuth to be the
extrapolated value
az_error_estimate=azi_fit-azv_i;
end
      else
az_error_estimate=0;
end
```

In the extrapolation algorithm, a selected azimuth angle of 36˚ was fixed and the elevation angle was varied between 0˚ to 90. For this research a quadratic polynomial fit (polyfit) was used to find the coefficients of the polynomial. The polyfit, fits the preceding elevation angles (elv_prev) to the preceding azimuth angles (azi_prev). The polyval command was used to extrapolate the azimuth angle to the current elevation value. The estimated azimuth angle was assumed to be the extrapolated value. Although the results presented here are for an azimuth angle of 36˚, the extrapolation algorithm is valid for all azimuth angles. The results of the extrapolation algorithm for the azimuth angle of 36˚ are depicted in Figure 6-1.

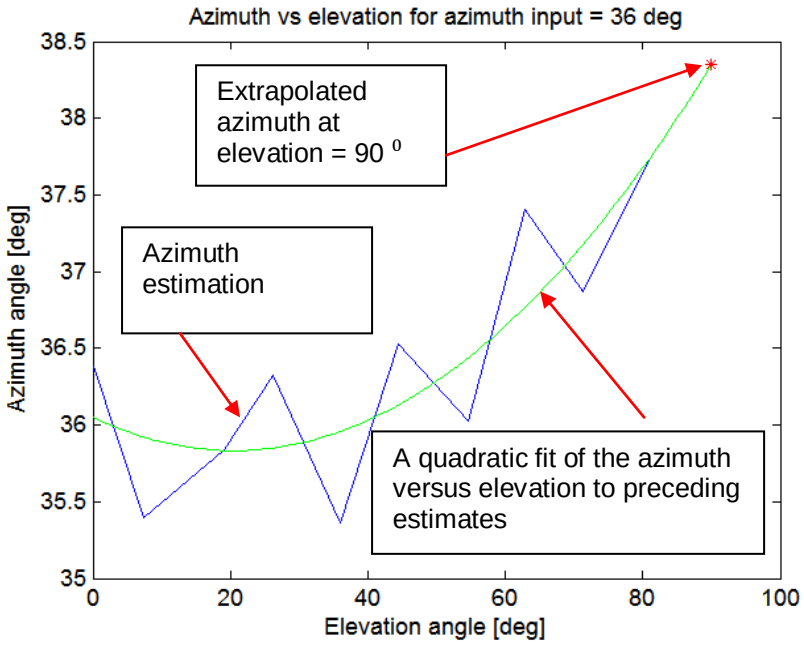

Figure 6-1: Finding the azimuth for elevation angles near 90˚. In this case the input azimuth angle is 36˚

The errors in azimuth estimation that were found at low elevation angles are not a significant problem in the application to HF beacon signals. A study by Minko (2013:74) concludes that the HF beacon signal will not be visible at low elevation angles at the HF DF array at SANSA Space Science Hermanus because the beacon frequency is below the LUF for the incidence from these elevation angles. The HF beacon signal is visible for elevation angles above 45˚. For that reason, the estimation errors at low elevation angles may be ignored. Figures 6-2 and 6-3 show typical distributions of the azimuth and elevation errors with an SNR of 40 dB for all azimuth angles (0˚ to 360˚) in steps of 18˚ and elevation angles (0˚ to 90˚) in steps of 9˚, without an extrapolation algorithm. The results are presented by means of error maps. The error map indicates the distribution of the azimuth and elevation errors for all combinations of angles for a single SNR level. Each block on the error map represents the error associated with a specific azimuth and elevation combination. The results of all the algorithms follow.

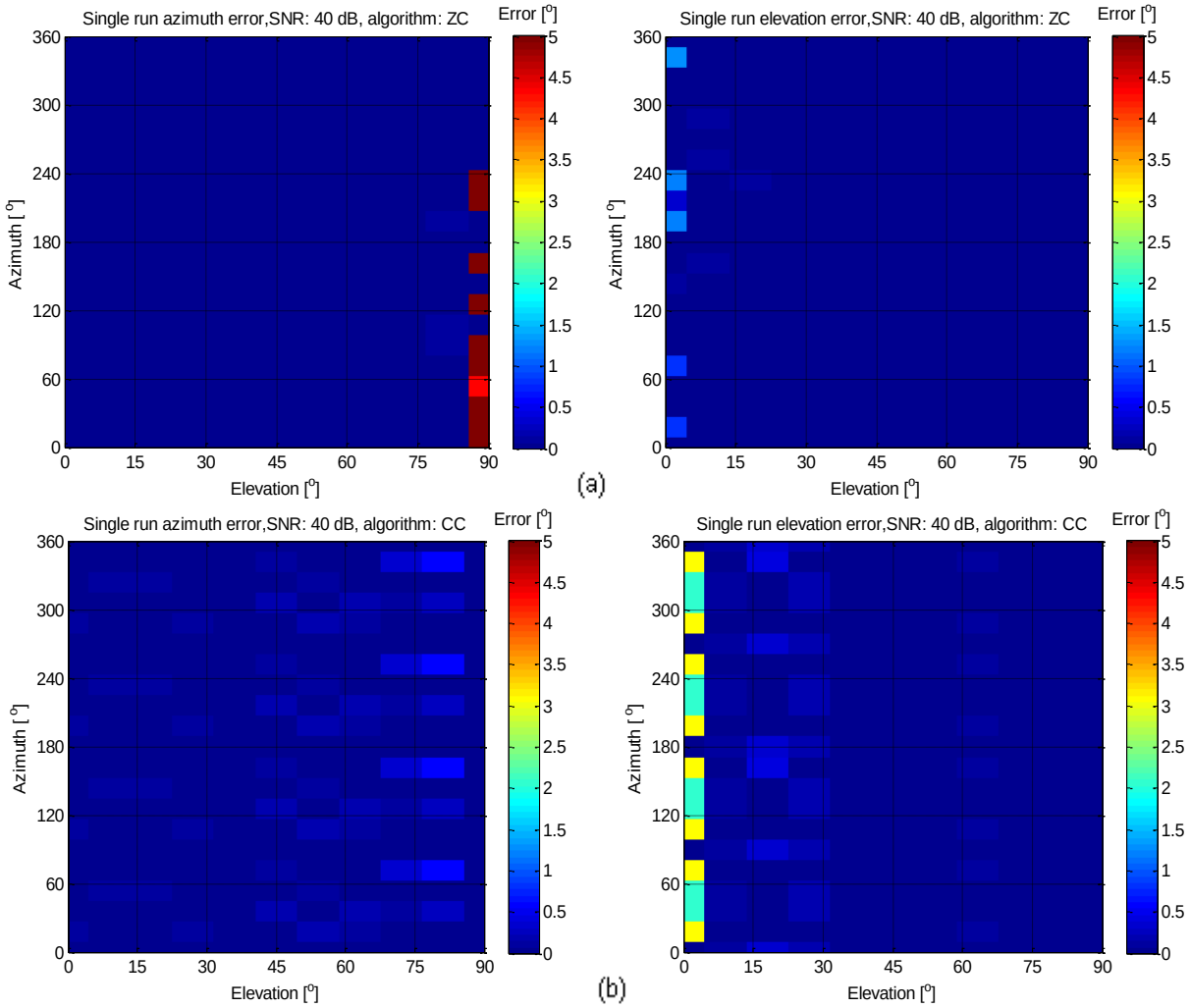

Figure 6-2: The mapping of the error distribution for all the azimuth and elevation angles for (a) ZC and (b) CC with a good SNR of 40 dB. The duration of the realisation of the signal is 1 s. The simulated base band signals are sampled at 22 ks/s. The results are for a single run of the simulation without an extrapolation algorithm

Figures 6-2 and 6-3 show that all the algorithms estimate the azimuth and elevation angles correctly with small errors of less than 1˚ for most combination sets of angles. However, larger azimuth errors of around 5˚ were detected at elevation angles close to 90˚ and elevation errors were found at low elevation angles. Yet estimation errors at low elevation angles are not a threat to the application of the algorithms to HF beacon signals. Azimuth correction with the extrapolation algorithm addressed the azimuth errors that are experienced at elevation angles near vertical.

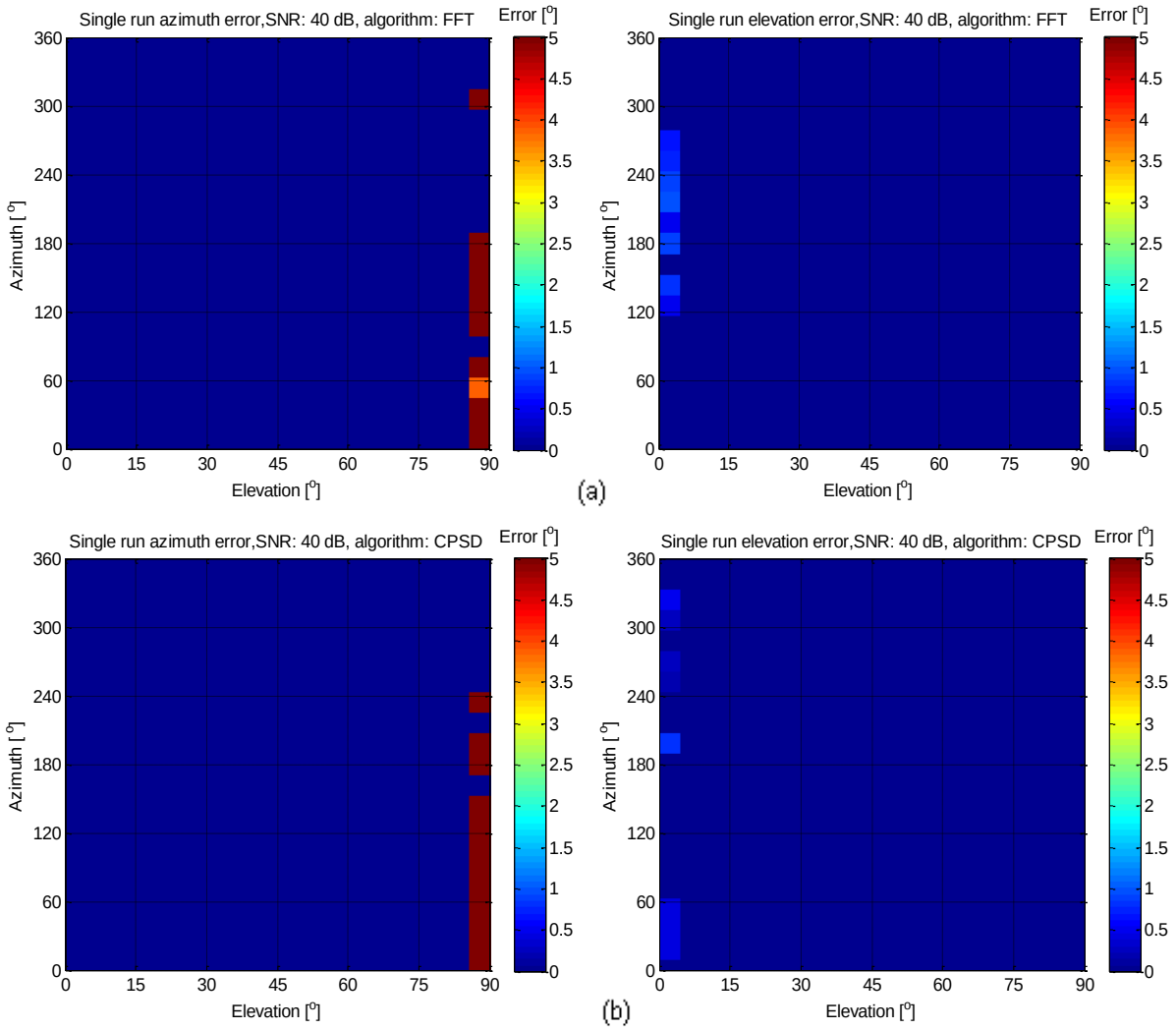

Figure 6-3: The mapping of the error distribution for all the azimuth and elevation angles for (a) FFT and (b) CPSD with a good SNR of 40 dB. The duration of the realisation of the signal is 1 s. The simulated base band signals are sampled at 22 ks/s. The results are for a single run of the simulation without an extrapolation algorithm

Figures 6-4 through 6-5 illustrate the effect of the extrapolation of the azimuth estimation near vertical. The azimuth errors closer to the elevation angles of 90˚ are removed by the extrapolation algorithm. All the algorithms estimate the azimuth angles with maximum error of less than 1˚ for most combinations of angles, after the correction with the extrapolation algorithm. For the estimation of elevation, all the algorithms give the correct estimation for most combinations of angles, where the elevation angle is greater than 45˚.

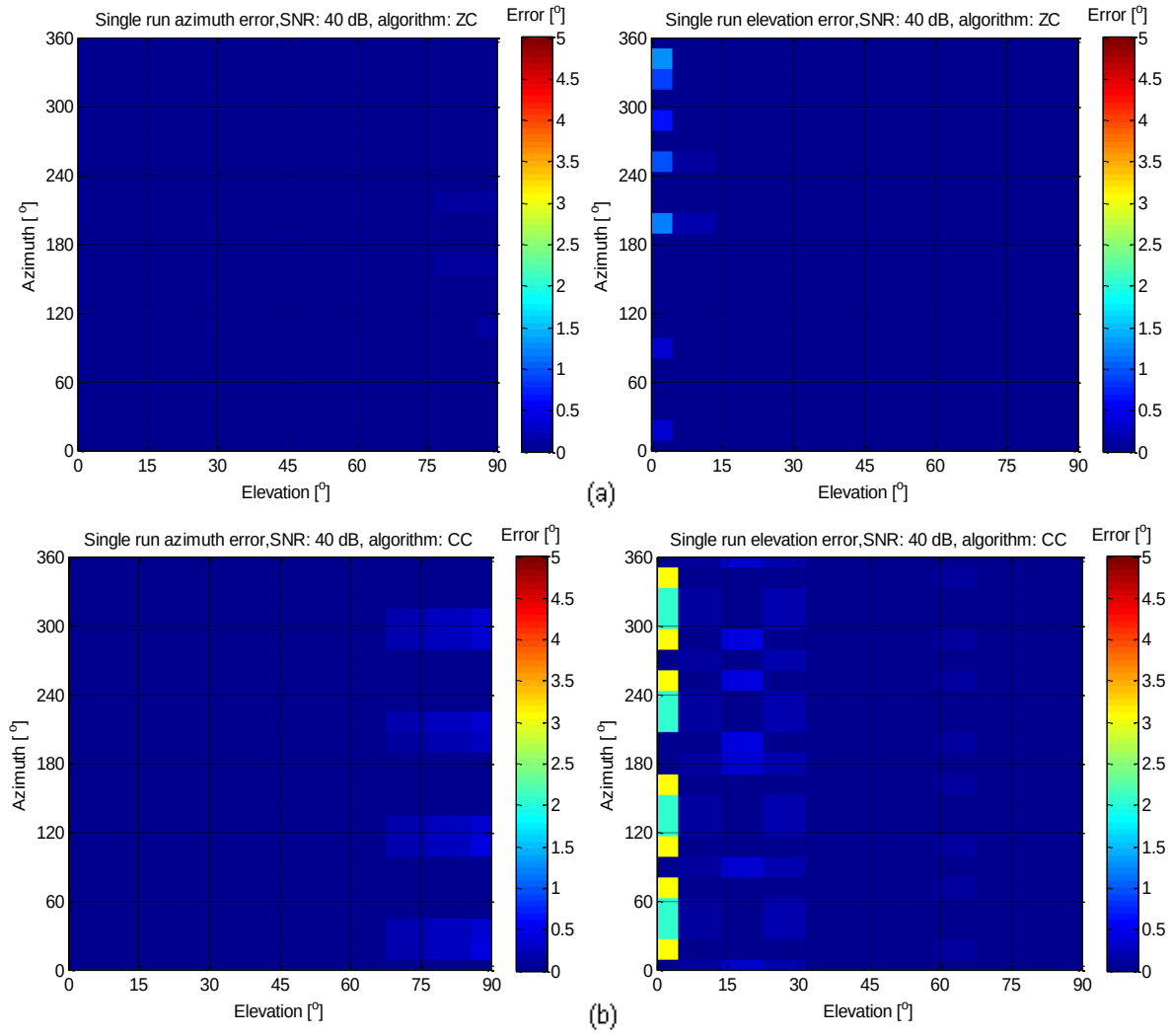

Figure 6-4: The mapping of the error distribution for all the azimuth and elevation angles for (a) ZC and (b) CC with a good SNR of 40 dB. The duration of the realisation of the signal is 1 s. The simulated baseband signals are sampled at 22 ks/s. The results are for a single simulation of each combination of angles, corrected with an extrapolation algorithm

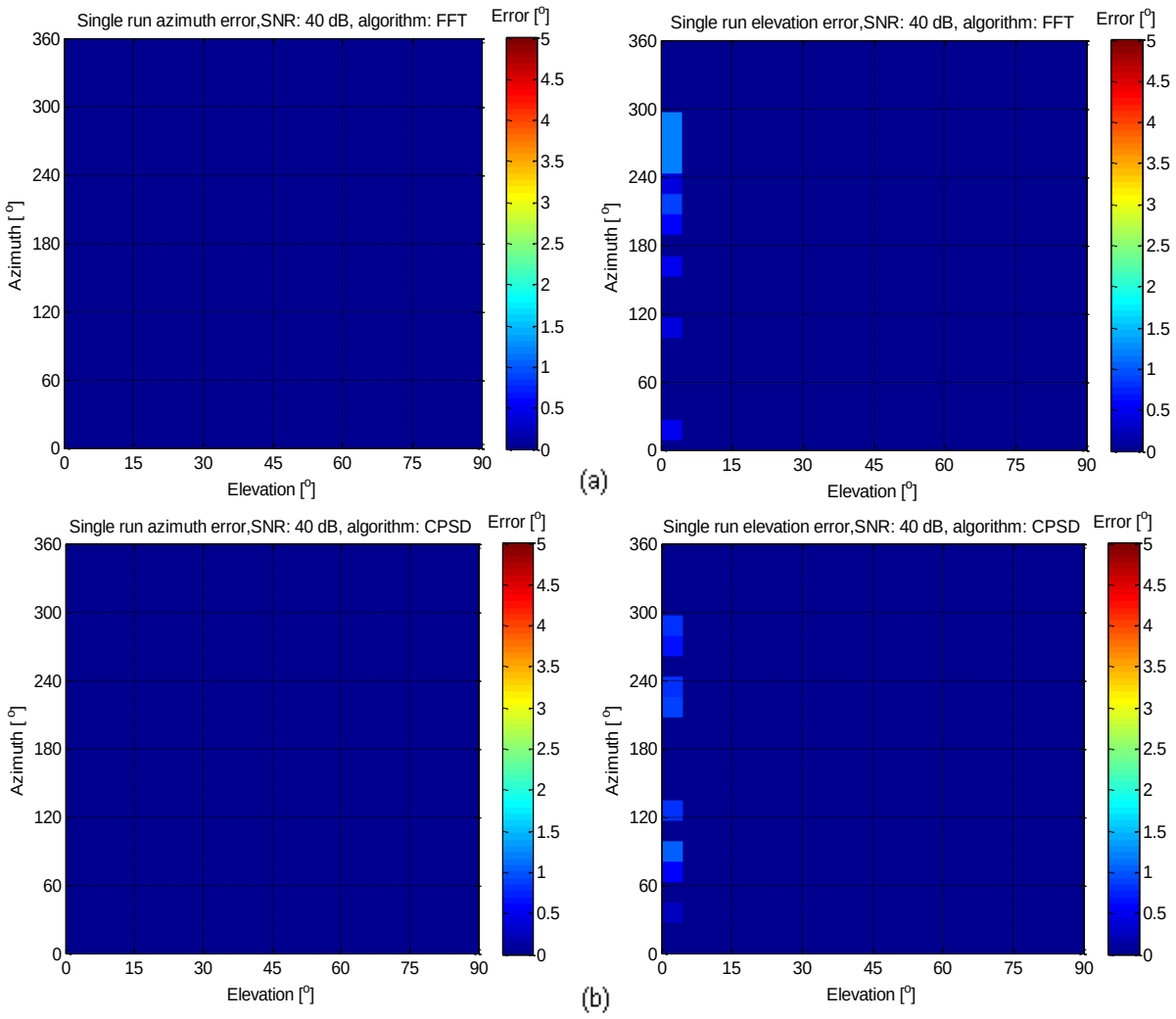

Figure 6-5: The mapping of the error distribution for all the azimuth and elevation angles for (a) FFT and (b) CPSD with a good SNR of 40 dB. The duration of the realisation of the signal is 1 s. The simulated baseband signals are sampled at 22 ks/s. The results are for a single simulation of each combination of angles, corrected with an extrapolation algorithm

The simulations for all the algorithms were run with the extrapolation algorithm to address the azimuth errors near elevation angles of 90˚. Each algorithm was evaluated for the effect of SNR on the SD of the azimuth and elevation errors. The SD is the parameter that measures the accuracy for each algorithm. Furthermore, the speed of computation of each algorithm was determined and compared with that of the other three algorithms. Accuracy and speed were the criteria for selection of the optimum algorithm.

6.3 Accuracy of the algorithms

This section compares the accuracy of all algorithms for their estimation of azimuth and elevation. The SD of the azimuth and elevation errors was used to measure the accuracy of the azimuth and elevation estimation. Gaussian noise was added to the simulated baseband signals to control the SNR. The effect of the SNR on the accuracy of estimation of azimuth

and elevation was compared for all the algorithms. The results presented are for an azimuth angle of 346˚ and elevation angle of 47˚. Figure 6-6 shows the effect of SNR on the performance of each algorithm.

In Figure 6-6, the SNR varies from −10 dB to 50 dB in steps of 5 dB. For every SNR level there is an associated SD of azimuth and elevation errors. It is evident that for all algorithms, the SD of the azimuth and elevation errors decreases as the SNR increases. The SD of azimuth and elevation errors for each algorithm converges to around 0˚ when the SNR increases above 35 dB.

For the ZC algorithm, the SD of azimuth and elevation errors is greater at lower SNR levels and remains constant. The SD of the azimuth errors are distributed between 100˚ and 120˚, while the SD of elevation errors are distributed between 25˚ and 30˚.The SD of azimuth and elevation errors start converging to 0˚, when the SNR increases above 35 dB.

The CC algorithm estimates the azimuth and elevation incorrectly for SNRs lower than – 10 dB, since the distribution of the SD of the azimuth and elevation angles is wide. However, the CC algorithm estimates azimuth and elevation angles with lower SD when the SNR is above 5 dB. For the CC algorithm, the SD of the azimuth and elevation errors approaches 0˚ for all values of SNR above 5 dB.

The FFT and CPSD algorithms achieve the same accuracy in the estimation of the azimuth and elevation angles. Even at lower levels of SNR, the CPSD and FFT estimate the azimuth and elevation angles correctly with minimum errors. The SD of azimuth and elevation errors begins to converge to 0˚ for all values of SNR above 0 dB.

The CPSD and FFT algorithms perform significantly better even at a low SNR, compared to the ZC and the CC algorithms. However, all algorithms perform equally well with a good SNR above 35 dB and more. The azimuth and elevation angles are correctly estimated, with the SD of azimuth and elevation errors converging to less than 1˚.

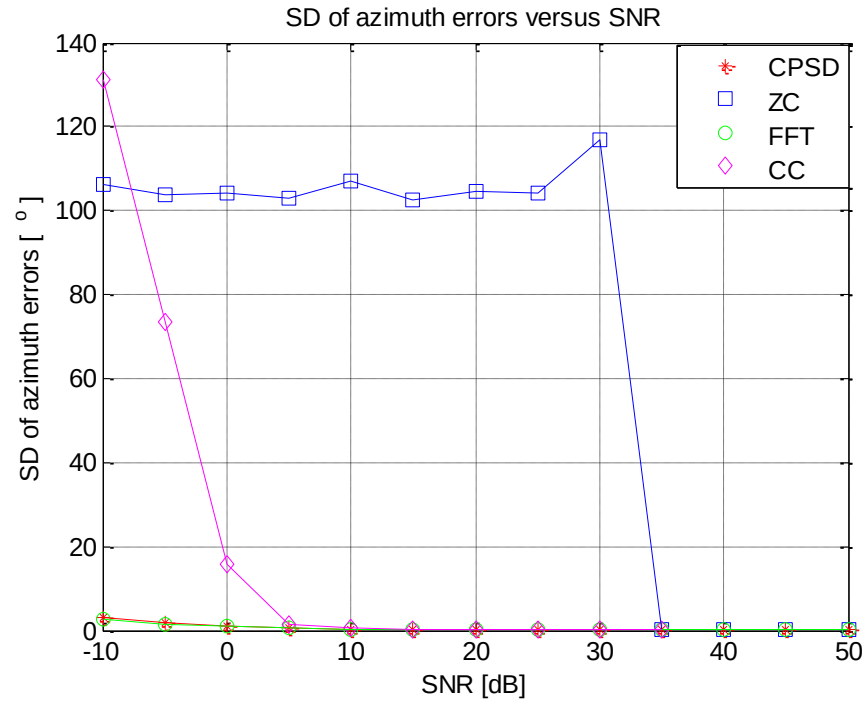

(a) SD of azimuth errors

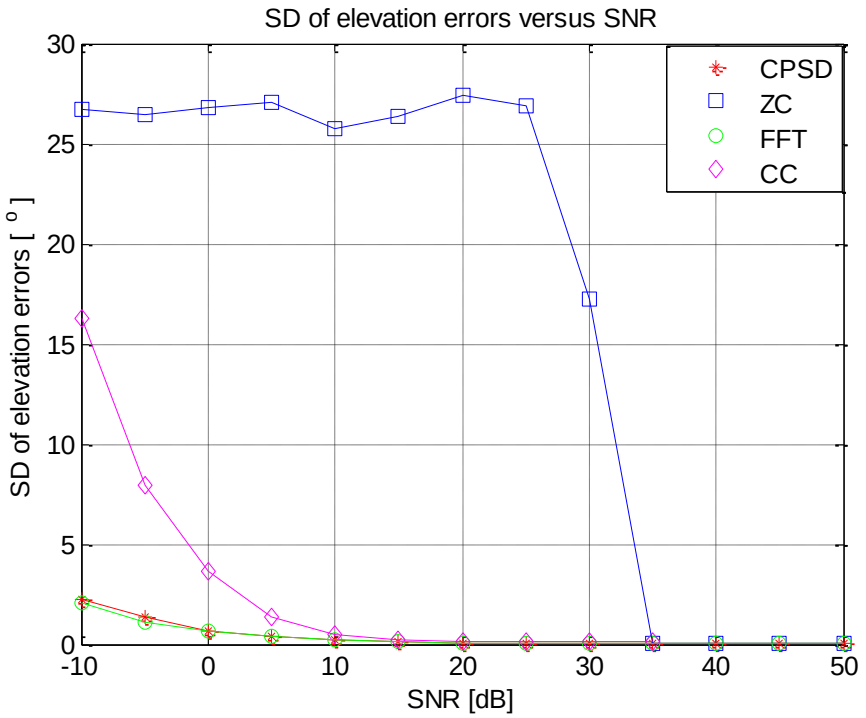

(b) SD of elevation errors

Figure 6-6: The SD of the (a) azimuth and (b) elevation errors as a function of SNR for all the algorithms. These results are for an azimuth of 346° and elevation of 47°. The SD of the errors was determined after 500 Monte Carlo simulations sampled at 22 ks/s. The duration of the realisation of the signals is 1 s. The number of cycles at base band is 1000

A few cycles at baseband were run by decreasing the total duration of the signal for the same input azimuth of 346˚ and elevation of 47˚. The effects on the SD of the azimuth and elevation errors were evaluated.

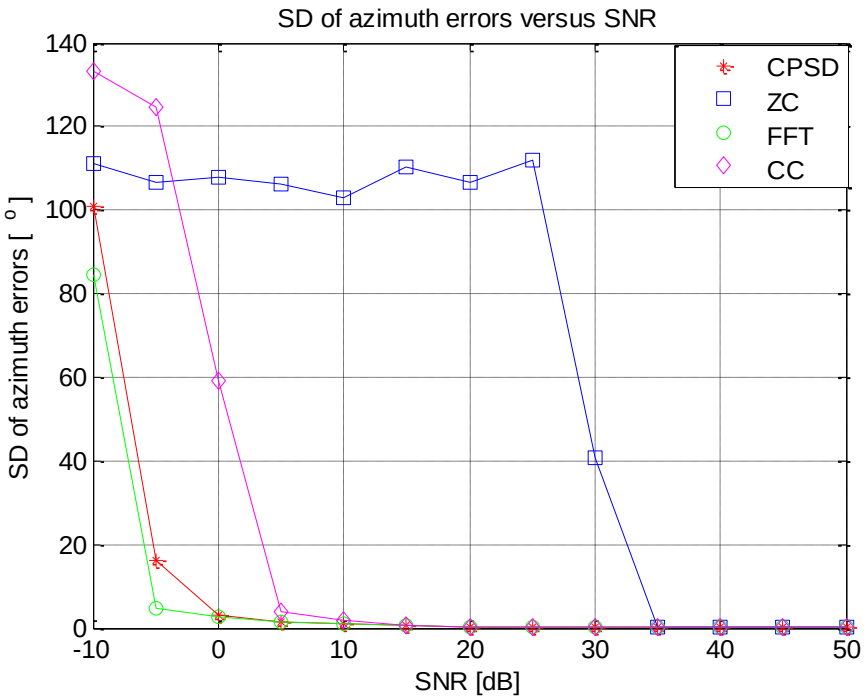

(a) SD of azimuth errors

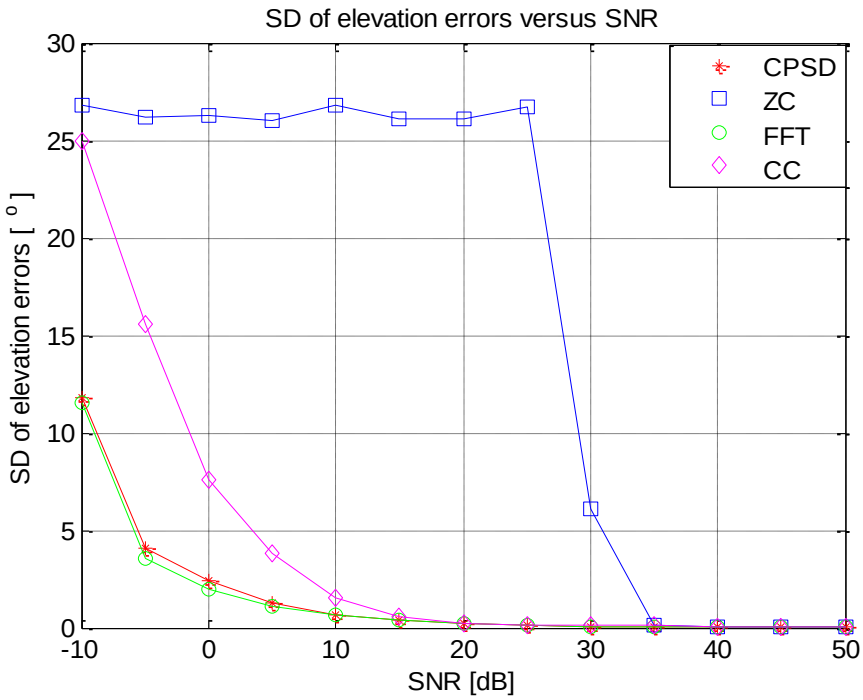

(b) SD of elevation errors

Figure 6-7: The SD of the (a) azimuth and (b) elevation errors as a function of SNR for all the algorithms. These results are for an azimuth of 346˚ and elevation of 47˚. The SD of the errors was determined after 500 Monte Carlo simulations, sampled at 22 ks/s. The duration of the realisation of the signals is 0.1 s. The number of cycles at baseband is 100

In Figure 6-7 the effect of decreasing the total number of cycles at baseband on the SD of the errors is illustrated. The total number of cycles depends on the duration of the signal.

It is evident that the SD of the azimuth and elevation errors increases as the duration of the signal decreases. A significant change was observed with the CPSD and FFT algorithms at lower SNRs. The SD of azimuth and elevation errors increases gradually, as compared to a 1 s signal duration. All the algorithms perform well when the SNR level is 35 dB and above. However, the performances of the CPSD and FFT are very similar, and make it difficult to determine which one is the better of the two. The author continued to evaluate the time each algorithm needed to compute the estimated azimuth and elevation angles.

6.4 Speed of the algorithms

The objective of the study was not to compare the computational cost of the algorithms, but it was to compare the relative speed of the algorithms. The reason for not considering computational complexity is that it is platform and language dependent and the author was limited in what was available for the simulations. The algorithm that able to estimate the DOA with the minimum of errors within the shortest time, is the algorithm of choice. The computation time of each algorithm was determined by using the MATLAB function (tic/toc). The computation time is defined as the time each algorithm takes to estimate all combinations of azimuth and elevation angles, using the SD maps of azimuth and elevation errors, for all azimuth angles (0˚ to 360˚) in steps of 18˚ and all elevation angles (0˚ to 90˚) in steps of 9˚. The SD of azimuth and elevation errors was determined after 100 Monte Carlo simulations. Each algorithm was computed with a good SNR of 40 dB. The simulated baseband signals were sampled at 22 ks/s and the total duration of the signals was 1 s. Figure 6-8 shows the computation time of each algorithm. It was found that decreasing the duration of the signals by selecting fewer cycles at baseband speeds decreased the computation time, but increased the error.

The FFT algorithm is the fastest at estimating the azimuth and elevation angles. The CC is the slowest algorithm, because it is computed between the interpolation signals from the Reference and the other two antennas. The ZC is not the fastest algorithm because it uses the interpolation method that was used for the detection of the ZC points. The CPSD takes longer than the FFT, because the (cpsd) command function computes the CC and uses the FFT of the CC signals to estimate the phase difference from which the azimuth and elevation are determined. The FFT's efficient computation time is due to the fact that it calculates the phase differences from the phases detected at the frequency of operation.

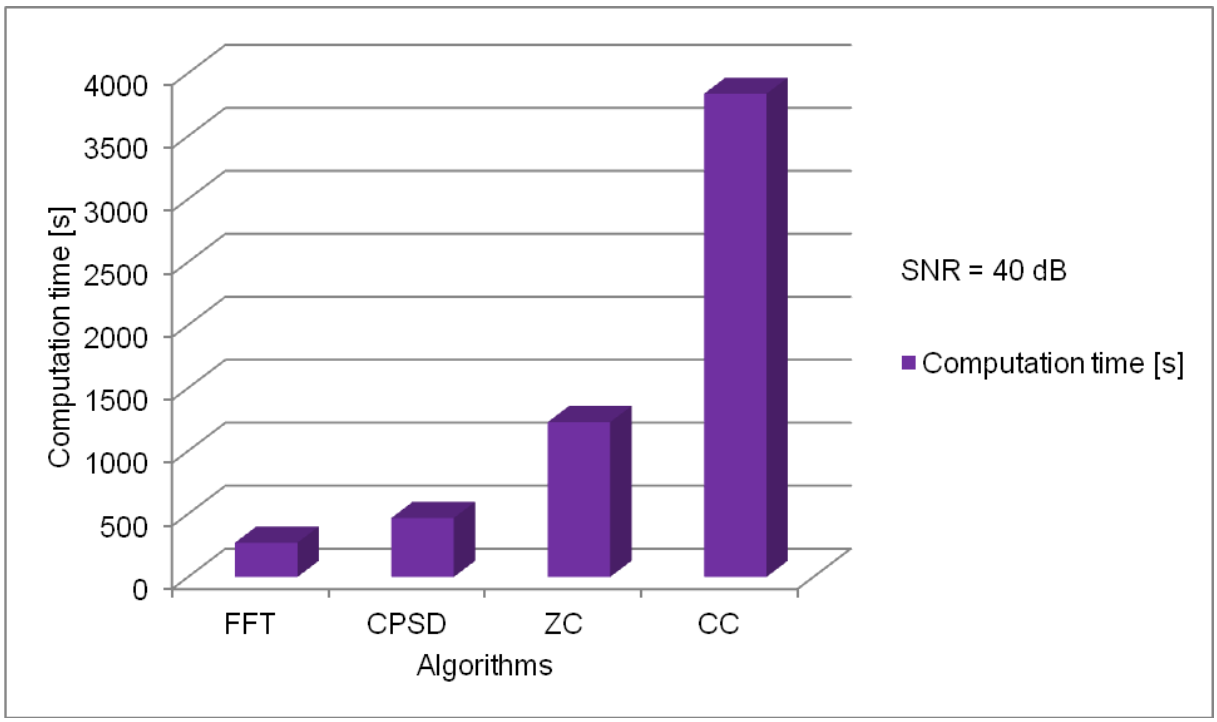

Figure: 6-8: Comparison of the computation times of all the algorithms. The computation time is for all combination of angles, with a good SNR of 40 dB

Thus the FFT algorithm is considered to be the fastest algorithm.

6.5 Accuracy and speed

A particular combination of azimuth and elevation angles was then evaluated against the two criteria. SNRs of 40 dB and 0 dB were used to evaluate the computation time of each algorithm. The comparisons of algorithms for accuracy and speed are presented in Figures 6-9 through 6-12. The results are for an azimuth of 246˚ and elevation of 85˚. The distribution of the SD of the azimuth and elevation errors was determined after 500 Monte Carlo simulations.

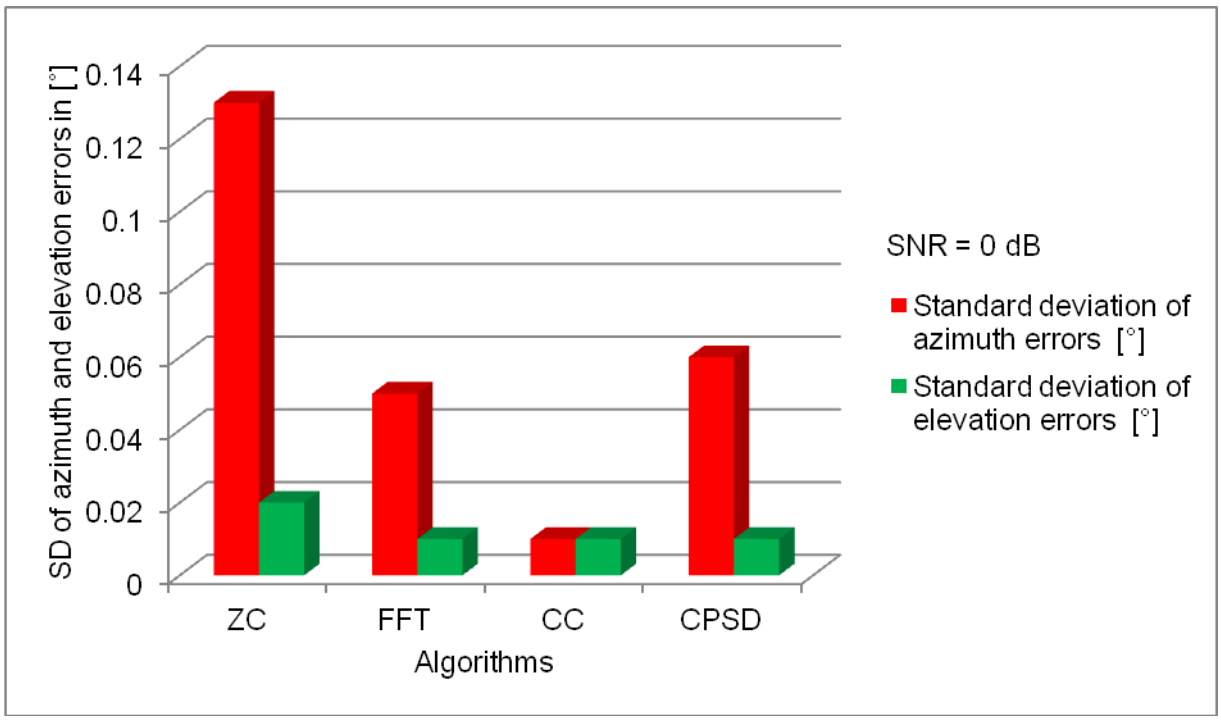

Figure 6-9: Performance of algorithms in terms of accuracy with an SNR of 40 dB. The duration of the realisation of the signal is 1 s and the number of cycles at baseband is 1000

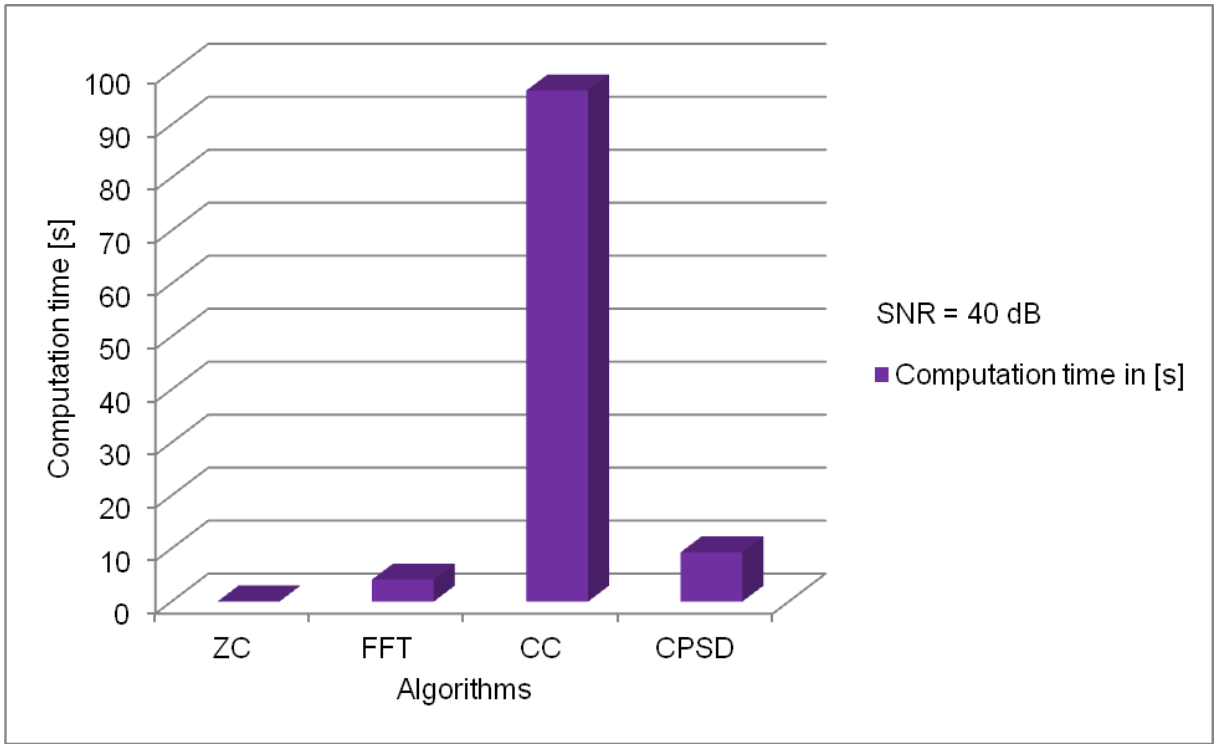

Figure 6-10: Performance of algorithms in terms of speed with an SNR of 40 dB. The duration of the realisation of the signal is 1 s and the number of cycles at baseband is 1000

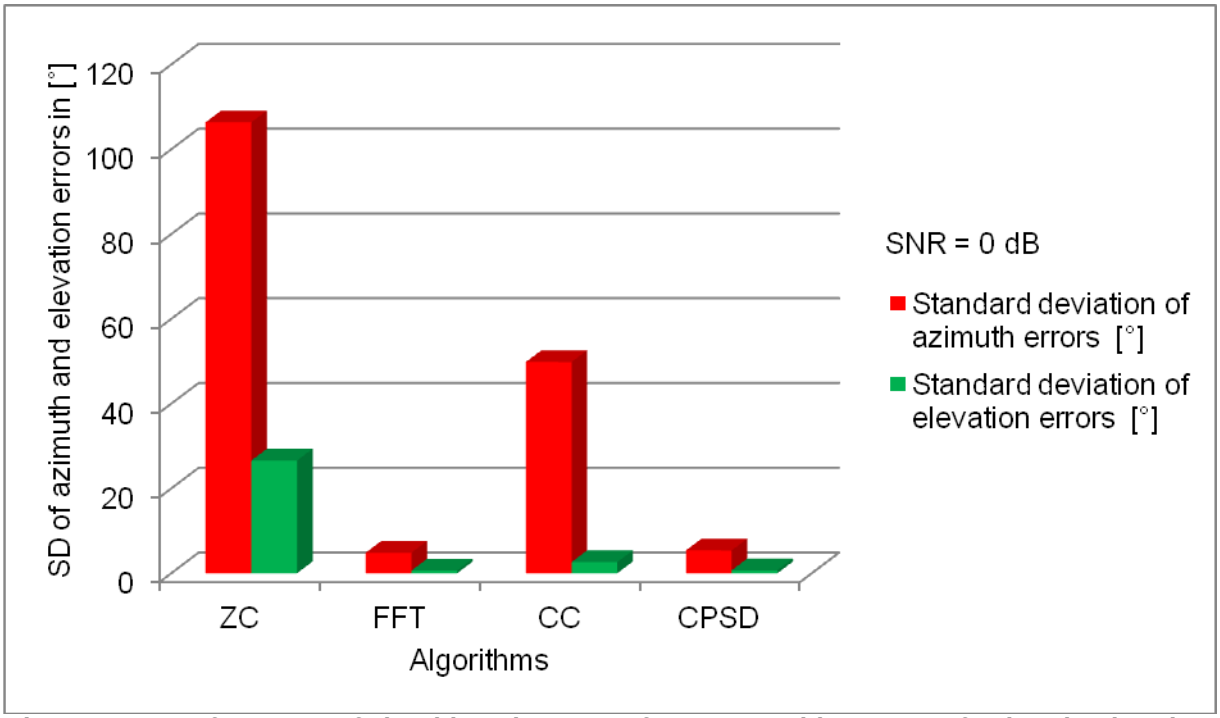

Figure 6-11: Performance of algorithms in terms of accuracy with an SNR of 0 dB. The duration of the realisation of the signal is 1 s and the number of cycles at baseband is 1000

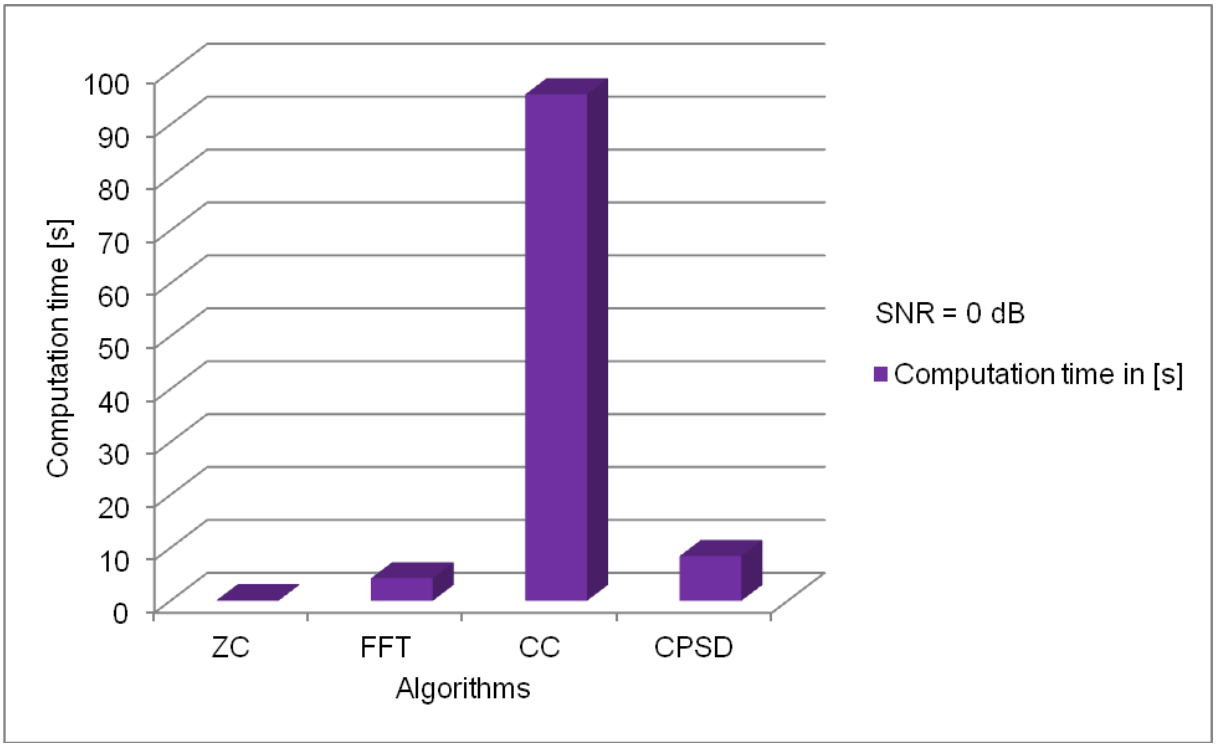

Figure 6-12: Performance of algorithms in terms of speed with an SNR of 0 dB. The duration of the realisation of the signal is 1 s and the number of cycles at baseband is 1000

Figure 6-9 illustrates that all algorithms estimate the azimuth and elevation angles correctly with an SD of azimuth and elevation errors of less than 1˚, and a good SNR of 40 dB. Figure 6-10 shows that the CC algorithm is the slowest of the algorithms. Figure 6-11 shows that the performances of the algorithms deteriorates when the SNR decreases to 0 dB. The high level of noise causes this deviation from their true values. Figure 6-12 also indicates that the CC algorithm is slower than the other algorithms. At 0 dB the CPSD and FFT retain the same accuracy in the estimation of azimuth and elevation angles. The CPSD and FFT algorithms estimate the azimuth and elevation correctly with minimum errors at low SNR levels. The FFT algorithm was selected as the optimum algorithm due to its excellent computation time

6.6 Discussions

With the ZC algorithm, the accuracy of the estimation of azimuth and elevation angles breaks down when the SNR decreases below 35 dB. The accuracy of the estimation of DOA with the ZC algorithm depends on the ZC points and the SNR. With a high SNR, the ZC algorithm estimates the azimuth and elevation angles correctly with minimum errors. The method for detection of the ZC points is significant for the accuracy of the estimation of the azimuth and elevation angles. ZC points need to be correctly detected in order to avoid large errors, especially at low SNR levels. The computation time of the ZC algorithm was not good.

The accuracy of estimation of the azimuth and elevation angles with the CC algorithm becomes poor when the SNR decreases below 10 dB. However, when the SNR increases beyond 25 dB, the SD of both the azimuth and elevation errors improves and starts converging to 0˚.

The CPSD and FFT reach almost the same accuracy in the estimation of azimuth and elevation angles at high SNR values of 40 dB as illustrated in Table 6-1 for a specific azimuth angle of 246˚ and elevation angle of 85˚.

Table 6-1: The magnitude of SD of azimuth and elevation errors for a specific azimuth of 246˚ and elevation of 85˚ for different SNR levels for the CPSD and FFT algorithms

Algorithms	SNR [dB]	SD of azimuth errors [˚]	SD of elevation errors [˚]
FFT	40	0.05	0.01
CPSD	40	0.05	0.01
FFT	10	1.48	0.20
CPSD	10	1.67	0.21
FFT	0	4.98	0.60
CPSD	0	5.41	0.70

The two algorithms still estimates some combinations angles correctly with minimum errors even at a SNR of -20 dB, when the noise level is 100 times larger than the signal amplitude. However at the realistic SNR of 10 dB, the SD of the azimuth and elevation errors from Table 6-1 is 1.48˚ and 0.20˚ respectively for the FFT algorithm, while for the CPSD the SD of azimuth and elevation errors is 1.67˚ and 0.21˚. The FFT algorithm will be favoured compared to CPSD. From the comparison of computation time of these two algorithms, the FFT take less time to estimates the azimuth and elevation angles compared to the CPSD algorithm. FFT was selected as an optimum algorithm due to the less computation time.

6.7 Summary

The ZC at high and low SNR levels is the fastest algorithm for an azimuth of 246˚ and elevation of 85˚. However, when comparing the computation time of the algorithms for the estimation of all combinations of azimuth angles (0˚ to 360˚) and elevation angles (0˚ to 90˚), the FFT is the fastest algorithm. The CC algorithm takes more time to estimate the DOA compared to FFT, CPSD and ZC.

The ZC algorithm estimates the azimuth and elevation angles with large errors at low SNR levels, due to multiple ZC points resulting from high levels of noise. Several methods for detecting the ZC points were tried in order to address large errors at low SNR levels, such as Schmitt trigger. However, the result was the same as using the simple linear interpolation method to detect the ZC points. The detection of the ZC points, plays a major role in the estimation of the phase difference between the two signals, which has an effect on the DOA estimation. The accuracy of estimation was the same for the CPSD and FFT algorithms.

Thus the FFT is faster than the CPSD, and the CPSD and FFT provide the greatest accuracy. FFT was selected as the optimum algorithm to estimate the azimuth and elevation angles of the HF signal for its speed of computation.

CHAPTER SEVEN: CONCLUSION AND FUTURE WORK

7.1 Conclusion

In this chapter a conclusion is drawn and recommendations are made for further research in this field.

The objective of the study was to evaluate algorithms for the estimation of the DOA from the phase difference of the HF beacon signal transmitted from ZACUBE-1 (TshepisoSAT). The performance of each algorithm was tested with variables such as SNR, the total duration of the signals, and the number of cycles at baseband. The criteria for selection of the optimum algorithm were accuracy and speed. The DOA of the signal was derived by processing the ideal simulated baseband signals received from the Reference antenna, South antenna 1 and West antenna 1. The algorithms were tested using simulated signals. The comparison of the algorithms was done for a three-element L-shaped array.

The RF frequency signal of the HF beacon signal changes due to the Doppler shift. The maximum Doppler shift frequency, for a satellite on the horizon, was estimated to be about ± 354.1 Hz for the general case. The maximum Doppler shift was passed to the baseband signals. The number of cycles used for the determination of the phase and elevation angles, are sufficient not to cause a significant variation in the performance of the algorithms between the extremes of the Doppler shifted frequency. Having determined this, a baseband frequency of 1 kHz was used for the error analysis and for the selection of the best algorithm.

There were some discrepancies in the azimuth estimation for elevation angles near 90°, however, an extrapolation algorithm was used to address the azimuth errors. All the algorithms were corrected by means of the extrapolation algorithm.

Evaluation of the algorithms:

The evaluation of the algorithms was based on two criteria:

- Accuracy: The accuracy was expressed in terms of the SD of the azimuth and elevation errors for a range of SNR levels. In the first experiment, the SD of the azimuth and elevation errors of a particular combination of azimuth and elevation angles were evaluated for a range of SNR levels for each algorithm. The first experiment showed where the errors begin to increase for each algorithm when using a particular combination of azimuth and elevation angles. In the second experiment, the SD of azimuth and elevation errors for all azimuth angles (0° to 360°) and

elevation angles (0˚ to 90˚) were evaluated with a single SNR level for each algorithm.

- Speed: The speed was expressed in terms of the computation time of each algorithm for the estimation of a particular combination of azimuth and elevation angles. Likewise the computational time for all azimuth angles (0˚ to 360˚) and elevation angles (0˚ to 90˚) from each algorithm was calculated.

- Accuracy and speed: Each algorithm was evaluated in terms of accuracy and speed.

The results of this research, lead us to the following conclusions:

- The ZC algorithm is the simplest algorithm for DOA estimation. Its accuracy depends on the SNR and the detection of the ZC points. At high SNR levels, multiple ZC points are detected which influence the performance of the algorithm estimation. ZC algorithm was found to break down at SNR levels below 35 dB. For a particular combination of azimuth and elevation angles, the ZC algorithm is fast, however, the speed slows down when processing all the azimuth and elevation angles. The ZC algorithm estimate the azimuth and elevation angles with an SD of the azimuth and elevation errors of less than 1˚ with an SNR of 40 dB and above

- The CC algorithm is very slow in the estimation of the DOA compared to the other three. The estimation accuracy of the CC algorithm is better than the ZC algorithm. The CC algorithm breaks down at SNR levels below 10 dB. The CC algorithm estimate the azimuth and elevation angles with an SD of the azimuth and elevation errors of less than 1˚ with an SNR of 40 dB and above

- The CPSD and FFT algorithms are equally accurate in the estimation of the DOA. These two algorithms outperform the CC and ZC algorithms. The CPSD and FFT estimate the DOA with a small SD of errors for some combinations of azimuth and elevation angles with a low SNR of – 20 dB. However, the FFT is the faster than the CPSD. Both the CPSD and FFT estimate the DOA with an SD of the azimuth and elevation errors of less than 1˚ with an SNR of 40 dB and above.

All the algorithms estimate the DOA correctly with an SD of the azimuth and elevation errors of less than 1˚ with a high SNR of 40 dB and above.

Selection of the best algorithm:

The evaluation of the algorithms led to clear winners in the race for the best algorithm. Since both the CPSD and FFT are equally accurate in the estimation of the DOA, the speed of computation was considered to be the parameter that would determine the best algorithm. Thus FFT algorithm was selected as the optimum algorithm for the estimation of the DOA.

7.2 Future work and Recommendations

- Further research will be required to evaluate these algorithms for real-time applications. The algorithms have to be converted to other programming languages such as C++ or C. Zhou *et al*., (2012) proposed a ZC algorithm for time difference estimation that was suitable for real time application, low computational and an estimation accuracy comparable to that of the FFT algorithm.

- Since all the algorithms that were evaluated, estimate the DOA correctly with small degrees of error with a high SNR of 40 dB and above, the ZC, CC and CPSD may be use for the case a signal with a high SNR of 40 dB and above is received. They are useful due to their accuracy at high SNR levels.

- The ZC algorithm can be improved by reducing the large errors at low SNR levels by means of methods for accurate detection of the ZC points. The multiple ZC points lead to incorrect estimation of the DOA, resulting in large errors. Post-processing signal conditioning and pre-detection low pass filtering may reduce the noise levels before the phase differences are estimated (Sedlacek & Krumpholc, 2005).

- More accurate estimates of the DOA are possible by adding more elements to the array, and basing the simulations on the extended array. The design of the HF DF array at SANSA Space Science provides for possible future expansion to five and seven elements. The results obtained for the three elements may be used for comparison with simulations that are based on the five or seven elements.

BIBLIOGRAPHY

Agaba, D. 2012. Analysis of satellite to ground ray paths for the calibration of the SuperDARN radar by means of the HF Beacon on the ZACUBE1 CubeSat. Unpublished MSc thesis, University .of Cape Town: Cape Town.

Akers, G.A. 2000. Low band direction finding using an ensemble of structurally integrated antennas. Unpublished Master's thesis, Air Force Institute of Technology: AU.

Allnutt, J. E. 1989. *Satellite-to-ground radiowave propagation*: theory, practice and system impact at frequencies above 1 GHz. Stevenage: Peter Peregrinus.

Ankita, G., Rajeev, T. & Sachin, M. 2013. An efficient approach to zero crossing detection based on opto-coupler. *International Journal of Engineering Research and Applications,* 3(5): 834-838, September –October.

Bailey, A. D., & McClure, W. C. 1963. A sum-and-difference interferometer system for HF radio direction finding. *IEEE Transactions on Aerospace and Navigational Electronics,* 1: 65-72.

Barringer, M. H., & Springer, K. D. 2008. *Radio wave propagation, Engineering Handbook, 7th ed.* Washington, DC: National Association of Broadcasters.

Benesty, J. 2000. Adaptive eigenvalue decomposition algorithm for passive acoustic source localization. *The Journal of the Acoustical Society of America*, *107(*1): 384-391.

Bland, J. M., & Altman, D. G. 1996. Statistics notes: measurement error. *Bmj*, *312*(7047): 1654: http://www.bmj.com/content/312/7047/1654 [8 July 2014].

Changlin, J. C. 2006. The estimation method on the phase delay between two real signals. *2006 International Conference on Communications, Circuits and Systems Proceedings,* Guilin, June 2006*,* IEEE*,* 1: 394-397.

Chen, J., Benesty, J., & Huang, Y. 2003. Time delay estimation using spatial correlation techniques. *Eighth International Workshop Acoustic Echo and Noise Control (IWAENC'03),* Kyoto, September 2003*.* IWAENC*:* 207-210.

Cheng, T., Gui, X., & Zhang, X. 2013. A dimension separation-based two-dimensional correlation interferometer algorithm. *EURASIP Journal on Wireless Communications and Networking*, 1:1-10.

Cilliers, P.J., Agaba, D., Inggs, M. & Van Zyl, R. 2013. Calibration of a SuperDARN radar antenna by means of a satellite beacon on a CubeSat. *IGARSS*, *July 2013*. IGARSS, 1290-1293.

Cilliers, P. 2012. Electric and magnetic field theory V: space applications. Hermanus: SANSA Space Science. [Unpublished course notes].

Corbin, C. F. 2011. High frequency direction finding using structurally integrated antennas on a large airborne platform. Unpublished MSc thesis. Air Force Institute of Technology- AU.

Coetzee, P.J. 2012. An interferometric direction finder for the 14.099 MHz transmissions from the ZACUBE-1 Satellite. Bellville: Cape Peninsula University of Technology [Unpublished notes].

Danilkin, N. P. 1997. Transionospheric propagation at the boundary of radio transparency range: results of Russian space experiments and plans for low orbiting pilot space station. *Tenth International Conference on Antennas and Propagation,* Edinburgh, 14-17 April 1997. *IET,* 2:31-34, *(Conf Publ. No. 436).*

Dhull, S., Arya, S. & Sahu, O. P. 2010. Comparison of time-delay estimation techniques in acoustic environment. *International Journal of Computer Applications*, *8*(9): 29-31.

El-Barbary, K.A., Mohamed, T. S., & Melad, M. S. 2013. High resolution direction of arrival estimation (Coherent Signal Source DOA Estimation). *International Journal of Engineering Research and Applications (IJERA),* 3(1): 132-139, January-February.

Erad, Y., Vered, U., Vered, G. & Erad, M. 2013. Direction finding system device and method.*United States. Patent Application Publication*, 1-34.

Royal Academy of Engineering. 2013. *Extreme space weather: impacts on engineered systems and infrastructure.* http://www.raeng.org.uk/news/publications/list/reports/space_weather_full_report_final.pdf [10 March 2014].

Gething, P. J. 1991. *Radio direction finding and superresolution*. London: Peter Peregrinus.

Goodman, J. M. 2005. *Space weather & telecommunications*. New York: Springer.

Greenwald, R. A., Baker, K. B., Dudeney, J. R., Pinnock, M., Jones, T. B., Thomas, E. C., & Yamagishi, H. 1995. Darn/Superdarn. *Space Science Reviews*, *71*(1-4): 761-796.

Haydon, G. W., Lucas, D. L., & Pinson, G. S. 1988. High frequency sky-wave propagation predictions in the design of broadcast systems. *IEEE Transactions on Broadcasting*, *34*(2): 238-241.

Herndon, H. J. 1991.Small-aperture radio direction-finding. http://www.amazon.com/Small-Aperture-Radio-Direction-Finding-Artech-Library/dp/0890064202 [16 July 2014].

Intelsat General Corporation. 2013. Satellite basics.
http://www.intelsatgeneral.com/resources/satellite-basics
[2 September 2014]

Introduction to HF radio propagation. 2012. http://www.ips.gov.au/Educational/5/2/2
[2 September 2014]

Jianhua, Z., Hong, X., & Jianping, Y. 2000. Analysis of the dipole circular array in interferometric direction-finding system. *Proceedings of the 5th International Symposium on Antennas, Propagation and EM Theory,* Beijing, August 2000. *I*SAPE*:* IEEE*:* 255-260.

Jha, S., & Durrani, T. 1991. Direction of arrival estimation using artificial neural networks. *IEEE Transactions on Systems, Man and Cybernetics, 21*(5): 1192-1201.

Jones, C. E. 2006. The basics of radio wave propagation. http://ecjones.org/propag.html [11 March 2014].

Kawase, S. 2007. Radio interferometer for geosynchronous-satellite direction finding. *IEEE Transactions on Aerospace and Electronic Systems,* 43(2): 443-449.

Khaddour, H. 2011. A comparison of algorithms of sound source localization based on time delay estimation. *Electrotechnic magazine: elektrorevue*, 2 (1): 31-37.

Kintner, P. M., Ledvina, B. M. & De Paula, E. R. 2007. GPS and ionospheric scintillations. *Space Weather*, *5*(9): 1-23, 7 September.

Knapp, C., & Carter, G. C. 1976. The generalized correlation method for estimation of time delay. *IEEE Transactions on Acoustics, Speech and Signal Processing, 24*(4): 320-327.

Koons, H.C., Mazur ,J.E., Selsnick ,R.S., Blacke, J.B. ,Fennell, J.F. ,Roeder, J.L., & Anderson, P.C. ,1999, "The Impact of the Space Environment on Space Systems", Aerospace technical Report, TR-99(1670), Los Angeles, CA: Space and Missile Systems Center.

Kraus, J. D., & Fleisch, D. A. 1984. Electromagnetics*:* New York: McGraw-Hill.

Liang, J. 2009. Joint azimuth and elevation direction finding using cumulant.*Sensors Journal, 9*(4): 390-398.

Lin, S. N., & Chern, S. J. 1998. A new adaptive constrained LMS time delay estimation algorithm. *Signal processing*, *71*(1): 29-44.

Liu, T. H., & Mendel, J. M. 1998. Azimuth and elevation direction finding using arbitrary array geometries. *IEEE Transactions on Signal Processing, 46*(7): 2061-2065.

Liu, Q. 1999. Doppler measurement and compensation in mobile satellite communications systems. *Military Communications Conference Proceedings,* Atlantic City, NJ, 31 October – 3 November 1999*. IEEE*, 1: 316-320.

Lusis, D. J. 1983. HF propagation: the basics.*QST journal of the American Radio Relay League*, 11:11-15 https://www.arrl.org/files/file/Technology/tis/info/pdf/8312011.pdf [16 July 2014].

Ma, W. K., Hsieh, T. H., & Chi, C. Y. 2009. DOA estimation of quasi-stationary signals via Khatri-Rao subspace. *IEEE International Conference on Acoustics, Speech and Signal Processing,* 19-24 April 2009*. IEEE:* 2165-2168.

Mažeika, L., & Draudvilienė, L. 2010. Analysis of the zero-crossing technique in relation to measurements of phase velocities of the Lamb waves. *Ultrasound*, 66(2): 7-12.

McKinnell, L. 2008. Introducing Hermanus. http://www.ips.gov.au/IPSHosted/INAG/web-69/2008/introducing_hermanus.pdf [19 May 2014]

McNamara, L. F. 1991. *The ionosphere: communications, surveillance, and direction finding*. Malabar, FL: Krieger Publishing Company.

Minko, S. F. 2013. CubeSat mission design for characterising the dual auroral radar network (SuperDARN) field of view. MTech thesis, Cape Peninsula University of Technology, Bellville.

Mošna, Z., Šauli, P., & Santolık, O. 2008. Analysis of Critical Frequencies in the Ionosphere. *WDS' Proceedings of Contributed Papers*. 172-177.

Neri, F. 2006. *Introduction to electronic defense systems*. Raleigh, NC: SciTech Publishing.

Omologo, M., & Svaizer, P. 1994. Acoustic event localization using a crosspower-spectrum phase based technique. *IEEE International Conference on Acoustics, Speech, and Signal Processing,* 19-22 April 1994*. IEEE, 2:* II-273.

Papandreou, P. 1997.Design and prototype development of an optimum symmetrical number system direction finding array. Unpublished MSc thesis, Naval Postgraduate School, Monterey CA.

Paulose, S., Sebastian, E., & Paul, B. 2013. Acoustic source localization. *International Journal of Advanced Research in Electrical, Electronic and Instrumentation Engineering*, 2 (2): 933-939. February.

Poole, I. 1999. Radio waves and the ionosphere. *Qst*, *83*(11): 62-64.

Pozar, D. M. 2009. *Microwave engineering*. 3rd ed. New York: John Wiley & Sons.

Qinghua, L., Shan, O. & Liangnian, J. 2013. Two-dimensional DOA estimation with L-shaped array based on a jointly sparse representation. *Information Technology Journal*, *12*(10): 2037-2042

Rishbeth, H., & Mendillo, M. 2001. Patterns of F2-layer variability. *Journal of Atmospheric and Solar-Terrestrial Physics*, *63*(15): 1661-1680.

Roberts, R. A. & Mullis, C.T. 1987. *Digital signal processing*. Reading, MA: Addison-Wesley Publishing Company.

Sanudin, R., Noordin, N. H., El-Rayis, A. O., Haridas, N., Erdogan, A. T. & Arslan, T. 2011. Analysis of DOA estimation for directional and isotropic antenna arrays*. Antennas and Propagation Conference (LAPC),* Loughborough, 14-15 November 2011. IEEE: 1-4.

Sedlacek, M., & Krumpholc, M. 2005. Digital measurement of phase difference - a comparative study of DSP algorithms. *Metrology and Measurement Systems*, *12*(4): 427-448.

Shen, M., & Liu, H. 2009. A modified cross power-spectrum phase method based on microphone array for acoustic source localization. *IEEE International Conference on Systems, Man and Cybernetics,* San Antonio TX, 11-14 October 2009*.* IEEE: 1286-1291.

Shi, L. & Zhang, C. 2010. Algorithm of signal processing with five – channel interferometer. *Proceedings of International on Symposium Signals, Systems and Electronics* (ISSSE2010), Nanjing, 17-20 September 2010. IEEE, 2:1-4.

Shomorony, I., & Avestimehr, A. S. 2013. Worst-case additive noise in wireless networks. *IEEE Transactions on Information Theory*, 59(6), 3833-3847.

Shrestha, P. L., Hempel, M., Mahasukhon, P., Ma, T., & Sharif, H. 2012. Performance analysis for direction of arrival estimating algorithms. *IEEE 75th Vehicular Technology Conference (VTC Spring).* Yokohama, 6-9 May 2012. IEEE:1-5.

Silva, E., O'Connor, S. & Massa, C. 2011. A passive direction finding system for locating pulsed emitter signals. Unpublished BSc thesis. Worcester Polytechnic Institute, CA.

Smith, S. W. 1997. *The scientist and engineer's guide to digital signal processing*. San Diego, CA: California Technical Publishing.

Tachioka, Y., Narita, T., & Iwasaki, T. 2012. Direction of arrival estimation by cross-power spectrum phase analysis using prior distributions and voice activity detection information. *Acoustical Science and Technology*, *33*(1): 68-71.

Tsai, P.H. 2008. Broadcast signal direction finder. Unpublished BSc thesis, University of Cape Town, Cape Town.

Tshisaphungo, M. 2009. Validation of high frequency propagation prediction models over Africa. Unpublished MSc thesis, Rhodes University, Grahamstown.

Tsui, J.B. 2001. *Fundamentals of global positioning system receiver: a software approach*. New York: John Wiley & Sons.

Van Zyl, R. R., Visser,D.F., Cilliers, P. J. & Opperman, B. D.L. 2013. ZACUBE-1 space weather mission: characterize the SuperDARN HF radar antenna array at SANAE-IV, *Space Weather*, 11: 52-54.

Visser, D.F. 2011. CubeSat mission design for characterising the dual auroral radar network (SuperDARN) field of view. *62nd International Astronautical Congress*, Cape Town, 3-7 October 2011.

Visser, D.F. 2009. ZACUBE-1 (1U CubeSat) Mission Requirements and Technical Specifications. Bellville: Cape Peninsula University of Technology. [Unpublished Technical Report].

Welch, P. D. 1967. The use of fast Fourier transform for the estimation of power spectra: a method based on time averaging over short, modified periodograms. *IEEE Transactions on Audio and Electroacoustics*, *15*(2): 70-73.

Woellert, K., Ehrenfreund, P., Ricco, A. J. & Hertzfeld, H. 2011. Cubesats: cost-effective science and technology platforms for emerging and developing nations. *Advances in Space Research*, *47*(4): 663-684.

Xiong, B., Li, G. L., & Lu, C. H. 2006. DOA estimation based on phase-difference. *8th International Conference on Signal Processing,* Beijing, 2006. IEEE,1.

Yamaguchi, T. J., Soma, M., Halter, D., Raina, R., Nissen, J., & Ishida, M. 2001. A method for measuring the cycle-to-cycle period jitter of high-frequency clock signals*. In VLSI Test Symposium, 19th IEEE Proceedings on. VTS 2001,* 102-110. IEEE.

Zhang, Y., & Abdulla, W. H. 2005. A comparative study of time-delay estimation techniques using microphone arrays, report 619. Auckland: The University of Auckland, School of Engineering.

Zhou, C., Qiao, C., Zhao, S., Dai, W., & Li, D. 2012. A zero crossing algorithm for time delay estimation. *IEEE 11th International Conference Signal Processing (ICSP),* Beijing, 21-25 October 2012. *IEEE,*1:65-69.

Zolesi, B. & Cander, L. R. 2013. Ionospheric prediction and forecasting. Berlin: Springer.

APPENDICES

Appendix A: SD of azimuth and elevation errors versus number of cycles at baseband

The graph below illustrates the effect of increasing the total time by using more cycles at baseband for the SD of the azimuth and elevation errors. The comparison was done for two algorithms, ZC and CPSD. Furthermore, the effect of the Monte Carlo simulations or number of runs on the SD of the azimuth and elevation errors, was evaluated. It was found that the number of runs does not have an effect on the SD of the errors. However, the number of cycles at baseband has an effect on the SD of the azimuth and elevation errors. Increasing the number of cycles at baseband decreases the SD of the azimuth and elevation errors

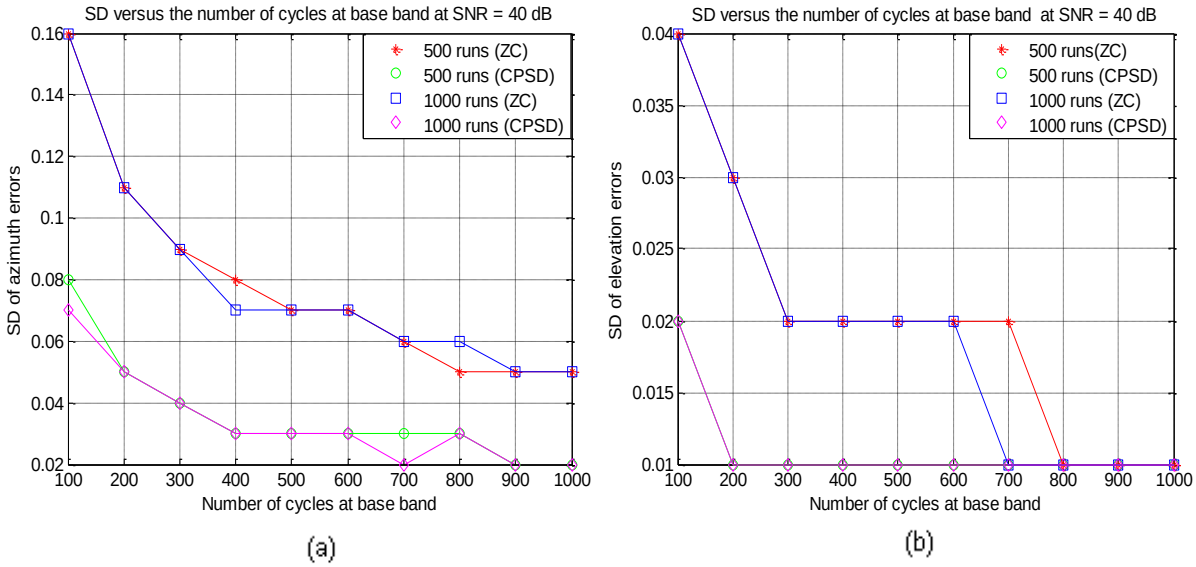

Figure A-1: Comparison of the ZC and CPSD algorithms for the SD of (a) azimuth and (b) elevation errors versus the number of cycles at baseband

Appendix B: The illustration of the height of the antennas

The photograph shows the view from the Reference antenna toward the west and the author next to the antenna. This shows the height of the elements from ground level.

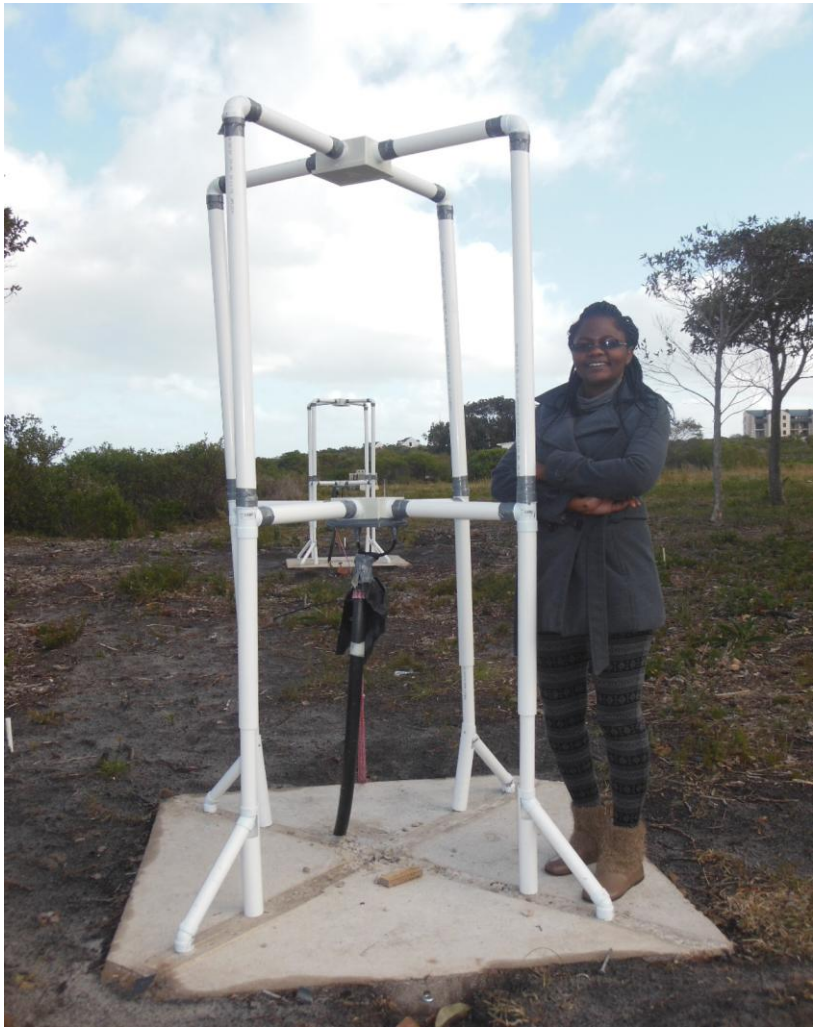

Appendix C: The receiving system

The photograph below shows the receiving system of the HF DF array at SANSA Space Science where signals will be recorded, analysed and processed in order to estimate the azimuth and elevation angles of the incoming signals. The four cables that go to the receiver are from the three antennas, with the Reference signal split into two signals, one from each of the Reference antenna loops.

The annotated picture below shows the inside of the receiving system box.

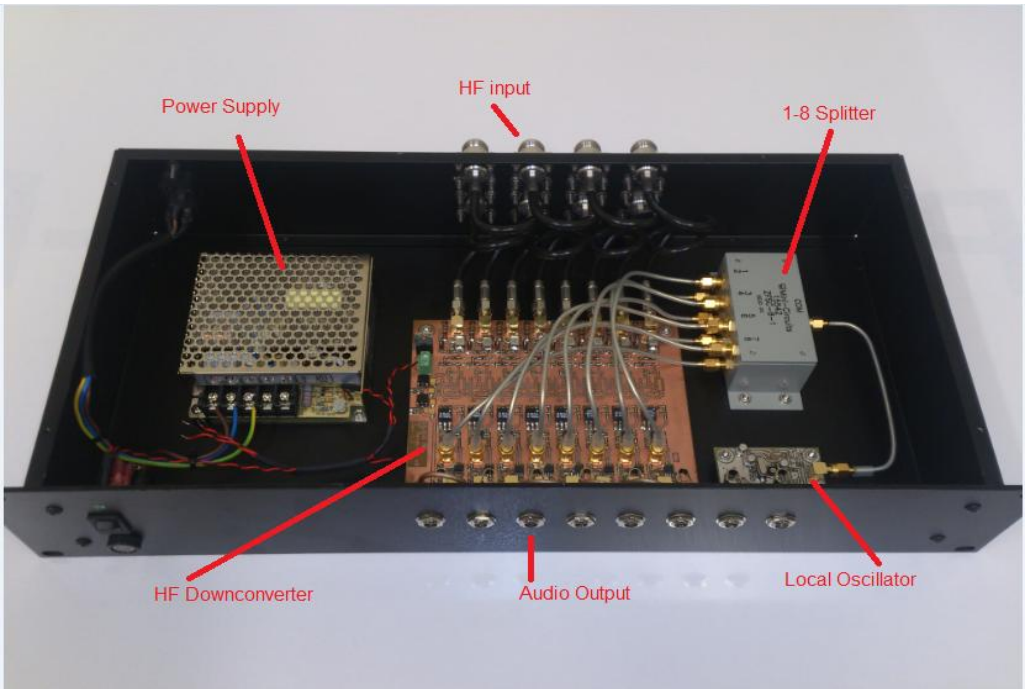

Appendix D: MATLAB CODES

This Appendix, gives the explanations of the MATLAB codes on the CD, which is available from the author. All the codes have to be saved in the same directory when running them in MATLAB

Functions:

DF_azel_v3a.m: This function calculates the azimuth and elevation angles from the phase differences in all four quadrants, using the McNamara equations. This function maps the phase differences chi-S1 ($\Delta\psi_{S1}$) and chi_W1 ($\Delta\psi_{W1}$) to azimuth and elevation. This function is the same for every algorithm.

az_el_snr_cc.m: This function calculates the phase difference between the signals using the cross correlation algorithm.

az_el_snr_cpsd.m: This function calculates the phase difference between the signals using the cross power spectral density algorithm.

az_el_snr_FFT2.m: This function calculates the phase difference between the signals using the Fast Fourier Transform algorithm.

az_el_snr_zc.m: This function calculates the phase difference between the signals using the zero crossing algorithm.

Scripts:

In all the MATLAB scripts, there are constants and there are variables. All variables can be changed by the user. The amplitudes of the signals are fixed, they are assumed to be unity. The period of the signal depends on the baseband frequency. The number of samples per cycle may be selected. The minimum level and maximum level of SNR is selected. Alpha (azimuth angle) and theta (elevation angle) are the input angles that are selected and the number of runs represents the number of Monte Carlo simulations.

cross_power_spectral_algorithm_2014_final.m: This script evaluates the CPSD algorithm.

cross_correlation_algorithm_2014_final.m: This script evaluates the CC algorithm.

FFT_Algorithm_West_South_2014.final.m: This script evaluates the FFT algorithm.

Zero_crossing and time_difference_2014.final.m: This script evaluates the ZC and time difference algorithm.

If one wants to evaluate the SD of the azimuth and elevation errors versus the SNR, the analysis_type to be selected is the Std_vs_SNR. To evaluate the size of the errors, using the histograms and fitting the Gaussian curve on the histograms, the analysis_type to be selected is the error_distribution. To evaluate the SD of the errors, the number of Monte Carlo simulations has to be specified, because if the number of Monte Carlo simulation is 0, one will not be able to get the distribution of the errors.

Az_el_estimation_SNR_test_V4.m: This code estimates azimuth and elevation angles of the DOA using different algorithms to determine the estimated phase difference between the two signals. In this script, there is the option to select the algorithm. There are various options for the analysis_type. If one wants to evaluate the distribution of the errors for all azimuth angles (0˚ to 360˚) and elevation angles (0˚ to 90˚), the analysis_type to be selected is the Error_map. To evaluate the SD of the errors, the analysis_type to be selected is the Error_SD_map. To evaluate the mean of the errors, the analysis_type to be selected is the Error_mean_map.

ZC algorithm code:

```
%% Find zero-crossings for the Reference signal
The array t() contains the sampled antenna baseband signal
The array iz_ref[] will contain the length of the indices for the Reference
antenna signal
The array t0_ref[] will contain the final zero crossing indices for the
Reference antenna signal

iz_ref=[];          % Create an empty matrix of iz_ref
t0_ref=[];          % Create an empty matrix of t0_ref
tic                 % Elapse time
for ip=1:length(t)-1% Start a for loop for the ip = 1 to the length of t -1
    t1=t(ip);       % Valid point of time before the crossing state
    t2=t(ip+1);     % Valid point of time after the crossing state
    bt1=bref(ip);   % Valid point of amplitude before the crossing state
    bt2=bref(ip+1); % Valid point of amplitude after the crossing state
    if bt1<=0 && bt2>=0 % Find ZC
       iz_ref=[iz_ref,ip];
       t0=(bt2*t1-bt1*t2) /(bt2-bt1); % Formula to calculate the real ZC
       t0_ref=[t0_ref,t0];
      end                   % End if loop
end                         % End for loop



%% Find the zero crossing for the South Antenna 1
The array iz_1[] will contain the length of the indices for the South
antenna 1 signal
The array t0_S1[] will contain the final zero crossing indices for the
South Antenna 1 signal
```

```
iz_1=[];              % Create an empty matrix of iz_1
t0_S1=[];             % Create an empty matrix of t0_S1
for ip=1:length(t)-1  % Start a for loop for the ip = 1 to the length of t
    t11=t(ip);        % Valid point of time before the crossing state
    t22=t(ip+1);      % Valid point of time after the crossing state
    bt11=S1(ip);      % Valid point of amplitude before the crossing state
    bt22=S1(ip+1);    % Valid point of amplitude after the crossing state
  if bt11<=0 && bt22>=0 % Find ZC
     iz_1=[iz_1,ip];
     t00=(bt22*t11-bt11*t22)/(bt22-bt11);%Formula to calculate the real ZC
     t0_S1=[t0_S1,t00];
  end                 % End if loop
end                   % End for loop

%% Find the crossing for the West Antenna 1
The array iz_2[]will contain the length of the indices for the South
antenna 1 signal
The array t0_W1[] will contain the final zero crossing indices for the West
Antenna 1 signal

iz_2=[];             % Create an empty matrix of iz_2
t0_W1=[];            % Create an empty matrix of t0_W1
for ip=1:length(t)-1 % Start a for loop for the ip = 1 to the length of t
    t13=t(ip);       % Valid point of time before the crossing state
    t23=t(ip+1);     % Valid point of time after the crossing state
    bt13=W1(ip);     % Valid point of amplitude before the crossing state
    bt23=W1(ip+1);   % Valid point of amplitude after the crossing state
 if bt13<=0 && bt23>=0 % Find ZC
  iz_2=[iz_2,ip];
  t01=(bt23*t13-bt13*t23)/(bt23-bt13);% Formula to calculate the real ZC
  t0_W1=[t0_W1,t01];
 end                 % End if loop
end                  % End for loop
```